Modelling and Design of a Vanadium Redox Flow Battery for Energy Storage

DE Schutte


orcid.org/0000-0002-5056-4029

Dissertation accepted in fulfilment of the requirements for the degree Master of Engineering in Chemical Engineering at the North West University

Supervisor:	Dr RH van Coller
Co-supervisor:	Prof HM Krieg
Co-supervisor:	Mr AF van der Merwe

Graduation: June 2025

DECLARATION

I, Denise Schutte, declare that this dissertation, titled "MODELLING AND DESIGN OF A VANADIUM REDOX FLOW BATTERY FOR ENERGY STORAGE," is the result of my own independent research work. I have conducted all the research, analysis, and writing myself, utilising writing aids such as Microsoft Copilot™ and Grammarly™ only for grammar and sentence construction.

I certify that this work is original, and any sources used have been properly acknowledged. This dissertation has not been submitted for any degree or examination at any other academic institution.

Signed,

Denise Schutte

ABSTRACT

This dissertation focuses on the modelling and design of a Vanadium Redox Flow Battery (VRFB) for energy storage applications. The research includes a comprehensive analysis of the VRFB system, utilising an Equivalent Circuit Model (ECM) to simulate the battery's performance. Key findings emphasise the optimisation of the battery's efficiency and reliability. Through experimentation and data analysis, the study provides insights into the development and practical implementation of advanced energy storage solutions, highlighting the potential improvements and applications of VRFB technology.

Key terms

Vanadium Redox Flow Batteries (VRFB)

Equivalent Circuit Model (ECM)

Energy Storage Solutions

LIST OF ABBREVIATIONS

$V_2(SO_4)_3$	Vanadium Sulphate
$(VO)SO_4$	Vanadyl Sulphate
ECM	Equivalent Circuit Model
H_2	Hydrogen
H_2SO_4	Sulphuric Acid
NaS	Sodium Sulphur
OCP	Open Circuit Potential
RC	Resistors and Capacitor Pairs
RFB	Redox Flow Battery
SoC	State of Charge
SoH	State of Health
V_2O_5	Vanadium Pentoxide
VRFB	Vanadium Redox Flow Battery
ZnBr	Zinc Bromide
VCl_3	Vanadium Trichloride
HCl	Hydrogen Chloride
CH3SO3H	Methanesulfonic Acid
H3PO4	Phosphoric Acid
NaOH	Sodium Hydroxide
PAN	Graphitised Polyacrylamide
MSA	Methanesulfonic Acid

A	Ampère	Current
Ah	Ampère Hour	Capacity
C	Coulomb	Electric Charge
E	Voltage	Cell Potential
K	-	Equilibrium Constant
kg	Kilogram	Mass
kW	Kilowatt	Power
kWh	Kilowatt Hours	Energy
mA/cm^2	Milliampere per Square Centimetre	Current Density

Q	Coulomb	Electric Charge
R	Joule per Mol Kelvin	Universal Gas Constant
s	Seconds	Time
V	Voltage	Potential Difference
Wh/L	Watthour per Liter	Energy Density
Ω	Ohm	Resistance

TABLE OF CONTENTS

LIST OF TABLES

LIST OF FIGURES

CHAPTER 1 INTRODUCTION

1.1 Background and Motivation

The world is facing a growing demand for energy and a need to reduce greenhouse gas emissions from fossil fuel combustion. Renewable energy sources such as solar, wind and hydro power offer clean and sustainable alternatives, but are subject to variability and uncertainty (Höök and Tang, 2013, Poullikkas, 2013, Sinsel *et al*., 2020, Agoundedemba *et al*., 2023). Therefore, there is a challenge to integrate these renewable energy sources into the existing power grid and ensure reliable and stable electricity supply. One possible solution is to use energy storage systems that can store excess energy from renewable sources when they are available, releasing it when needed (Capellán-Pérez *et al*., 2014). In this way, energy storage systems can help balance the supply and demand of electricity, reduce the dependency on fossil fuels, and enhance the resilience and efficiency of the power grid (Poullikkas, 2013, Agoundedemba *et al*., 2023, Sinsel *et al*., 2020).

Among various types of energy storage systems, batteries are widely used for their high energy density, fast response, and flexibility (May *et al*., 2018). However, conventional batteries such as lead-acid and lithium-ion have some limitations such as high cost, low cycle life, safety issues and environmental concerns (May *et al*., 2018, YILMAZ, 2015). Redox flow batteries (RFBs) are a promising alternative that addresses some of these disadvantages. RFBs are electrochemical devices that store energy in liquid electrolytes that circulate through a cell stack where redox reactions take place (Shigematsu, 2011). The electrolytes are stored in separate tanks that can be scaled up or down according to the desired capacity. Some of the characteristics of RFB's that are beneficial for energy storage are long cycle life, low maintenance, moderately high efficiency, modular design and independent power and energy ratings (Shigematsu, 2011).

Vanadium redox flow batteries (VRFB) are a type of RFB that use Vanadium ions in both the positive and negative electrolyte (Li *et al*., 2013, Li *et al*., 2011a, Li *et al*., 2011b, Li *et al*., 2011c). The use of the same active species in both electrolytes, combats the effects of cross contamination that are present in other RFB technologies (Li *et al*., 2013, Li *et al*., 2011b) VRFBs also have high stability, reversibility, and electrochemical activity (Li *et al*., 2011c). However, VRFBs still face some challenges such as lower electrolyte energy density, high cost, membrane degradation and performance optimisation (Li *et al*., 2011b).

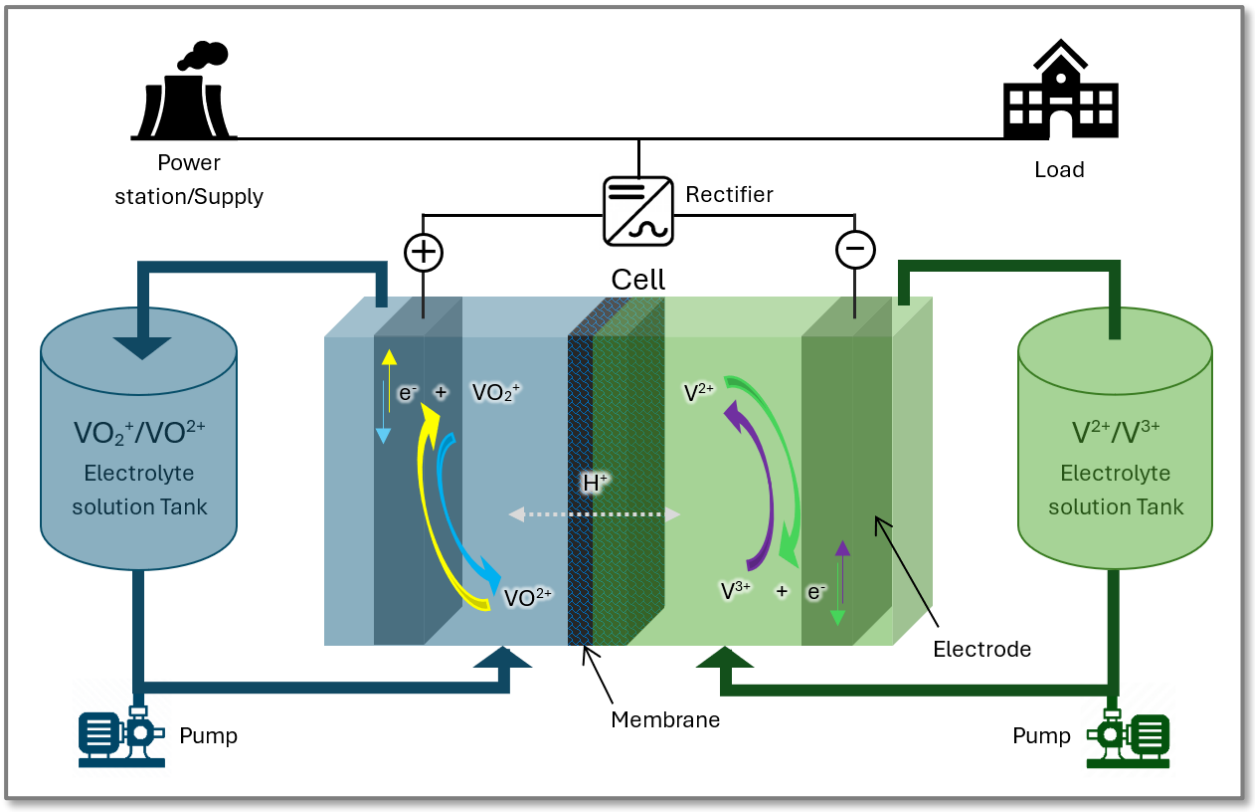

Figure 1-1: Vanadium Redox Flow Battery setup description - Adapted from (Shigematsu, 2011)

Figure 1-1 depicts a representation of a VRFB cell, incorporated into a power grid. The different oxidation states of Vanadium at their corresponding electrodes and storage tanks are indicated. The semi permeable membrane in the centre of the cell comprises of an ion-exchange membrane which allows the Hydrogen (H^+) ions to pass through and balance the charge within the cell. The pumps circulate the electrolyte and are operational only during the discharge and charging stages of the cell (Shigematsu, 2011).

Constant and reliable power supply is required for any modern micro-grid to function. Specialised equipment in the industrial, educational and commercial sectors rely on a constant and reliable power supply. If an energy storage solution was implemented to combat the effects of unreliable grid supply, the operation of these businesses and even residences would improve. The independently scalable capacity, low maintenance and long cycle life make VRFBs a possible storage solution at this scale. The implementation of VRFBs could therefore improve the function of those affected by unstable grid supply.

1.2 Problem statement

South Africa suffers from frequent power outages due to the inadequate supply and distribution of electricity historically sourced from fossil fuel-based generation plants. Poor maintenance,

ageing infrastructure and environmental factors affect the quality and reliability of the national power grid. The national electricity supplier, Eskom Holdings Ltd, habitually resorts to load shedding or scheduled rolling blackouts to cope with the high demand and prevent grid collapse. This negatively affects various sectors of the economy and society, such as industry, commerce, education, and health. While renewable energy sources are an alternative to the national power grid, their variability renders them unable to provide consistent energy throughout the day.

1.3 Aim and Objectives

A battery system is required for storing energy, providing backup power and the stabilisation of micro-grids. The micro-grids operate independently of the national power grid during national grid outages. They rely on the battery system to sustain their operation during these outage periods. Additionally, the battery system must be able to store energy generated from renewable energy sources.

The aim of this study is to design and evaluate a VRFB system for energy storage for a micro-grid at the North-West University campus in Potchefstroom, South Africa.

The objectives of this study are:

- To determine the requirements of the VRFB system for a micro-grid, such as capacity, size, efficiency, and charge/discharge capabilities.
- To review the factors that affect the performance of the VRFB system, such as electrolyte composition, membrane type, electrode material and additives, to determine the best design solution for the VRFB system.
- And use the system factors investigated to model a VRFB system that meets the micro-grid requirements.

1.4 Scope of study

This study investigates the factors influencing the performance of Vanadium Redox Flow Batteries (VRFBs). The focus will be on the electrolyte, electrode, and membrane, as detailed in existing literature. Cost analysis will be confined to the estimated total system cost, also derived from literature sources. The availability of materials will not be examined.

The primary objective of this study is to develop a model capable of predicting VRFB performance during continuous blackouts. An electrical equivalent VRFB model will be proposed to predict the electrical response of a VRFB under the load of a building. This model builds on the studies by Pugach *et al*. (2018) and Yesilyurt and Yavasoglu (2023) by incorporating experimental VRFB

measurements from the literature and following a requirements-based approach. This study will not include physical experimental work, rather, experimental verification of the model will be conducted by testing the modelled data against external sources found in the literature.

The model will be designed to meet the requirements of a building experiencing power outages, specifically the N1 building at North-West University. It will also offer empirical predictions of capacity retention and state of charge. Considering the scale of the micro-grid, the VRFB pump power will not be factored into the power rating calculations. This study assumes that the pump power is included in the overhead calculations above the micro-grid's requirements. The VRFB model will assume a constant temperature.

CHAPTER 2 LITERATURE REVIEW

To develop a comprehensive understanding of VRFBs and their potential for energy storage in micro-grids, this literature review chapter will examine the existing research. This chapter details the elements that comprise a VRFB and provides insight into how these elements ultimately impact the battery's performance and eligibility as an energy storage solution. Subsequently, the chapter will provide an overview of the modelling techniques used to model VRFBs. This will include a general discussion on the advantages and disadvantages of the various techniques in use today, as well as an in-depth discussion on electrical equivalent models and the parameter estimation techniques that it requires to accurately predict the electrical response of the battery system.

2.1 VRFB's

Vanadium redox flow batteries were proposed by Skyllas-Kazacos and co-workers in 1985 (Kim *et al*., 2015) and have been extensively investigated, with several demonstration plants in operation in Japan (Oriji *et al*., 2004). VRFBs have already achieved initial commercial operation and are favoured for large-scale renewable energy storage (Huang *et al*., 2021).

VRFBs use the changes in the valence states of Vanadium ions in the positive and negative electrolytes to interconvert between electrical energy and chemical energy (Huang *et al*., 2021). This is possible because of the four different oxidation states Vanadium can exert when in solution. The states in which Vanadium can be found in the electrolyte solution are shown in Equations 2-1 and 2-3. The half-reactions depicted in Equations 2-2 and 2-4 demonstrate the changes undergone by the Vanadium ions during the charging phase (Huang et al., 2021, Delgado et al., 2022, Oriji et al., 2004, Sangwon, 2019). The reverse of these reactions depicts the activity occurring during the discharge of the battery (Shigematsu, 2011, Sangwon, 2019).

Cathode

$$VO^{2+} + H_2O \leftrightarrows VO_2^+ + 2H^+ + e^- \qquad \text{2-1}$$

$$V^{4+} \leftrightarrow V^{5+} + e^- \qquad \text{2-2}$$

With $E^{\theta}_{cathode} = 1.00\ V$.

Anode

$$V^{3+} + e^{-} \leftrightarrow V^{2+} \qquad \text{2-3}$$

$$E^{\theta} = E^{\theta}_{cathode} - E^{\theta}_{anode} = 1.26\ V \qquad \text{2-4}$$

With $E^{\theta}_{anode} = -0.26\ V$.

At the anode the bivalent Vanadium ion undergoes oxidation to the trivalent Vanadium ion (Shigematsu, 2011). The electrode potential for the oxidation half-reaction is -0.26 V at the anode while the pentavalent Vanadium ion gains an electron, which originated during the oxidation reaction (Shigematsu, 2011, Bogdanov *et al*., 2023). The electrode potential for the reduction half-reaction is 1 V while the overall electrode potential of the redox reaction adds up to 1.26 V. (Bayeh *et al*., 2021, Weber *et al*., 2018, Blanc, 2009). The total electromotive force (electric potential) over an entire cell equates to between 1.4 V and 1.5 V for most VRFBs, also referred to the as open circuit potential (OCP) of a cell (Shigematsu, 2011, Sangwon, 2019). This is a lower OCP compared Li-ion batteries, averaging in around 3.6 V (Yoshio *et al*., 2009).

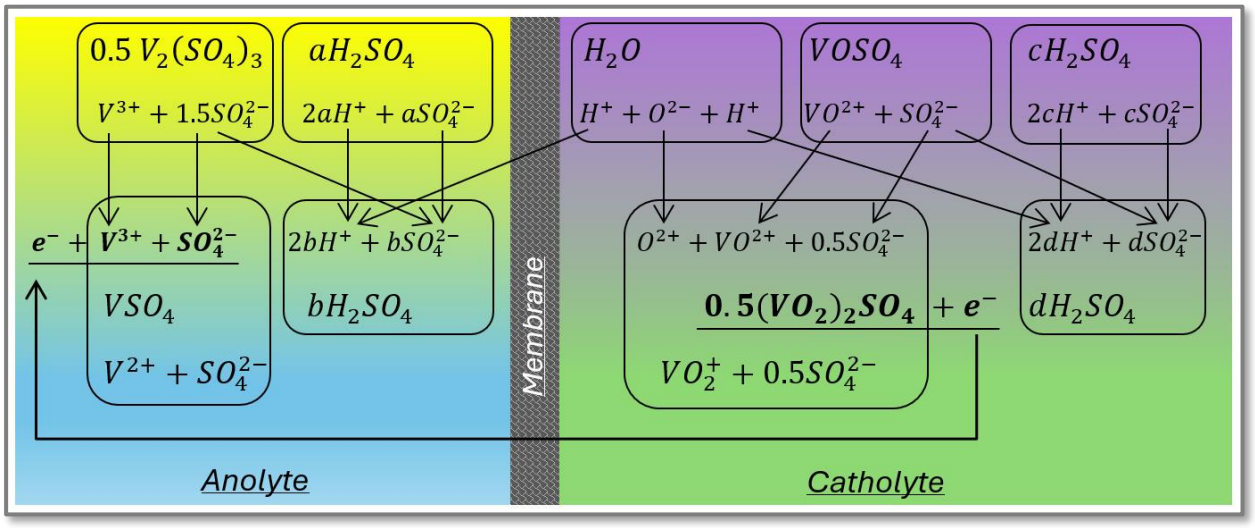

Figure 2-1: Illustration of full ionic VRFB equations during charging - Adapted from (Blanc, 2009)

Figure 2-1 illustrates the complete ionic equations which contain Vanadium ions in various oxidation states as well as protons (H^+) and sulphate ions (SO_4^{2-}). The H^+ and (SO_4^{2-}) ions are spectator ions and essential for mass conservation and charge balance in the electrolyte concentration calculations (Krowne, 2023). The illustration provides an understanding of proton concentration variations and why some H^+ ions cross the membrane to balance the electrolyte charges (Blanc, 2009).

Table 2-1: Comparison between current energy storage devices (Skyllas-Kazacos and McCann, 2015, May *et al*., 2018, Du *et al*., 2023)

	VRFB	NaS	Lead acid	Li-on	ZnBr
Life, years	15	10	15	15	7
Cycles	20000 up to 200000	4000	2000	2500	3000
Energy efficiency, %	70	75	85	90	70
Installed system cost, $/kWh	750-850	600-800	400-600	1250-1500	600-800

Table 2-1 depicts the comparison between various batteries, based on performance and running costs. VRFBs can sustain over five times the amount of charge/discharge cycles than their competitors. This is an important factor when the battery system discharges regularly such as during scheduled blackouts. The service life of the battery is projected to last up to 10 years (Rychcik and Skyllas-Kazacos, 1988).

The capacity and power rating of the battery system are both affected by the electrolyte. While the capacity is controlled by the concentration of active species in the electrolyte, the power rating of the battery is related to the electrode size and active species behaviour. The number of cell stacks in the battery system as well as their voltage also impact the total system capacity (Lourenssen *et al*., 2019).

2.1.1 Electrolyte

The electrolyte serves as a key component in VRFBs, since it acts as the energy storage medium. As such, it has a great effect on the performance and cost of the battery system (Zihan *et al*., 2024, Iwakiri *et al*., 2021). VRFB's Electrolytes typically consist of Vanadium species in various oxidation states dissolved in a supporting electrolyte, commonly sulfuric and hydrochloric acids (Phil-Jacques *et al*., 2022, Roznyatovskaya *et al*., 2019). The supporting electrolyte enhances ionic conductivity and provides hydrogen ions for reactions (Phil-Jacques *et al*., 2022).

Different preparation methods have been explored for electrolytes. The catalytic reduction of V2O5, has proven to be cost-effective (Wenxin *et al*., 2023). Other methods include chemical reduction, electrolysis, and ion exchange (Guo *et al*., 2022). Additives have also been explored to enhance electrolyte stability and electrochemical performance (Wenxin *et al*., 2023). Various compounds, including polyhydroxy-alcohols (Nguyen *et al*., 2024), taurine (Jinyeon *et al*., 2018), carbohydrates (Liming *et al*., 2022, Vasudevarao and Ramanujam, 2017), and ionic organic

compounds (Wang *et al*., 2014), have shown promising results. These additives enhance the thermal stability, electrochemical activity, and capacity retention of VRFBs. For instance, taurine improved energy efficiency and thermal stability by forming Vanadium-additive complexes (Jinyeon *et al*., 2018). Carbohydrates like α-lactose monohydrate and D-fructose mitigated capacity decay and improved electrochemical performance (Liming *et al*., 2022, Vasudevarao and Ramanujam, 2017). Potassium diformate enhanced the positive electrolyte's performance (Wei *et al*., 2022). A combination of ammonium phosphate and polyvinylpyrrolidone enabled VRFB operation at 50°C (Nguyen *et al*., 2024). These additives work through various mechanisms, including complexation, electrostatic repulsion, and precipitation inhibition (Wenxin *et al*., 2023), offering promising solutions for improving VRFB performance.

Methods of modifying the electrolyte composition have shown mitigation of capacity decay and volume variation issues (Toja *et al*., 2023). Although advancements have been made, improving electrolyte stability, temperature adaptability and monitoring methods continues to be a challenge for enhancing VRFB performance and cutting costs (Zihan *et al*., 2024, Xiongwei *et al*., 2014).

The literature contains investigations on the performance differences between a sulfuric acid (H_2SO_4) solution and a mixed sulfuric and hydrochloric acid (HCL) solution. In these investigations the mixed electrolyte solution performed better than the H_2SO_4 electrolyte solution, particularly with regard to energy density, stability over a wider temperature range and improved reaction rates (Li *et al*., 2011a, Zihan *et al*., 2024).

At a concentration of 2.5 M Vanadium sulphate and 6 M HCL, the temperature range increased to -5°C – 50°C. For an H_2SO_4 electrolyte solution, the stability of the electrolyte was limited to a temperature range from 0°C to 40°C (Li *et al*., 2011a, Zihan *et al*., 2024). The wider range of operating temperature diminishes the need for temperature control within both the cell and the electrolyte storage tanks. Along with the temperature range widening, the energy density also increased from 22 Wh/L to 39 Wh/L at a current density of 25 $mA.cm^{-2}$. The combination of both sulfate and chlorine ions enhances the performance of the battery significantly and should ideally be prepared in a 2.5:6 concentration [M] ratio for $VOSO_4$ and HCL, respectively (Li et al., 2011a, Zihan et al., 2024, Sangwon, 2019).

The electrolyte solute and solvents' advantages and disadvantages are set out in Table 2-2 and Table 2-3. These tables serve as a summary of the options for electrolyte compositions from various literature articles.

Table 2-2: Electrolyte Solute advantages and disadvantages (Zihan *et al*., 2024, Du *et al*., 2023, Cao *et al*., 2018, Lourenssen *et al*., 2019)

Vanadium Salt	Disadvantage	Advantage
VCl_3	Potential for chlorine gas generation	-
$VOSO_4$	Limited by solubility at high temperatures	Allows easy control of Vanadium concentration
V_2O_5	Low solubility in acids	Lower cost

Table 2-3: Electrolyte Solvent advantages and disadvantages (Zihan *et al*., 2024, Du *et al*., 2023, Cao *et al*., 2018, Lourenssen *et al*., 2019, Li *et al*., 2011a)

Solvent	Disadvantage	Advantage
HCl	• Potential for chlorine gas generation. • Results in lower electrolyte potential compared to H_2SO_4 (Phil-Jacques *et al*., 2022).	• High solubility over broad temperature range (0°C - 50°C) (Kim *et al*., 2011).
H_2SO_4	• Narrow temperature window and can lead to precipitation at high temperatures. • Limited concentration range (1.5 M – 3 M)	• High solubility for Vanadium ions. • Improves electrolyte conductivity. • Most common. • No hazardous emissions.
CH_3SO_3H	• Increases solution resistance and negatively affects electrochemical kinetics at higher concentrations. • Higher costs.	• Improves electrochemical activity. • Increases redox reaction kinetics. • Decreased mass transport resistance (Lourenssen *et al*., 2019) • Higher temperature stability than H_2SO_4
Mixed electrolytes: HCl & H_2SO_4	• Requires control of HCl concentration to prevent Cl_2 production. • Potential volatility issues.	• High energy density (40Wh/L). • High energy efficiency (85%).

		• Wide temperature range (-10°C – 50°C). • Increased Vanadium concentration (>2.5 M).
Electrolyte Additives	**Disadvantage**	**Advantage**
K_2SO_4	• Increases precipitation rate in V^{5+}	• Stabilises V^{4+}
Na_3PO_4	• Causes inhibiting amounts of precipitation when tested within the cell.	• Stabilises V^{3+}, V^{4+}, and V^{5+} exceptionally well in ex-situ tests.

The energy density of VRFBs is a critical parameter that determines their potential applications and performance. The energy density of VRFBs is typically around 25 Wh/L – 35 Wh/L (Lourenssen *et al*., 2019), which is relatively low compared to other types of batteries (Park *et al*., 2017). This characteristic makes VRFBs suitable for large-scale energy storage applications where physical size is not a major constraint.

The energy density can be influenced by several factors. One of the primary factors is the concentration of Vanadium in the electrolyte. A higher concentration of Vanadium can lead to an increase in energy density. However, this increase in concentration can also lead to increased viscosity and decreased ion mobility, which can negatively affect the overall performance of the battery (Park *et al*., 2017).

Temperature is another factor that can significantly influence the energy density of VRFBs. As the temperature increases, the energy density of the battery also increases due to the enhanced ionic conductivity and reaction kinetics (Li *et al*., 2011a). However, excessively high temperatures can lead to accelerated degradation of the battery, reducing its lifespan (Praphulla *et al*., 2022).

The energy density of VRFBs can also be improved by optimising the design and operation of the battery. For instance, the use of advanced electrode materials and designs can enhance the electrochemical reactions in the battery, leading to an increase in energy density (Hall *et al*., 2020). Additionally, optimising the operating conditions, such as the flow rate and state of charge, can also improve the energy density (Yang *et al*., 2015).

Table 2-4: Comparison of the energy density and efficiency of additives (Zihan *et al*., 2024)

Additive	Vanadium [M]	Acid concentration [M]	Energy density [Wh/L]	Current density [mA cm^{-2}]	Energy efficiency [%]
$H_2 SO_4$	1.0 – 1.5	3.0	16.0 – 18.0	150	77
HCl	2.3	10	35.5	100	80
$H_2 SO_4$ -HCl	3.0	3.0:6.0	40.8	75	81
MSA	2.0	7.0	–	40	83
$H_2 SO_4$ -MSA (Methanesulfonic acid)	2.8	0.25	39.9	20	78
H_2 SO4 -$H_3 PO_4$	2.5	0.16	–	–	83

Table 2-4 depicts the differences in energy density and efficiency of various electrolyte additives. While the energy efficiency of these additives seems comparable, the energy density can vary significantly. From Table 2-4, the low energy density of H_2SO_4 at 16 Wh/L – 18 Wh/L at 150 mA.cm^{-2} is substantially lower than its competing additives. The addition of additives increases the solubility and reduces the precipitation which results in higher energy density electrolytes (Zihan *et al*., 2024).

An equation for the energy density can be derived form the standard Gibbs and Nernst equations. The total energy of the system may be expressed as a function of the volume of the electrolyte as shown in Equation 2-5 (Fornaro et al., 2022, Sangwon, 2019).

$$E = \frac{E_{cell} \cdot V_t F C_V}{3600} [Wh] \qquad 2\text{-}5$$

In Equation 2-5, E denotes the total energy of the electrolyte in Wh. E_{cell} the cell voltage, V_t the volume of the electrolyte in each tank, F denotes Faraday's constant and C_V the vanadium concentration. The energy density can be calculated from Equation 2-5 by calculating the ratio between E and the total electrolyte volume (Fornaro et al., 2022).

While the energy density is an important parameter, it is not the only factor to consider when evaluating the performance of VRFBs. Other factors such as power density, efficiency, lifespan, and cost are also important in determining the overall performance and suitability of VRFBs for different applications (Weber *et al*., 2018).

VRFBs generally function within a temperature range of 10°C – 40°C due to limitations in electrolyte stability (Tian *et al*., 2023, Ren *et al*., 2023, Praphulla *et al*., 2022). Lower temperatures hinder performance by reducing ion diffusivity and reaction kinetics (Rao and Jayanti, 2023), while

higher temperatures may lead to the precipitation of Vanadium species (Nguyen *et al*., 2024). Inorganic compounds like ammonium phosphate and sodium pyrophosphate dibasic, alongside organic additives such as polyvinylpyrrolidone, have shown potential to enhance thermal stability and electrochemical performance (Nguyen *et al*., 2024, Yeon *et al*., 2017). Additionally, both the state of charge and Vanadium concentration can affect thermal stability (Yang *et al*., 2020).

Table 2-5 depicts the upper and lower temperature ranges, and stability for the various Vanadium species and Sulphate concentrations. The Additives are also evaluated and compared to the base electrolyte solution. From Table 2-5 a mixed SO_4^{2-} and HCL electrolyte solution predicts the broadest temperature range and stability. The electrolyte solution's composition affects the concentration and volume calculation.

Table 2-5: Temperature stability of Vanadium electrolytes (Choi et al., 2017)

Vanadium species	Concentration [mol/l]			Temperature [°C]	Precipitation time
	Vanadium [V]	Sulphate (SO_4^{2-})	Additive		
V(II)	1.5	5.0	–	−5	>90 days
	2.0	5.0			419 h
V(III)	1.5	5.0	–	−5	>90 days
	2.0	5.0			634 h
V(IV)	1.5	5.0	–	−5	>90 days
	2.0	5.0			18 h
	3.0	3.0	6.0 M HCL	−5	>10 days
V(V)	1.5	5.1	–	40	>90 days
	2.0	5.0			<95 h
	2.0	5.0	3 wt.% CH_3SO_3H	40	149 h
	2.0	5.0	3 wt.% $Na_2SO_4^{2-}$	40	70 h
	2.0	5.0	3 wt.% $Al_2(SO_4)_3$	40	120 h
	2.0	6.0	0.1 – 1.0 wt.% Polyacrylic acid	40	147 – 166 h
	2.0	3.0	3% Trishydroxymethyl aminomethane	40	>48 h
	3.0	3.0	6.0 M HCL	40	>10 days

2.1.2 Electrodes

The electrodes serve as the sites for the electrochemical reactions to occur during charging and discharging of the battery (Delgado *et al*., 2022). Electrodes influence the performance and cycle life of VRFBs (Xu *et al*., 2020). The properties of the electrodes, such as porosity and compression ratio, directly impact the battery's performance metrics like coulombic efficiency, activation polarisation, ohmic polarisation, concentration polarisation, and pressure drop (Huang *et al*., 2022).

The ideal electrode material should possess high conductivity, good stability in the electrolyte, high electrochemical activity, and low cost (He *et al*., 2022). Carbon-based materials, such as graphite felt, are commonly used due to their high conductivity, low cost, and good stability (He *et al*., 2022, Aberoumand *et al*., 2020). However, the electrochemical activity of carbon-based materials can be low, which can limit the performance of the battery (Aberoumand *et al*., 2020).

In a study by Bin Li *et al*. (Li *et al*., 2013), Bismuth (Bi) nanoparticles were used as an electrocatalyst to increase the reaction time of the bivalent to trivalent ion oxidation reaction within the graphite felt electrode. It was found that the Bi ions did not pass through the ion exchange membrane and contaminate the electrolyte at the cathode (Li *et al*., 2013). The suggestion is to deposit Bi nanoparticles onto the graphite felt surface of the anode and to allow for Bi nanoparticles to be suspended within the electrolyte containing V^{2+} and V^{3+}. The use of Bi nanoparticles increased the efficiency of the battery by as much as 8% and 11% when applying a discharge current density of 100 and 150 $mA.cm^{-2}$ respectively (Li *et al*., 2013). The specific capacity also increased to 64% of the theoretical capacity as opposed to 30% whereby Bi nanoparticles are absent. The optimal concentration of Bi nanoparticles was determined to be 0.01M. An efficiency of 86% was obtained at a current density of 70 $ma.cm^{-2}$ whereby 0.01M Bi nanoparticles were added to modify the electrode (Li *et al*., 2013).

Another attempt to improve the reaction rate of the oxidation of V^{2+} to V^{3+} was studied by Wenyue Li *et al*., whereby multi-walled carbon nanotubes (MWCNT) were evaluated. The addition of carboxyl and hydroxyl groups was used to modify the MWCNT. The carboxyl MWCNT showed improved results compared to regular carbon electrodes due to the increased surface area of the MWCNT and the catalytic activity introduced to the electrode by the carboxyl group addition (Li *et al*., 2011b). The use of carboxyl MWCNT in a laboratory scale experiment improved a generic carbon felt (CF) electrode to achieve an additional 250 seconds on a charge-discharge cycle at a constant current density of 20 $mA.cm^{-2}$. The overall duration of a charge-discharge cycle was found to be 3250 seconds, which indicated that the specific capacity of the cell increased by 15%.

An efficiency of 75% was obtained at a current density of 70 $mA.cm^{-2}$ for the modified electrode (Li *et al*., 2011b).

Table 2-6: Summary of applied Electrodes

Electrode Type	Description	Source
Graphitised Polyacrylamide (PAN)	Commonly used in carbon paper and felt forms. Advantageous due to their diverse structure and chemical properties. Commonly used as the positive electrode.	(Lourenssen *et al*., 2019)
Carbon Nanotubes	Developed for improved reactivity and performance; helps address shortcomings of traditional electrodes.	(Lourenssen *et al*., 2019)
Graphite Felt	Large specific surface area High electrical conductivity Low hydrophilicity Possible modifications: • Bi nanoparticles • B4C nanoparticles • titanium nitride nanowires • NiO nanoparticles • graphene oxide • Copper nanoparticles • Pt MWCNT • Modified by thermal treatment • Nitrogen doping • Acid treatment Improves electron transfer rate. Increase active sites	(Aberoumand *et al*., 2020) (Lourenssen *et al*., 2019) (He et al., 2022)

	Increases stability	
	Commonly used as the negative electrode Degradation when used as the positive electrode. Reduction of positive electrode degradation: • Graphene-coating Improve electrochemical activity of positive electrode: • Acid treatment Improve reversibility of positive electrode: • Electrochemical treatment	(He et al., 2022)

Table 2-6 outlines how these materials can enhance battery performance and identifies the challenges associated with their use as positive electrodes. It also describes the use of various electrode materials for both positive and negative electrodes. Carbon-paper electrodes are typically used as positive electrodes, while graphite felt electrodes are used as negative electrodes. Graphite felt electrodes can be implemented as positive electrodes, with modifications to improve the electrode degradation (Lourenssen et al., 2019, Aberoumand et al., 2020, He et al., 2022).

2.1.3 Membranes

The membrane separates the two half-cells, allowing for the selective dispersal of ions while preventing cross-contamination of the electrolytes. The membrane's ion selectivity, resistance, and long-term stability are key factors in the battery's performance and lifespan (Li *et al*., 2011c, Knehr *et al*., 2012, Yang *et al*., 2015, Park *et al*., 2017, Rychcik and Skyllas-Kazacos, 1988).

In the construction of VRFBs, various materials have been evaluated for use as membranes. Ion-selective materials, such as sulphonated polyethylene and Selemion CMV cation-selective material, have been employed in different studies (Rychcik and Skyllas-Kazacos, 1988, Li *et al*., 2011c). These materials have shown promising results, with Selemion CMV demonstrating a high open-circuit voltage even after several weeks of storage (Li *et al*., 2011c).

Nafion, a perfluorosulfonic acid ionomer, is another commonly used membrane material in VRFBs due to its excellent proton conductivity and chemical stability (Knehr *et al*., 2012). However, its high cost and susceptibility to Vanadium ion crossover are significant drawbacks (Knehr *et al*., 2012).

A novel composite membrane was developed by incorporating Sulfonated Poly(Ether Ether Ketone) SPEEK into a Nafion matrix (Yin *et al*., 2015). This composite membrane exhibited improved performance in terms of reduced Vanadium ion crossover and increased coulombic efficiency (Yin *et al*., 2015).

The membrane's characteristics significantly impact the battery's performance parameters, including its energy density, power efficiency, and service life. A high membrane resistance can lead to low voltage efficiencies at charge/discharge current densities (Li *et al*., 2011c). On the other hand, membranes with low selectivity can limit the self-discharge rate of the battery, extending its shelf life (Li *et al*., 2011c).

In a 1 kW (5 kWh) all-vanadium battery, the membrane's performance can contribute to achieving an energy density of 25 Wh/kg, similar to lead/acid and nickel/cadmium batteries (Rychcik and Skyllas-Kazacos, 1988). The membrane's stability over time impacts the battery's life. Charge/discharge cycling tests over 1500 hours have shown negligible decrease in performance, with the only observed change being an increase in the membrane resistivity. Further research is needed to determine which membrane material offers the best long-term stability (Li *et al*., 2011c).

Ongoing research is focused on evaluating a range of membranes and electrode materials to achieve further improvements in performance and cycle life (Li *et al*., 2011c). The development of membranes with improved ion selectivity, lower resistance, and enhanced stability could lead to VRFBs with higher power and energy densities, longer service lives, and broader application potential.

2.1.4 Cost

VRFB, Lithium-Ion batteries (LIB), and lead-acid batteries (LAB), differ in cost and performance. Currently, LIBs lead the market due to falling prices, even though there are safety concerns (Marshall *et al*., 2020). VRFBs offer advantages in safety, lifespan, and environmental impact, but need cost reductions to compete with LIBs (Marshall *et al*., 2020, Roberts and Brown, 2022). Lead-acid batteries are cost-effective for shorter-term storage (Baumann *et al*., 2013), while LIBs become more economical when considering longer operational life (Keshan *et al*., 2016). VRFBs

are more competitive at lower power outputs and higher energy storage capacities (Mignard, 2014).

Table 2-7: Energy storage system cost comparison

System Type	Conclusion	Source
VRFB	The bulk of the capital costs for a VRFB lie in the costs of the Vanadium electrolyte. The capital costs of a VRFB are estimated at $364.44/kWh in 2015.	(Moore *et al*., 2015)
	The cost of the battery components of a VRFB system was 142.4 $/kWh as of July 2017.	(Fernández-Marchante *et al*., 2020)
	Total installed system cost of 750-850 $/kWh in 2018.	(May *et al*., 2018)
	With a capital system cost of 300-800 $/kWh, the cost of the ion-exchange membrane accounts for nearly 40% of the system cost in 2017.	(Leung *et al*., 2017)
Lithium Ion	Total installed system cost of 1250-1500 $/kWh in 2018.	(May *et al*., 2018)
	Cells can be manufactured for less than $100/kWh using low-cost electrode materials in 2020.	(Ciez and Steingart, 2020)
	In 2015, the cost of battery packs for BEVs dropped to an estimated €250 per kWh for leading industry players.	(Wolfram and Lutsey, 2016)

2.2 Modelling and simulation

The current literature suggests 3 traditional VRFB modelling approaches including empirical, lumped parameter and dynamic electrical equivalent models (Bogdanov *et al*., 2023, Pathak *et al*., 2022). These models ultimately aim to simulate VRFB behaviour. Modelling based on electrochemical and fluid mechanic equations has been employed to analyse the chemical, electrical, and mechanical aspects of VRFBs (Ozgoli *et al*., 2015). Simplified dynamic lumped parameter models have been developed to study the effects of electrolyte flow rate, concentration, electrode porosity, temperature, and current on VRFB efficiency (Seepana *et al*., 2018). Equivalent circuit modelling of VRFBs has been applied to improve their performance and integration with renewable energy systems. Recent studies have aimed to refine models by incorporating factors like self-discharge (Buckley *et al*., 2018), the impact of flow rate and pump power inefficiencies (Challapuram *et al*., 2019), as well as intrinsic properties like shunt current,

ion diffusion, and energy use in pumping (Yesilyurt and Yavasoglu, 2023). Battery models, for example, are used for energy management in electric and hybrid vehicles, helping to predict charging status and battery capacity (R. Thakkar, 2021).

While VRFBs are promising for large-scale energy storage, they face challenges in modelling and management (Lourenssen *et al*., 2019, Ra and Bhattacharjee, 2021). Lumped-parameter models with crossover have shown good performance in simulating battery dynamics across a wide range of conditions (Bogdanov *et al*., 2023). However, challenges remain in estimating internal states like the state of charge and state of health (Fornaro *et al*., 2022).

Regarding empirical models, open-circuit voltage (OCV) modelling based on the state of charge (SoC) or Vanadium ion concentrations requires precise measurements and theoretical inputs (Kleinsteinberg *et al*., 2020). Decoupling and accessing voltage loss sources, such as ohmic, concentration, and activation overpotentials, are complicated by limited experimental data (Gvozdik *et al*., 2022).

Equivalent circuit models (ECMs) aim to accurately predict VRFB behaviour under different operating conditions and estimate the state of charge (Challapuram *et al*., 2019). Although ECMs are useful, they don't completely capture every detail of VRFB functioning. For example, ion diffusion across the membrane causes self-discharge, which greatly impacts the precision of state of charge (SoC) estimation in equivalent circuit models (Buckley *et al*., 2018).

ECMs strike a good balance between ease of use, rapid computations, adaptability, and precise prediction of electrical dynamics (Zhang *et al*., 2015). They can simulate battery dynamics and state of health (SoH) without the complexity of electrochemical models (Rotas et al., 2024). ECMs also excel in modelling electrical behaviour in relation to SoH and battery age (Parthasarathy et al., 2020).

An equivalent circuit modelling easily incorporates battery age and SoH dependant modelling. This is directly applicable to the modelling of an electrical grid, where effects like battery fade due to number of cycles plays a major role. Furthermore, ECMs can model the battery requirements of this study without the additional complexities of electrochemical modelling.

2.2.1 Equivalent circuit model (ECM)

An ECM is a circuit network that represents the operational characteristics of a battery, establishing a relationship between the battery's external and internal states (Xiong *et al*., 2019). ECMs could also be described as simplified electrical models, which could be used to represent the electrical behaviour of VRFBs. ECMs are simpler and more adaptable than detailed

electrochemical models, making them suitable for electrical and control assessments of VRFB systems (Zhang *et al*., 2015). ECMs see a popular emergence among Lithium-ion and NIMH battery models (Yesilyurt and Yavasoglu, 2023). While ECMs simplify the representation of VRFB behaviour by overlooking intricate physicochemical intricacies, their popularity soars in the domain of control and estimation, largely due to their computational efficiency (Pugach *et al*., 2018).

In recent years, researchers have advanced ECMs to encompass VRFB-specific phenomena like self-discharge due to Vanadium crossover (Zhang *et al*., 2015), the synergy between electrochemical and thermal dynamics (Xiong *et al*., 2019), and the intricate relationships among state of charge, flow rate, and model parameters (Delgado *et al*., 2022). Moreover, ECMs can replicate shunt currents within electrolyte pathways (Xiong *et al*., 2019, Delgado *et al*., 2022).

ECMs are typically represented by a Randles equivalent circuit (Challapuram *et al*., 2019, Ra and Bhattacharjee, 2021). The circuit includes a state of charge-dependent open-circuit voltage source, internal resistance, and RC (resistor and capacitor) pairs to capture the dynamic battery behaviour (Zhang et al., 2015).

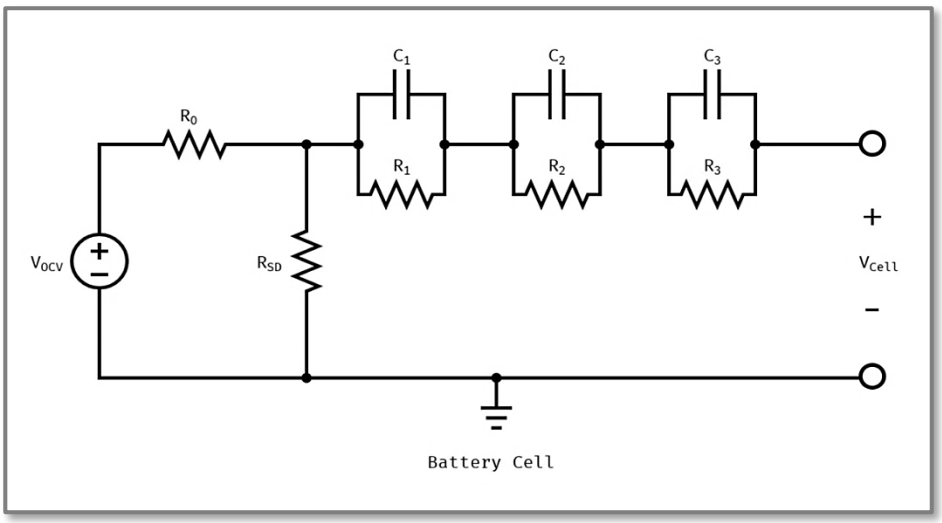

Figure 2-2: Randles equivalent circuit – Adapted from (Theliander et al., 2019)

Figure 2-2 illustrates a typical Randles equivalent circuit. It consists of a series resistance R_0, multiple resistor-capacitor pairs $R_{1,2,3}$ and $C_{1,2,3}$, a self-discharge resistor configured in parallel and a voltage source that corresponds to the open-circuit voltage. The voltage source V_{OCV} represents the cell's open circuit voltage (Praphulla *et al*., 2022). The cell's open circuit voltage is calculated using the Nernst equation based on the SoC and the temperature (Zhang *et al*., 2015).

$$E^{\theta} = E^{\theta'} + \frac{RT}{nF}\ln\left[\frac{c_O(0)}{c_R(0)}\right] \ [V] \qquad \text{2-6}$$

With:

- E^{θ} as the cell potential,
- $E^{\theta'}$ as the standard electrode potential,
- R as the universal gas constant,
- T as the temperature in Kelvin,
- n as the number of electrons transferred in the reaction,
- F as the Faraday constant,
- and C_0 and C_R as the concentrations of the products and the reactants respectively.

The open circuit voltage V_{OCV} in the Randles equivalent circuit shown in Figure 2-2 is equal to the cell potential E^{θ} from Equation 2-6 (Fornaro *et al*., 2022). The series resistance R_s describes the electrolyte solution resistance of the VRFB (Xiong *et al*., 2019, Challapuram *et al*., 2019, Ra and Bhattacharjee, 2021).The RC pairs, $R_{1,2,3}$ and $C_{1,2,3}$, represent the polarisation resistance and the dynamic characteristics of the battery during charging and discharging (Zhang *et al*., 2015, Xiong *et al*., 2019, Delgado *et al*., 2022).

The battery dynamics refer to the various effects occurring during battery charging/discharging. The battery model is more complex during operation than it is during steady state and requires a higher order model to reflect these complexities. For example, concentration gradients of reactants on the electrode surfaces, known as concentration polarisation, can increase battery resistance (Huang *et al*., 2022). Addition of RC-pairs allows the battery model to more accurately predict such behaviours during battery operation.

Self-discharge is a phenomenon in which internal chemical reactions reduce the stored charge of the battery without any connection between the electrodes or any external circuit. In the case of VRFBs, this can also include shunt currents as well as parasitic current losses of the flow pump. These effects are represented by a parallel resistance R_{SD} to ground (Fornaro *et al*., 2022, Xiong *et al*., 2019).

2.2.2 Parameter Estimation

Parameter estimation involves determining the values of model parameters to accurately represent battery behaviour. Various approaches have been developed for this purpose. These include using sequential quadratic programming for electrical analogue models (Li *et al*., 2012), employing least-squares optimisation with consideration of system uncertainties (Fogelquist *et al*., 2023), and utilising neural networks like Long Short-Term Memory for real-time estimation (Chun *et al*., 2020).

Challapuram *et al*., (2019) describe parameter estimation as the process of determining the values of the parameters in the equivalent circuit model (ECM) that best represent the physical

behaviour of the VRFB system (Challapuram *et al*., 2019). It can also be described as the process of fitting an equivalent circuit model to experimental battery data by repeatedly simulating the model and using numerical optimisation to adjust the model parameters (Huria *et al*., 2013). Each iteration of the simulation then minimises the error between the simulated and experimental results.

The literature shows many examples of parameter estimation solving the component values of the Randles circuit. While some research papers employ the least squares method (Zhang *et al*., 2015, Xiong *et al*., 2019), others reference the literature to solve for some of the parameters (Challapuram *et al*., 2019). Xiong *et al*., (2019) for example, used a combination of the least squares method and particle swarm opimisation algorithms to identify model parameters (Xiong *et al*., 2019).

The least squares method minimises the sum of squared error between the simulated and measured terminal voltage (Zhang *et al*., 2015, Xiong *et al*., 2019). In the context of the VRB model, the least squares method solves the model parameters minimising the difference between the experimental data and the model predictions (Zhang *et al*., 2015).

CHAPTER 3 MODEL DEVELOPMENT

To develop the VRFB model a reference battery system was derived and developed based on a combination of experimental data and circuit modelling techniques (Section 3.1). Subsequently the reference battery was parameterised and configured based on the requirements (Section 3.2). Simulations were conducted (Section 3.3) to test the feasibility of the model concerning the micro-grid's requirements. The micro-grid refers to a building on the North-West University campus.

3.1 Electrical Equivalent Battery

An electrical representation of a VRFB was created using an ECM along with parameter estimation techniques, as described in Section 2.2. The ECM was used to model the battery dynamics and electrical characteristics of a VRFB. It was also used as a component in various simulations to test the battery dynamics when subjected to the electrical load of a building.

To create the ECM, a real VRFB system was first selected as a reference point on which to base the equivalent circuit. This battery system was then evaluated to study its electrical response under various conditions. The equivalent circuit was then created to simulate the same electrical response under the same conditions.

The experimental results captured by Gao *et al*. (2021) were used to model the electrical behaviour of the equivalent battery. The combination of the input current, terminal voltage and charge capacity captured during these experiments was used to describe the battery under charge, discharge, and no-load conditions.

3.1.1 Experimental Setup

Experiments conducted by Gao *et al*. (2021) included various situations where VRFBs were continuously charged and discharged, while measuring the voltage response. The battery characteristics during these experiments are represented in Table 3-1.

Table 3-1: Experimental VRFB properties (Gao *et al*., 2021)

Battery property	Units	Value
Electrodes		Graphite felt (GFD4.6)
Electrolyte		Vanadium sulphate ($V_2(SO_4)_3$)
Positive side volume	mL	50

Negative side volume	mL	50
Flow rate	$mL.min^{-1}$	20
Active area	cm^2	10
Operating temperature	°C	20
Current density	$mA.cm^{-2}$	100
Membrane type		Nafion®212

These experiments yielded numerous output signals that were captured continuously throughout the charging and discharging cycles. The experimental results of Gao *et al*. (2021) included data for the following parameters:

- Input current [A]
- Terminal voltage [V]
- Charge capacity [Ah]
- Discharge capacity [Ah]
- Timestamp [s]

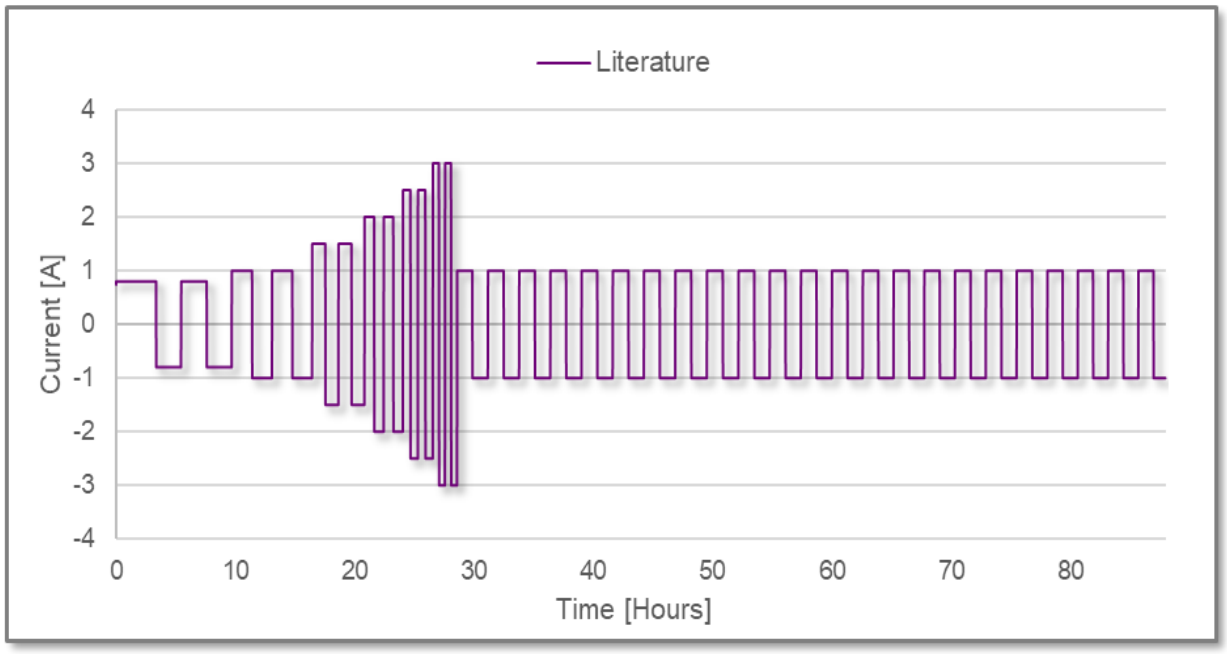

Figure 3-1: Experimental data - Charge and discharge current - Adapted from (Gao et al., 2021)

The charge and discharge current and voltage measurements from one of the experiments are shown in Figure 3-1 and Figure 3-2. These figures illustrate the nature of the charge and

discharge process that was applied to the VRFB respectively. An excerpt of the measurements can be seen in Appendix B.

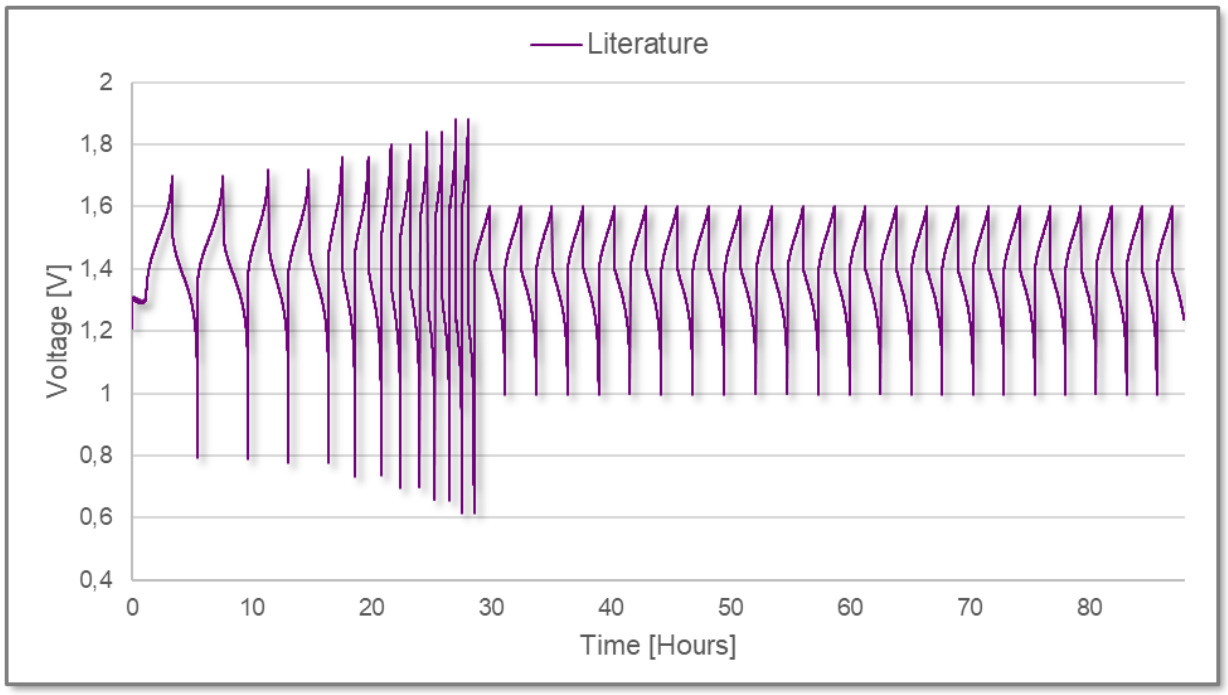

Figure 3-2: Experimental data - Charge and discharge voltage - Adapted from (Gao et al., 2021)

The current shown in Figure 3-1 corresponds with the voltage in Figure 3-2. Positive current indicates a charging input whereas negative current indicates battery discharge. During the transition phase between positive and negative input current, a brief steady-state period was applied, ranging between 10 to 20 seconds. Given the time scale of the experiments, the steady state period is not clearly visible in Figure 3-1 and Figure 3-2. The inclusion of the steady state period is useful in the modelling of the battery dynamics, since it provides insight into how the cell recovers from a load to no-load condition. The peak voltages in Figure 3-2 illustrate the overpotential of the battery during charging and discharging. Under steady-state conditions the battery voltage is expected to be 1.26 V at full charge Equation 2-4.

This is an example of the input currents applied to the VRFB in the experiments of Gao *et al*. (2021) and was selected based on the duration of the experiment and the variation of the applied input current. It was primarily intended to test the capacity retention of the VRFB with varying charge-discharge cycles. Therefore, the applied input current was varied in both magnitude and the frequency in the cycle between charging and discharging.

3.1.2 State of Charge (SoC)

The SoC refers to the ratio between the available charge and the maximum charge capacity of the cell (Fornaro et al., 2022, Sangwon, 2019). The SoC is calculated using the following equation:

$$\boldsymbol{SoC(t) = \frac{Q(t)}{Q_{Max}}} \qquad \textbf{3-1}$$

With $Q(t)$ [Ah] the charge capacity at the time t, and Q_{Max} [Ah] the maximum charge capacity of the cell. The state of charge is a dimensionless ratio, between 0 and 1, that typically indicates how much charge is remaining within the cell.

3.1.3 State of Health (SoH)

The maximum charge capacity of the battery Q_{Max} [Ah] may deteriorate over time due to various factors, including Vanadium crossover (Wang et al., 2024) and imbalanced Vanadium active species (Luo et al., 2013). The maximum charge of the battery Q_{Max} at a certain SoH may be different from the maximum charge at another SoH. The SoH is calculated by comparing the maximum retainable charge to the rated capacity of the battery (Puleston et al., 2022):

$$\boldsymbol{SoH = \frac{Q_{Max}}{C_r}} \qquad \textbf{3-2}$$

Here, C_r [Ah] denotes the rated capacity of the cell. Since SoH is a ratio, and therefore dimensionless, a SoH of 1 would typically refer to 100% capacity retention and no decay.

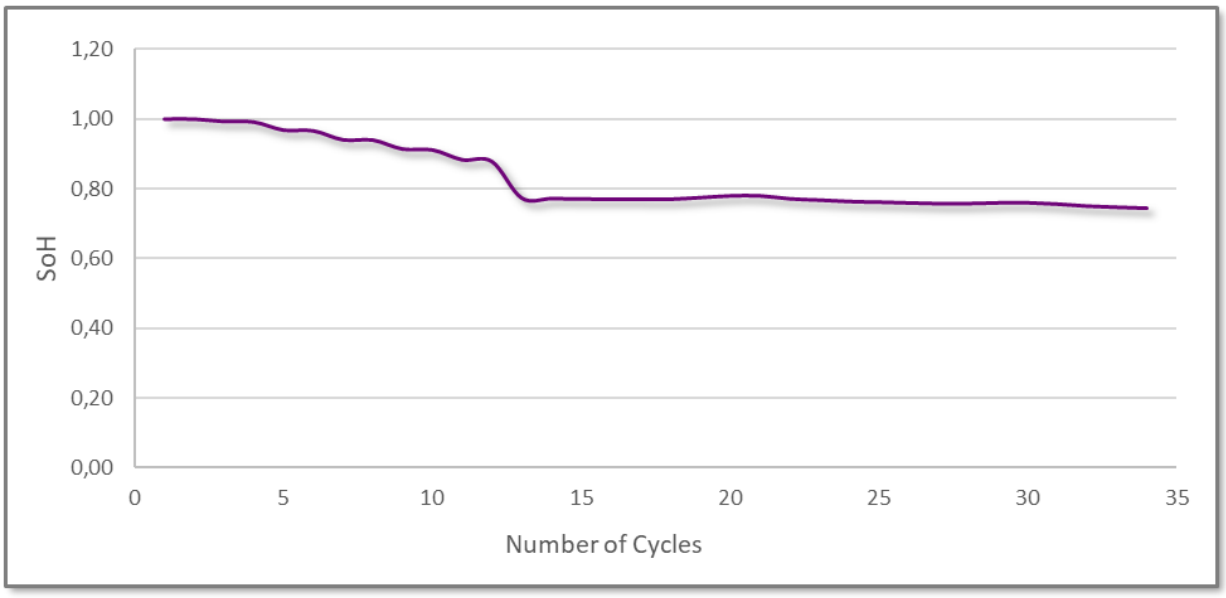

Figure 3-3: Experimental Data - SoH - Adapted from (Gao et al., 2021)

Figure 3-3 shows the measured SoH of the VRFB corresponding to the experiments detailed in Figure 3-1 and Figure 3-2. The figure indicates that the SoH decreases significantly during the first 12 cycles, and then stabilises.

3.1.4 Equivalent circuit model (ECM)

An ECM was designed to model the electrical battery dynamics of the VRFB. Simscape™ was used to create the battery component and parameterise the different phenomena that influence the VRFB system. Simscape™ is a toolbox available in MATLAB® that provides numerous electrical components. It aided in the design and use of electrical circuits that would simulate the behaviour of the battery model.

As described in Section 2.2.1, the ECM topology depicts the circuit components required to describe the battery characteristics. Expanding on the ECM topology used by Yesilyurt and Yavasoglu (2023), a similar design as shown in Figure 3-4 illustrates a Randles equivalent circuit with 2nd-order RC pairs corresponding to the circuit discussed in Section 2.2.1 above. To increase the accuracy of the battery dynamics, two RC pairs were implemented as opposed to the single pair by Yesilyurt and Yavasoglu (2023). The above would, corresponding to the Randles equivalent circuit, provide better accuracy at the cost of model complexity (Section 2.2.1). The higher order model is necessary for better accuracy during state transitions and changes in electrolyte flow rate. The series resistor (R_0) models the battery's internal resistance, while the parallel resistor (R_{sd}) represents the parasitic losses such as battery degradation and self-discharge (Yesilyurt and Yavasoglu, 2023).

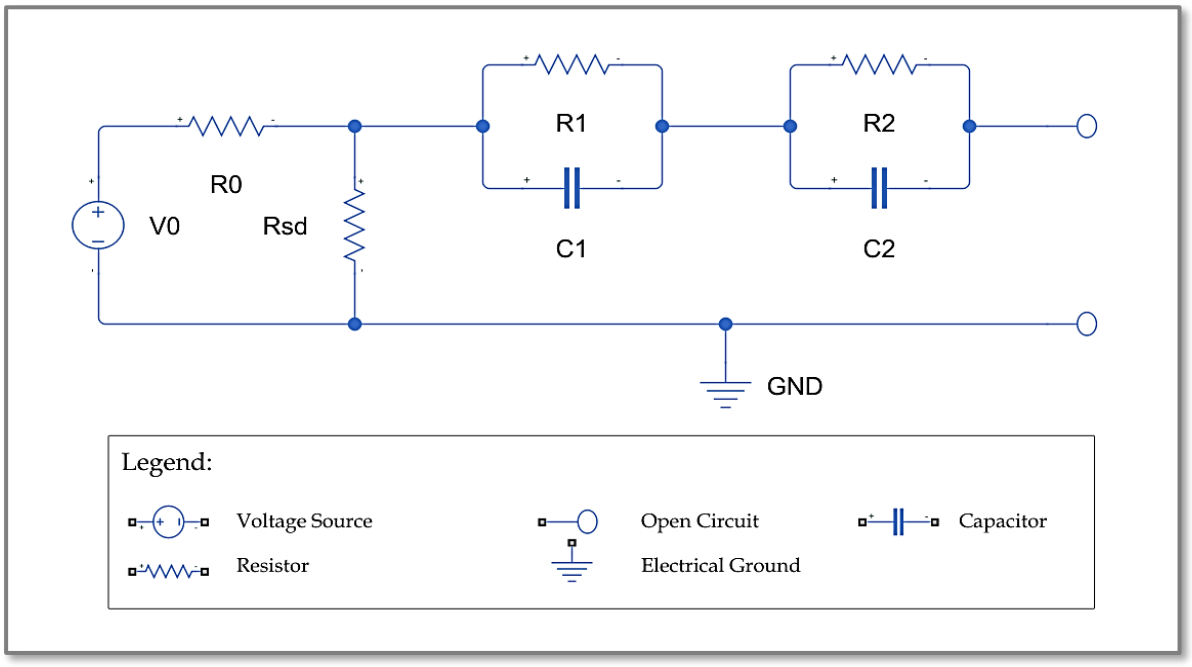

Figure 3-4: ECM circuit topology

Figure 3-4 illustrates the electrical circuit topology of an ECM, generated in MATLAB® (R2023a). Simscape™ toolbox includes a component called a table-based battery, which encapsulates the circuit in Figure 3-4. The use of this component simplifies the circuit into a single subsystem that exposes the internal circuit components as parameters.

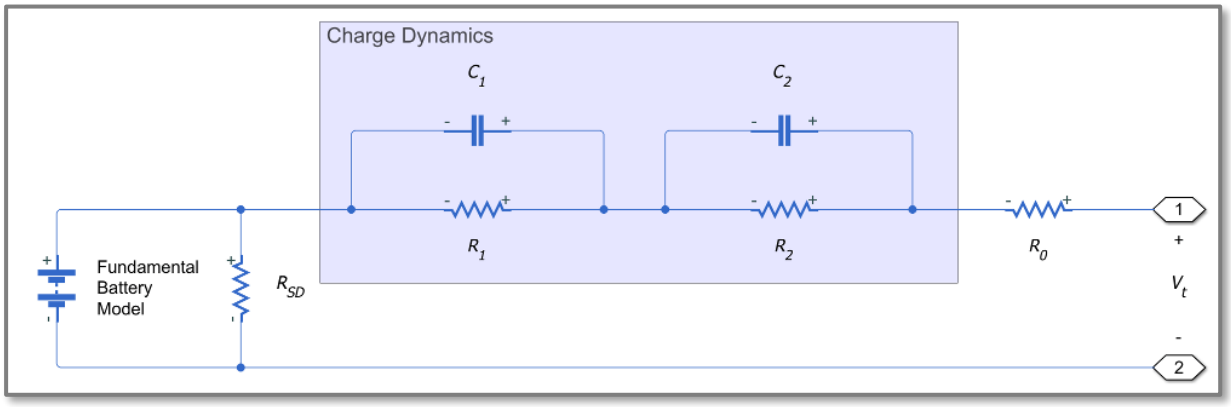

Figure 3-5: Table-based battery – Simscape™ (MathWorks, 2024)

The internal circuit of the table-based battery shown in Figure 3-5 is electrically identical to the ECM circuit shown in Figure 3-4. This means that the table-based battery component can be used to represent the ECM topology. The table-based battery component shown in Figure 3-5 makes use of a lookup table to derive its internal circuit parameters. The lookup table is state of charge (SoC) dependant and contains columns for each circuit parameter to be modelled. The table can be configured to provide values for the circuit parameters at any SoC value between 0 and 1. The accuracy of the circuit parameters increases with the number of distinct SoC values in the table. This results in an *M x N* matrix of circuit parameters with M as the number of circuit parameters and N as the number of distinct SoC increments.

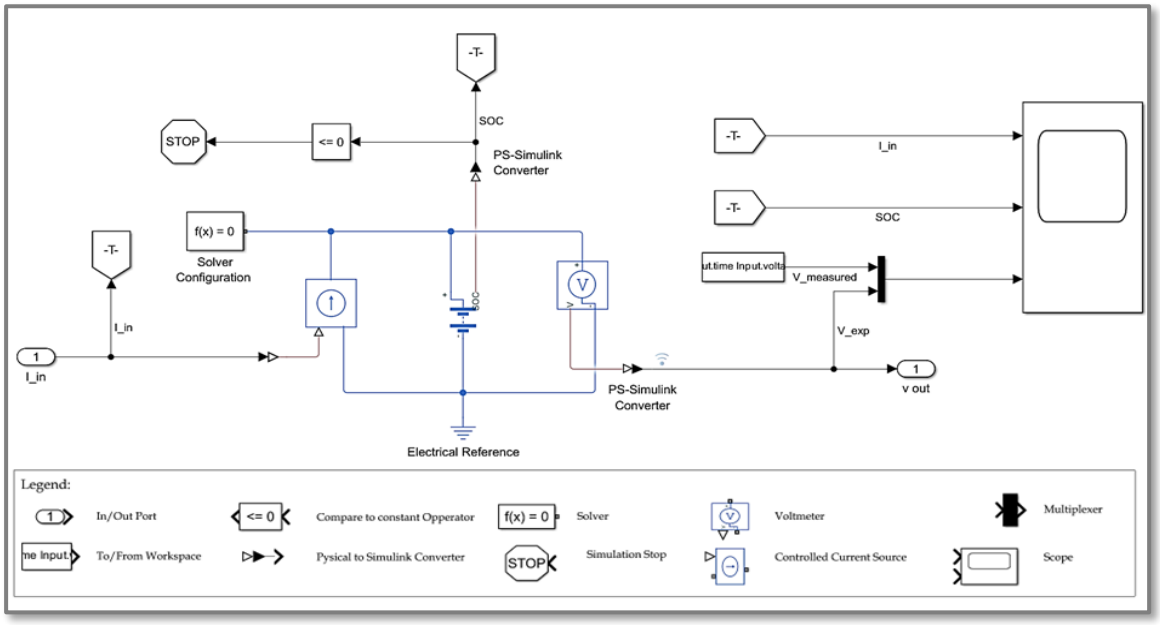

Figure 3-6: Simulink™ topology Illustration

Figure 3-6 illustrates the Simulink™ simulation that evaluates the ECM's voltage response. Using the Simscape™ table-based battery component, a simple Simulink™ circuit was created to measure the terminal voltage of the battery during charge, discharge, and no-load states. The model involves the battery as well as a current source to provide the charging power (or discharging power if programmed to supply negative current). The simulation was configured to stop whenever the SoC of the battery reached 0. The circuit also contains some utility components such as scopes (to visualise data in graphs), solvers, and workspace references (to export data), which are all required to run the circuit simulation in Simulink™.

3.1.5 ECM Parameters

To model the capacity loss and discharge characteristics, the model parameters were chosen to correlate with the experimental measurements in Section 3.1.1. A parameter that describes the maximum charge capacity, as seen in Equation 3-2, was defined as a function of the number of charge-discharge cycles (n).

$$\boldsymbol{Q_{max}(n) = SOH(n)C_r} \qquad \textbf{3-3}$$

The self-discharge resistance illustrated in Figure 3-4 was modelled as a constant parameter. This increases the weight of the capacity loss parameter (Equation 3-3) since it is the sole descriptor of the parasitic effects of battery ageing.

The Simscape™ battery component makes use of time constants as parameters, such that:

$$\boldsymbol{\tau_X = R_X C_X \ [s]} \qquad \textbf{3-4}$$

with τ_x the time constant [seconds], R_x the resistance [ohms] and C_0 the capacitance [Farad]. The circuit parameters are influenced by the SoC and temperature of the battery. The battery temperature was assumed constant in accordance with Yesilyurt and Yavasoglu (2023). Therefore, the components from Figure 3-4 are considered functions of SoC:

$$\boldsymbol{V_0(SoC) \ [V]} \qquad \textbf{3-5}$$

$$\boldsymbol{R_0(SoC), R_1(SoC), R_2(SoC) \ [\Omega]} \qquad \textbf{3-6}$$

$$\boldsymbol{C_1(SoC), C_2(SoC) \ [C]} \qquad \textbf{3-7}$$

The SoC values were limited to increments of 0.1, resulting in 10 possible values ranging from 0.1 to 1. This allows the SoC influenced parameter set to be expressed as a 6x10 matrix, which is employed in the parameter estimation (Section 3.1.6). The maximum charge capacity (Equation

3-3) was be modelled in a set of charge-discharge cycles of [0, 5, 10 ,15]. The set of 4-cycle increments covers the range of cycles available in the experimental data sample set (Section 3.1.1) and offers a balance between model complexity and accuracy.

3.1.6 Parameter Estimation

Utilising the measured terminal voltage output presented in Section 3.1.1 with the ECM simulation depicted in Figure 3-6, allows the circuit parameters to be solved. The MATLAB® parameter estimator was used to solve the circuit parameters. It was configured to iteratively compare the circuit voltage response to the measured terminal voltage for the same input. The least squares method was configured as the method of approximation. For each iteration, a new set of circuit parameters was configured based on the total error returned by the least squares function.

The parameter estimation setup required adding all parameters as one-dimensional arrays in the MATLAB® workspace. The measured current acted as the input to the model as well as the parameter estimator. The measured terminal voltage was compared with the model's output signal.

Initial values were configured for each function in Equations 3-3 to 3-7. This was the basis for the first iteration as described above. More accurate initial values typically result in a quicker estimation.

Table 3-2: Parameter Estimation – Initial parameters selection A

Parameter	Value	Unit
SoC	0.1, 0.2 … 1.0	-
V_0	1.3	V
R_0	10	$m\Omega$
R_1	50	$m\Omega$
R_2	10	$m\Omega$
R_{SD}	100	Ω
τ_1	100	s
τ_2	100	s

The initial values are shown in Table 3-2 and Table 3-3. Table 3-2 is used to describe the circuit component parameters as it relates to equations 3-4 to 3-6 while Table 3-2 describes the initial values of the capacity loss (Equation 3-3). The initial values were within the range of the values configured by (Yesilyurt and Yavasoglu, 2023).

Table 3-3: Parameter Estimation – Initial parameters selection B

Cycles	C [Ah]
0	1.90
5	1.81
10	1.78
15	1.69

The model was validated by testing its output with an independent set of VRFB measurements known as the validation dataset. The accuracy of the model with an independent set of measured input current and measured terminal voltage determines its general accuracy.

3.2 Battery Configuration

The battery configuration includes, *inter alia*, the configured capacity and current throughput of the battery system. The configuration is therefore context-specific based on the grid that the battery is connected to. The configuration parameters were determined by selecting a building as the micro-grid, and modelling the configuration parameters based on the building's power usage data. The building is located on the campus of the North-West University in South Africa and represents a micro-grid that is subject to rolling blackouts of the national grid and is referred to as 'the building' in Section 3.2.

3.2.1 Capacity

This chapter focuses on the study of the building's power requirements, and how the capacity was ultimately derived from a model of its past energy usage statistics. It includes possible auxiliary power systems, such as the generated power by the campus' solar panel array as well as the effects of power outages on the energy consumption metrics.

It is assumed that when an outage occurs, with the modelled battery installed and linked to the building's electrical system, the building would continue its normal operation as if no outage had occurred. Therefore, the required battery capacity was interpreted as the total energy that would have been consumed if an outage had not occurred.

Additionally, the power generated from the campus' solar panel array is included as a possible source of generated power. This allows the model to include generative sources as an additional parameter. The effects of power outages are also included in the examination of the building's power usage.

3.2.1.1 Consumption Data

This building was specifically selected as it was already equipped with a smart metering system that allowed for the retrospective collection of power data. From its history of power measurements, timestamped measurements that indicate the power being consumed [kW] were exported. The exported sets contained measurements at 30-minute intervals over a period of 3 weeks (Appendix C).

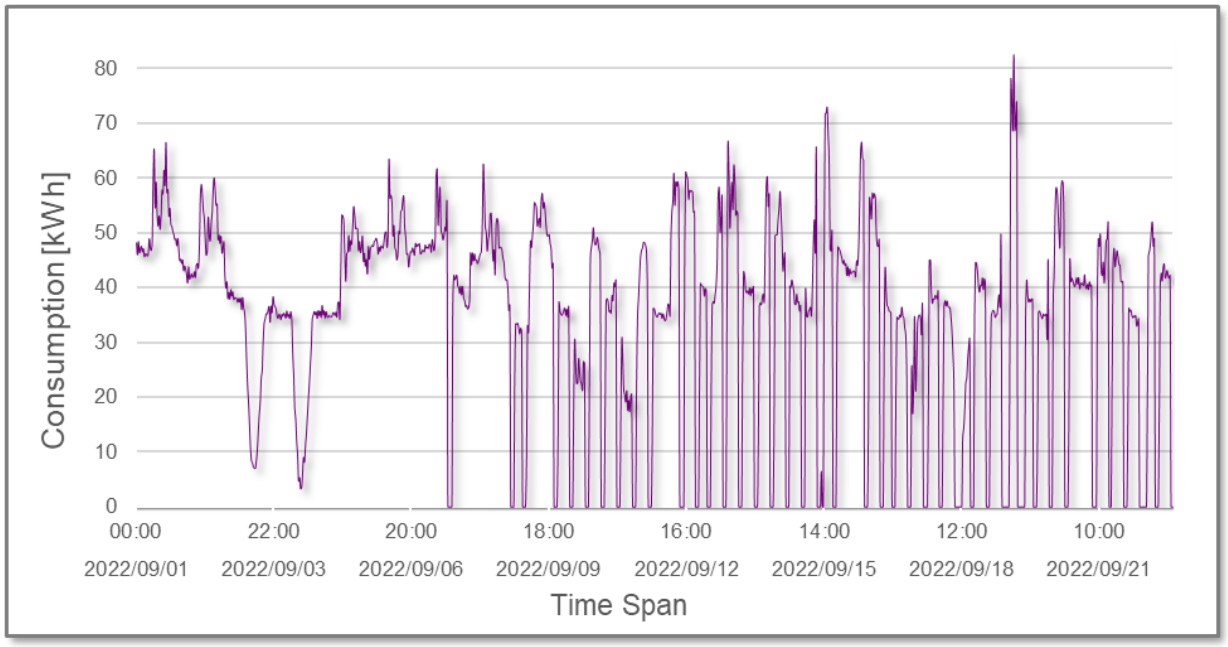

Figure 3-7: Grid power consumed by the N1 campus building from 01/09/2022 to 22/09/2022

Figure 3-7 shows the power [kWh] consumed by the building from 01/09/2022 to 22/09/2022. The building was not subject to any power system other than the national grid during this period. At the later part of the 3-week period, 0 kWh measurements for 2- and 4-hour periods can be observed. During normal operation of the building, power consumption is expected during all hours. The 0 kWh measurements are assumed to be the effect of grid outages (and not data capture error) due to the 2- to 4-hour periods of outages corresponding with the national grid outages that were expected during that time in 2022.

3.2.1.2 Generation Data

To model the effects of a generative power source attached to the battery system, the power generated by the campus' solar panel array (HySA Solar PV) was collected. The generation data was exported as timestamped power measurements [kWh] in 15-minute intervals (Appendix D).

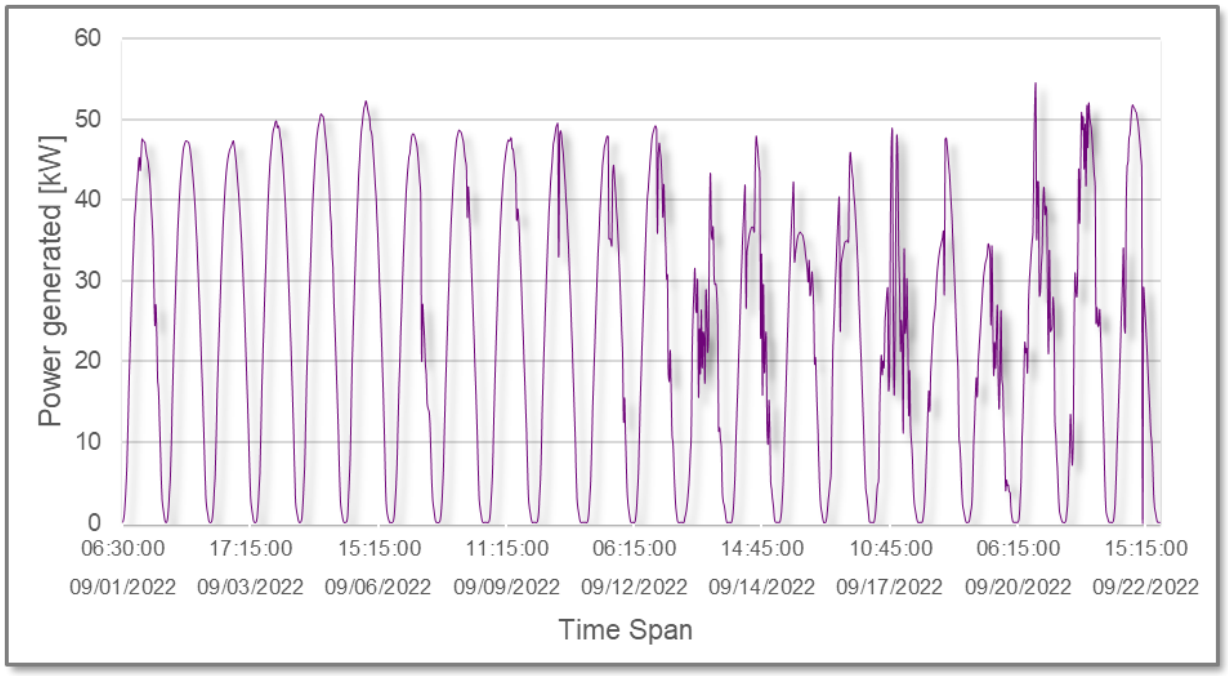

Figure 3-8: Solar power generated from 01/09/2022 to 22/09/2022

An excerpt of the generated solar power measurements is shown in Figure 3-8. The day-night cycle can be observed in the frequency of the solar power data. The measurements indicate that the solar power is more stable during the 3-week period than the grid power shown in Figure 3-7. In comparison with the consumed grid power shown in Figure 3-7 the peak generated power is not sufficient to satisfy the load conditions on its own. To satisfy the load conditions the battery system must therefore be able to also store grid power in addition to renewable sources.

3.2.1.3 Data Normalisation

The consumed and generated power data was formatted so that it could be represented as a 24-hour period. It is assumed that this period represents the power consumed by the building on an average day, including the effects of solar power. The average day was used as a template on which to test the response of the battery under simulated load conditions.

Data cleansing strategies were performed to minimise the effects of power outages and other outliers on the sample set. Zero points were identified and entire days containing zero points were removed from the sample set. Both the consumed and generated data sets were split by day based on their timestamps. Afterwards, the measurements were compared to their corresponding measurements of the same time on different dates. This allowed for the calculation of the average power consumption at any given time of the day. The average consumed power at time t can then be calculated using:

$$P_t = \sum_n^1 \frac{P_{t,n}}{n} \qquad 3\text{-}8$$

In Equation 3-8, *P* denotes the power [kW], *t* denotes the time of day and *n* the day in the sample. The power at any time of the average day is calculated as the average of the power measurements on that time of the day. This also causes the power calculation to be date independent.

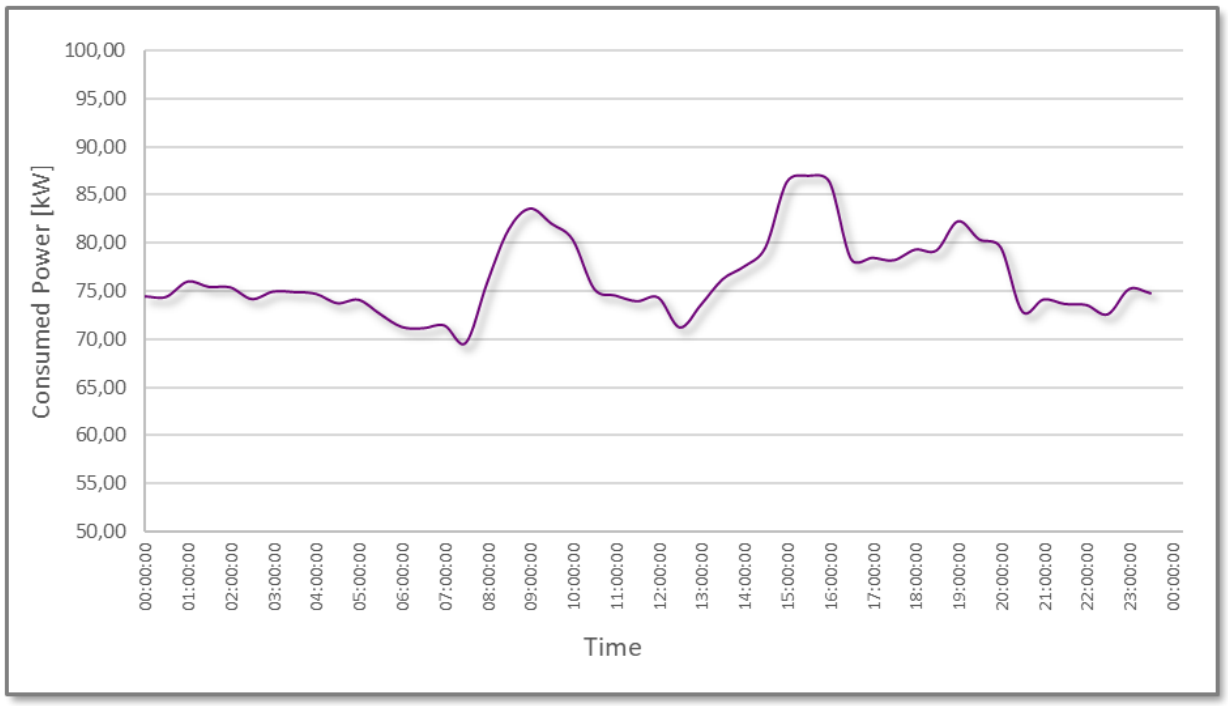

Figure 3-9: Representation of a statistically average day's power consumption

Figure 3-9 illustrates the calculated power consumed in an average 24-hour period. These values were utilised to determine the consumed power [kW] at any given time of the statistically averaged day. Additionally, it also provides insight into the maximum power that is typically consumed at a single point during the average day shown in Figure 3-9.

The consumed power in Figure 3-9 includes the power measurements during assumed outage periods, which can affect its accuracy. Furthermore, it is also assumed that the occurrence of a power outage during the day affects the power usage of the whole 24-hour period. These effects can range from power surges after the outage has ended to users adjusting their power usage in their day. To ensure maximum reliability in the sample set, all days (24-hour periods) containing power outages were removed from the sample set. This also allows the sample to maintain its integrity in that it only contains full days, resulting in the same number of data entries for each calculated time in Equation 3-8.

Furthermore, power measurements were categorized based on the same time of day for the entire sample set. For this sample, after excluding days with zero points, no measurement exhibited a variance exceeding 2σ.

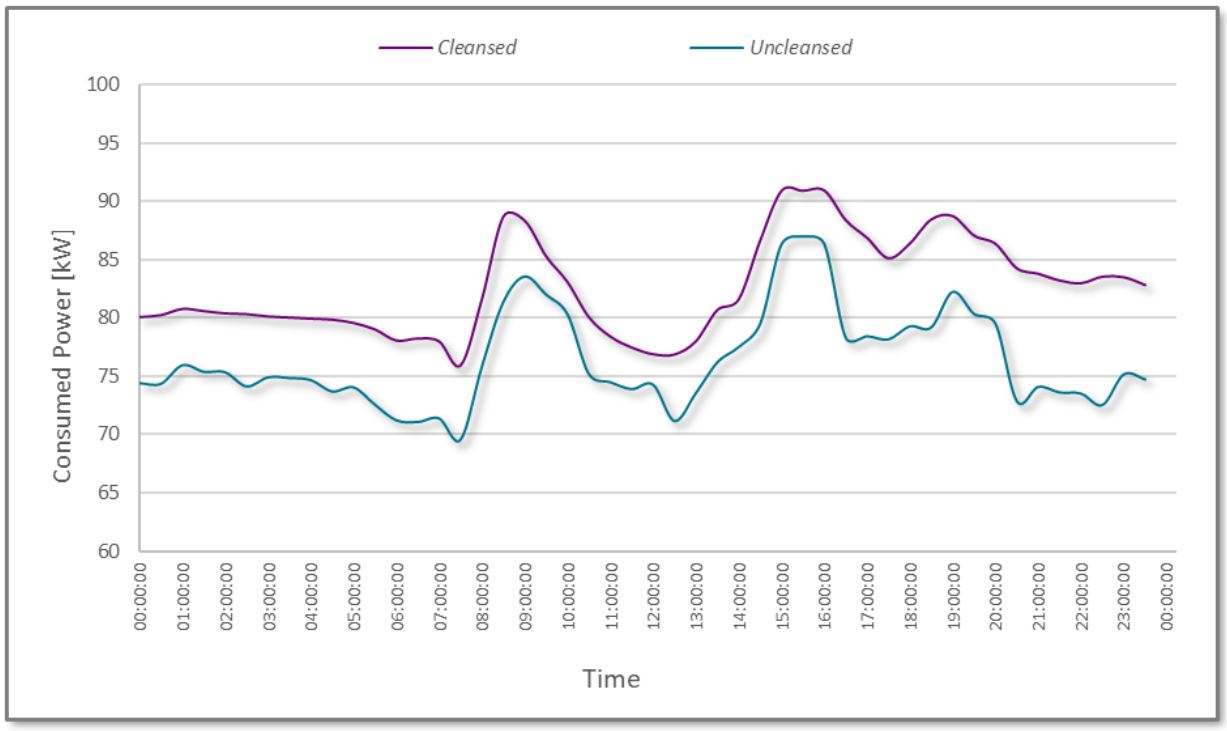

Figure 3-10: Average Consumed Power – Cleansed vs Uncleansed

Figure 3-10 illustrates the effect of removing only the days containing power outages from the set used previously in Figure 3-9. This was done by repeating the average day calculation using both the full (uncleansed) and revised (without outage days) datasets. Therefore, the average consumed power at any given time during the day is decreased due to the removal of zero points, but the smoothing of the curve also indicates significant changes in consumption behaviour.

MATLAB® scripts (Appendix A) were utilised to transform the datasets into classes that would describe a simulation based on power consumed and generated at any given point during the simulated day. The sample sets were integrated into a single generalised representation of the building's power characteristics on an average day.

The consumed power and generated power were captured with different sample frequencies. To compensate for this, the retime function was used to transform both datasets so that they could be represented with a sample period of 1 minute. The retime function linearly interpolates datasets so that data may be presented at a higher frequency.

The consumed grid power was calculated by summing the average daily solar generation- and consumed grid power (after cleansing) of the building at each time interval as shown in Figure

3-11. The generated solar power decreases grid demand resulting in a lower consumed grid power during daylight hours. The calculated consumed power in Figure 3-11 was used to drive simulations on the effectiveness of the battery model.

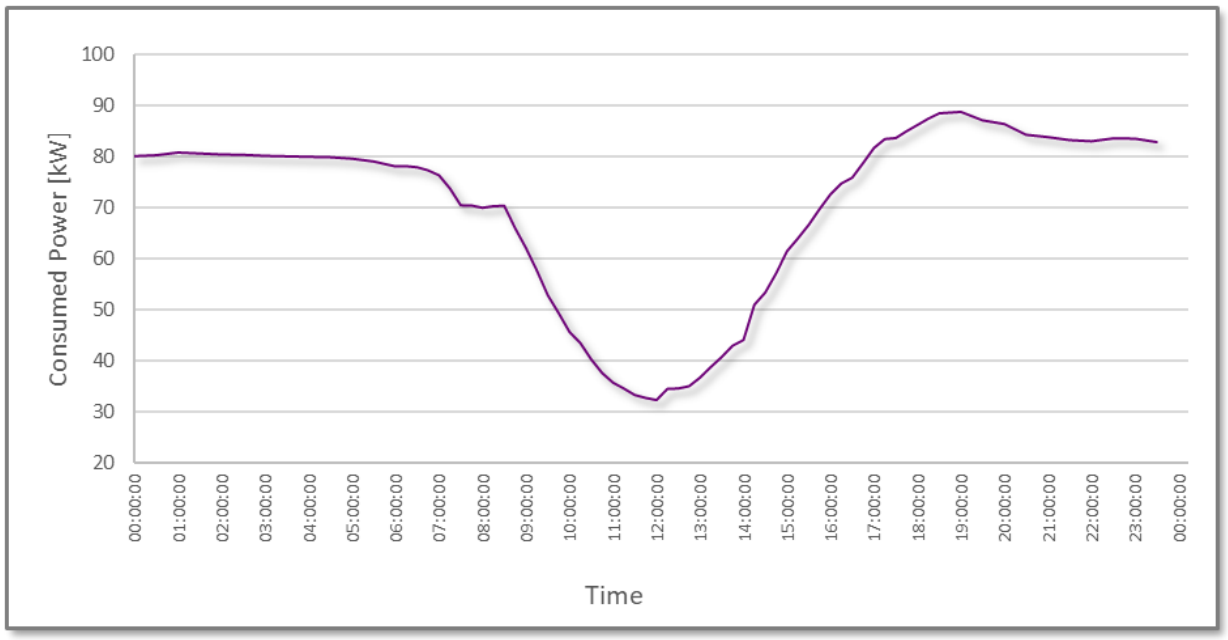

Figure 3-11: Average day consumed grid power including solar power

3.2.1.4 Power Outages

The total energy required by the building can be expressed as the energy consumed by the building where no outage had occurred. It may be expressed as the integral over the consumed energy *P* during the period *t* of an outage equation 3-9, providing:

$$\int_{t_2}^{t_1} \boldsymbol{P(t)dt} \qquad \textbf{3-9}$$

To calculate the required capacity of the battery, the combined power characteristics from Figure 3-11 were integrated over the outage period. Because the power consumption is inconsistent throughout the day, a MATLAB® script was developed to identify which outage period would result in the largest integral, for a given duration. MATLAB® window functions to evaluate fixed width integrals over the entire day.

3.2.2 Stack Configuration

The stack configuration determines the size, quantity, and topology of the electrodes. This ultimately determines the maximum current throughput that the stack could support. To establish

the maximum current throughput that the building consumes, the maximum power consumed (Figure 3-11) must be scrutinised.

$$\boldsymbol{P = IV} \qquad \textbf{3-10}$$

Power may be expressed as the product of voltage and current (Equation 3-10). The voltage of the building's power may be factored into Equation 3-10 to calculate the maximum current required. This gives the maximum current I_{max} required as:

$$\boldsymbol{I_{max} = \frac{P_{max}}{V}} \qquad \textbf{3-11}$$

with P_{max} the maximum power consumed at any point during the average day.

To determine the stack topology, the current and voltage requirements of the battery system must be considered. In a circuit, the number of cells in series determines the voltage. By incorporating the required voltage of the cell, the number of series cells may be represented by Equation 3-12

$$\boldsymbol{N_{series} = \left\lceil \frac{V}{V_{cell}} \right\rceil} \qquad \textbf{3-12}$$

with N_{series} the approximated number of cells to supply the voltage V and V_{cell} the voltage per cell. Similarly, the number of parallel cell stacks (stacks of N_{series}) may be calculated by incorporating the required current. Equation 3-13 may be used to calculate the number of parallel stacks so that:

$$\boldsymbol{N_{parallel} = \left\lceil \frac{I}{I_{cell}} \right\rceil} \qquad \textbf{3-13}$$

with $N_{parallel}$ the number of parallel stacks and I_{cell} the current that each cell supplies. The current provided by each cell may be expressed as the product of the current density J [$A.m^{-2}$] and the total area of the electrodes of the cell [m^2]. Thus:

$$\boldsymbol{I_{cell} = A.J} \qquad \textbf{3-14}$$

Combining Equations 3-11, 3-12, 3-13 and 3-14 the number of parallel cells may be expressed as:

$$N_{parallel} = \left\lceil \frac{\left(\frac{P_{max}}{V_{cell} N_{series}}\right)}{A\,J} \right\rceil \qquad 3\text{-}15$$

Equation 3-15 can be used to calculate the number of parallel cell stacks (each with N_{series} series cells) that is required to satisfy the electrical load requirements of the building. Since Equation 3-15 has the current density J as a parameter, it can be re-used to calculate the stack topology for varying electrolytes.

3.3 Simulations

The Simulink™ package was used to create various simulations, respectively simulating different operating conditions to which the battery will be subject to. These conditions include the charging of the battery during sustained grid power, the discharging of the battery when under full load of the building, the battery fade and capacity retention after extended use and the simulated day's usage, including multiple power outages and solar generation.

3.3.1 Setup

To facilitate simulations, custom simulation classes were created in the MATLAB® workspace. These can provide the expected generated and consumed power as a function of time. Additionally, they are set up to provide consumed power data only during the programmed power outage periods. These simulation classes were used as the drivers of the simulations, allowing various scenarios to be repeated on the same simulation model, but with varying drivers.

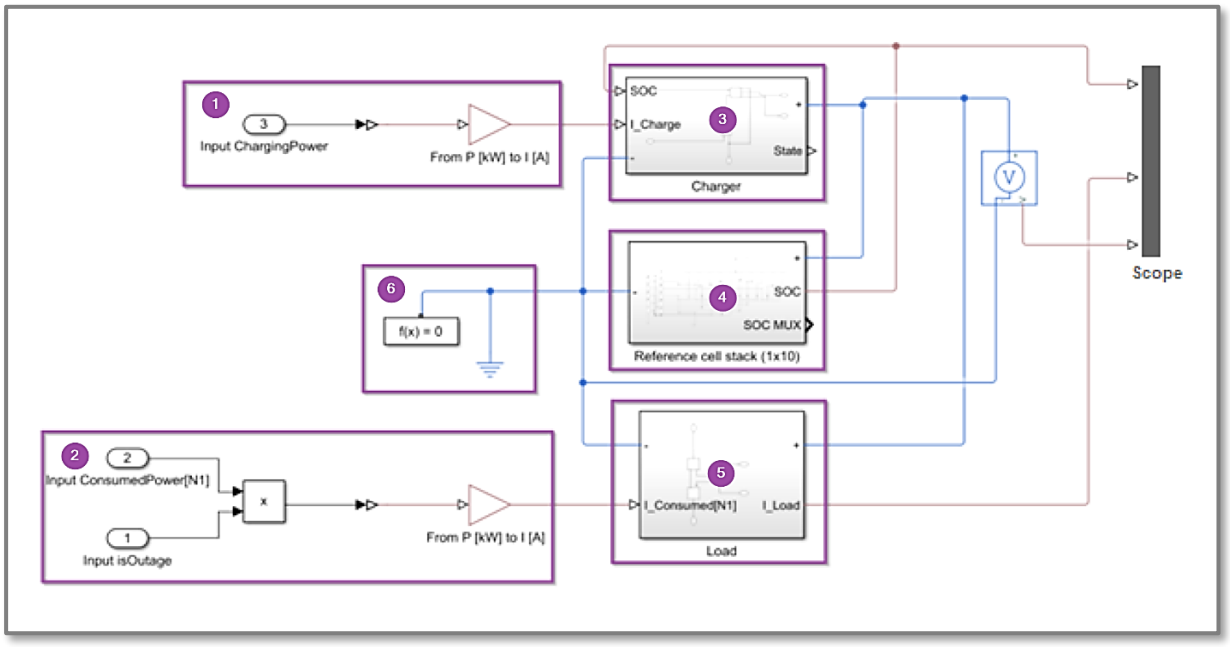

Figure 3-12: Simulation setup

A Simulink™ model was created as seen in Figure 3-12. The 5 major components of the simulation configuration are discussed in sections 3.3.1.1 to 3.3.1.6 along with the Simulink™ simulations configuration that was used.

3.3.1.1 Input charging power

The power generated by the charger is governed by an input signal (which is driven by the simulation class discussed earlier). The signal was converted from power to current, conforming to the charger component. By incorporating the building's voltage of 230 V into Equation **3-11**, the input charging power was calculated.

3.3.1.2 Input consumed power

The input consumed power refers to the power that will be consumed by the battery system. The conversion from power to current (that is required by the Simulink component), Equation **3-11** was solved with a voltage of 230V. The consumed power input also included a control signal that governed whether the power outage started and stopped. By calculating the product of the input signal and the control signal, the consumed power is calculated during outages and no power is consumed during normal operation. This may be expressed by Equation 3-16:

$$\boldsymbol{I_{consumed}} = \frac{\boldsymbol{P_{building}}}{\boldsymbol{230V}}(\boldsymbol{\alpha}), \qquad \textbf{3-16}$$

with α = [0, 1]

3.3.1.3 Charger

A charger component was implemented to provide positive current to the battery system. The charger was driven by the charging power input (in Section 3.3.1.1) and included additional componentry to regulate its output current.

Figure 3-13 illustrates the charger component that provides positive current to the battery system. It is driven by the input signals (I_{Charge}) used in the simulation and uses a controlled current source to determine the current provided. It does, however, also use a switch to prevent overcharging the battery system. The switch (controlled by the SoC of the battery) opens the charging circuit connection when the battery is fully charged.

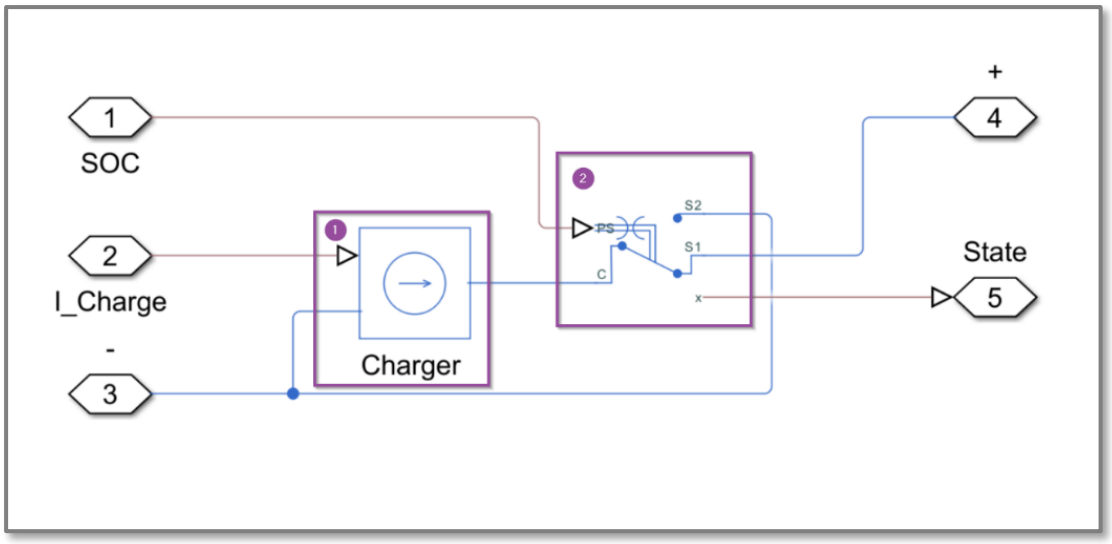

Figure 3-13: Simulation setup - charger

3.3.1.4 Cell stack

The battery system is comprised of numerous cells configured in a certain topology to produce the required voltage and current. The battery (modelled in Section 3.1) was used as a reference component. Numerous cells were configured, each referencing the single battery configuration previously configured, allowing configurations to make use of a single source.

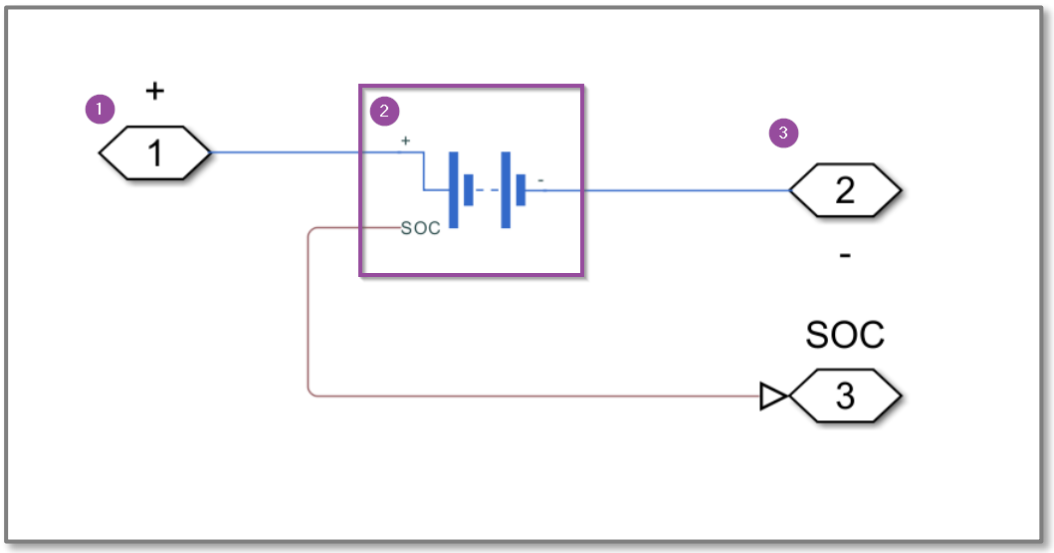

Figure 3-14: Simulation setup - reference cell

Figure 3-14 illustrates the reference cell. It was configured as a wrapper, exposing the positive, negative and SoC signals from the original battery component, respectively. Copies of the reference cell were implemented in series and parallel configurations. One such cell stack configuration is illustrated in Figure 3-15, where the reference cells (Figure 3-14) are configured

in series. This allows the cell stack to provide more voltage, as is expected of a series combination of batteries.

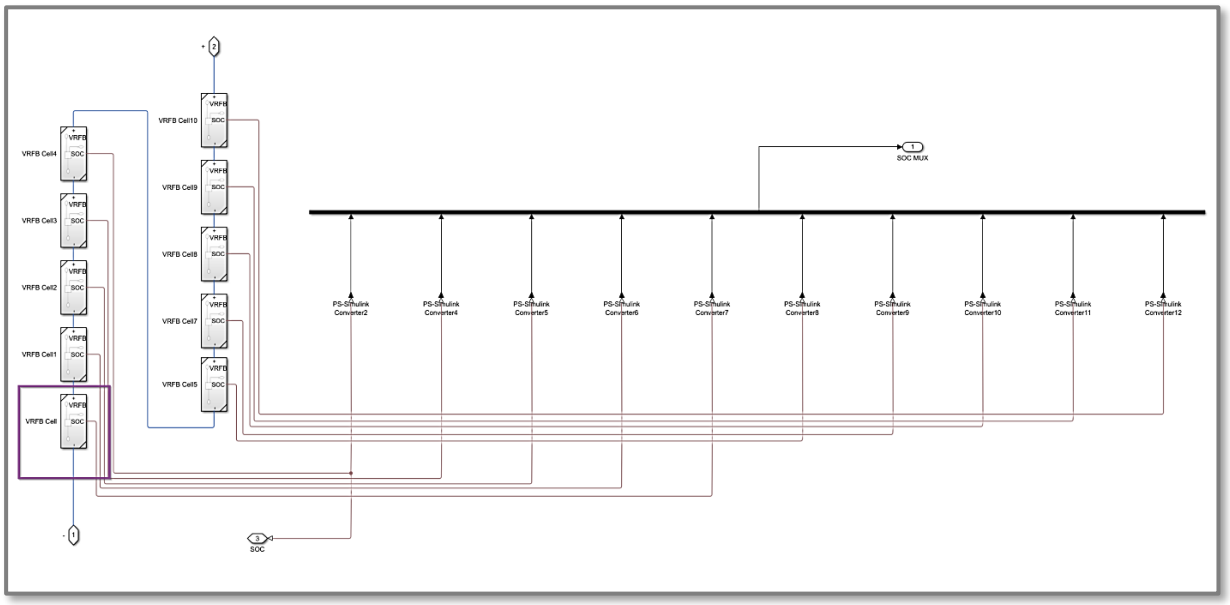

Figure 3-15: Simulation setup - reference cell stack - series

The stack in Figure 3-15 also features a multiplexer, which combines the SoC signals of each of the cells into a single multiplexed signal. The multiplexed signal is exposed (top of the stack) while a single SoC value is also exposed (bottom of the stack). This allows the external components to consume a single- or all SoC values.

3.3.1.5 Load

The load component was configured to simulate the consumed power by implementing a controlled current source. The current source was configured to provide negative current as a means of simulating power consumption.

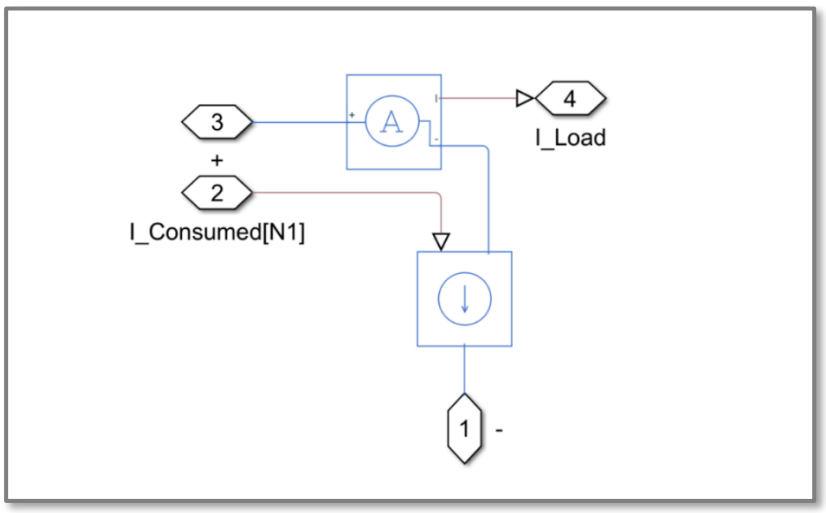

Figure 3-16: Simulation setup – load

Power data provided by the simulation class as (discussed in Section 3.3.1) was employed to drive the current source. Figure 3-16 illustrates the load component configuration, together with its input and output signals. It also features a current metering component that outputs the current flowing through the load.

3.3.1.6 Data measurement

To collect and measure the simulation data, various output signals were connected to scope components in Figure 3-17. The signals comprise of the SoC of the battery system, the current through the load, the voltage over the load and the total consumed power of the battery. Consumed power is calculated by the integral of the product of the current and voltage as shown in Equation 3-17.

$$E = \int P\,dt = \int IV\,dt \qquad 3\text{-}17$$

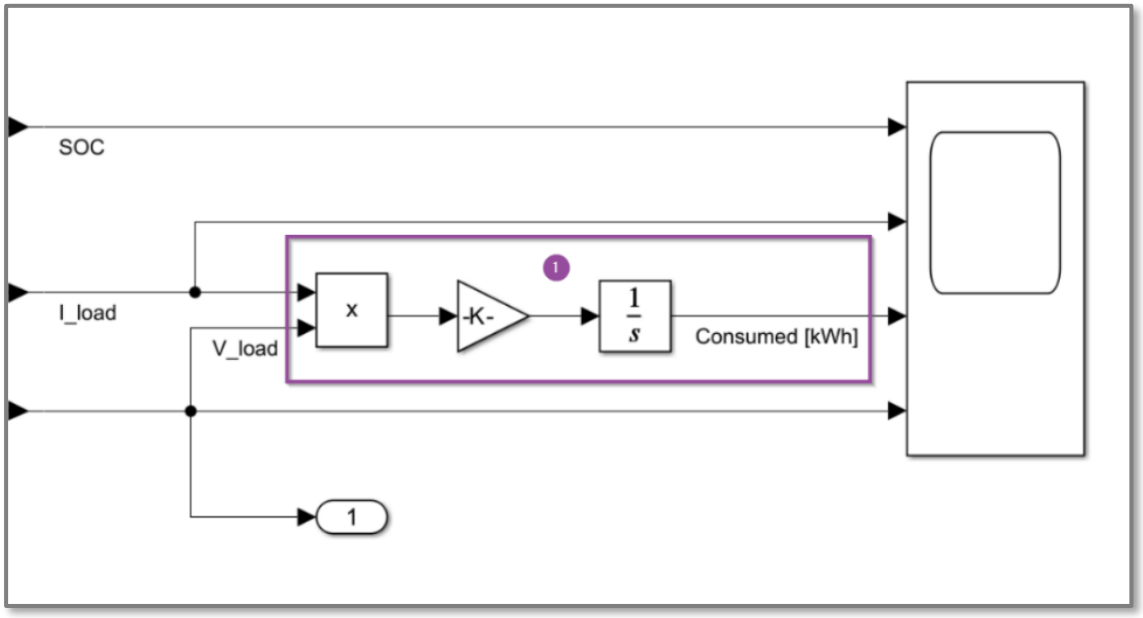

Figure 3-17: Simulation setup – scope

Figure 3-17 illustrates Equation 3-17 in the form of Simulink components used to transform the output signals of the system. The figure shows that a combination of a product, gain and integrator components were implemented to calculate the total consumed power E [kWh].

3.3.2 Charging and discharging

To simulate charging and discharging, simulations that were created that involved charging the battery from a low- to high-SoC and *vice versa.* The charge time and response were captured and measured.

3.3.3 Capacity retention

The capacity retention was simulated by continuously charging and discharging the battery. During this simulation, the amount of stored energy at full SoC was measured. The change in capacity over the number of cycles indicates the capacity retention of the battery model.

$$F_{retension} = \frac{C_{t0}}{C_t} \quad \text{3-18}$$

Here, $F_{retension}$ signifies the retention factor (unit-less), C_{t0} the initial capacity and C_t the capacity after the loss in capacity retention has been calculated.

3.3.4 Outage case studies

To simulate outages, various outage scenarios were created and run separately. These can range from single to multiple outages with different durations. The simulation tests the battery's response to the change in power, as well as testing the battery's capacity.

Power outage scenarios were selected and used as a basis from where the power requirements for each specific scenario were calculated. The required battery capacity per scenario was calculated using the total power required during the outage as a basis. The SoC operating range (discussed in Section 3.1.1) of the battery was factored into the capacity calculation

The required capacity C_E in [Wh] is calculated by:

$$C_E = \frac{E_{outage} F_{retension}}{(SoC_{max} - SoC_{min})} \quad \text{3-19}$$

Here, E_{outage} denotes the total consumed power [*Wh*] during the power outage and $F_{retension}$ the capacity retention factor as determined in Equation 3-18.

CHAPTER 4 RESULTS AND DISCUSSION

In this chapter, the results of the study are discussed in the context of the aims and objectives set out in Section 1.3. The results section details the system requirements of a VRFB for a micro-grid (Section 4.1), the factors that influence the performance of the VRFB system (Section 4.2) as well as the model results obtained in modelling simulations Section 4.3.

4.1 Requirements of a VRFB system for a micro-grid

The micro-grid refers to a building on the campus of the North-West University. The system requirements, such as capacity, electrolyte volume, electrode surface area, and efficiency were determined. These were derived by analysing the historic usage data of the building along with power outage simulations. The power rating of a battery indicates its maximum immediate power at peak load, while the energy rating reflects its total capacity. The VRFB's capacity and power rating are modelled independently.

4.1.1 Capacity

In Section 3.2.1 the capacity of the battery was calculated using a statistically average day in terms of the historic energy usage. The average day was subjected to numerous power outages of various lengths after which the total consumed battery power was calculated.

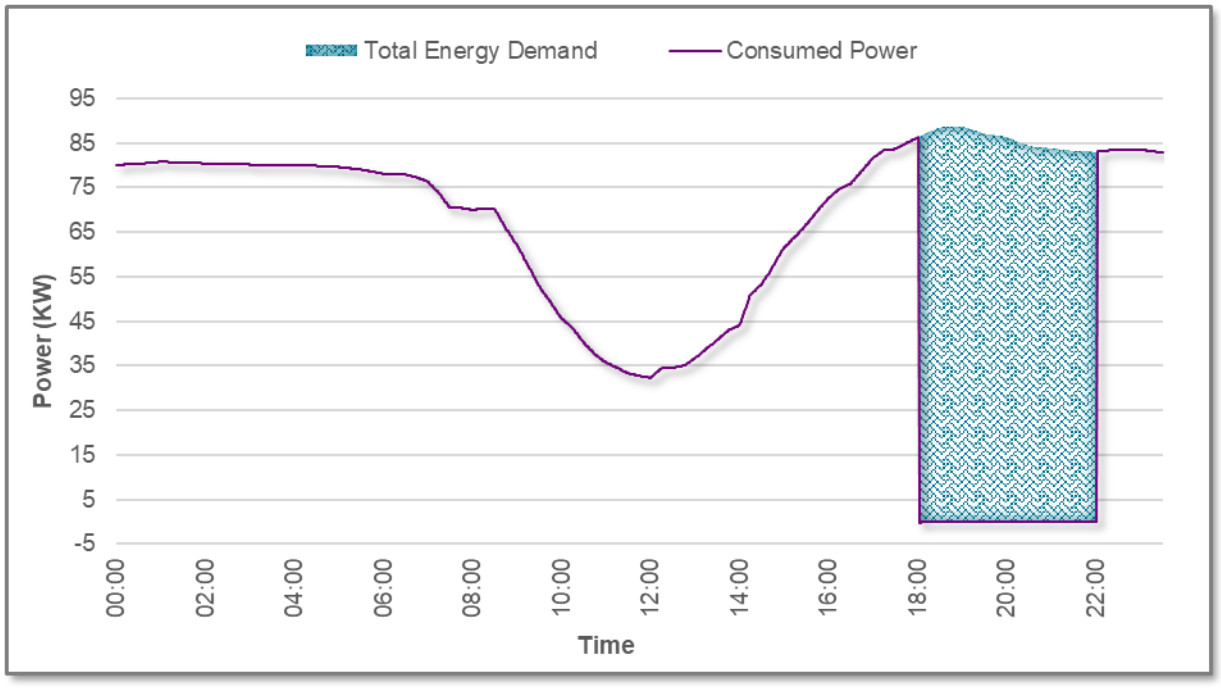

Figure 4-1: Power usage - single outage 4 hours

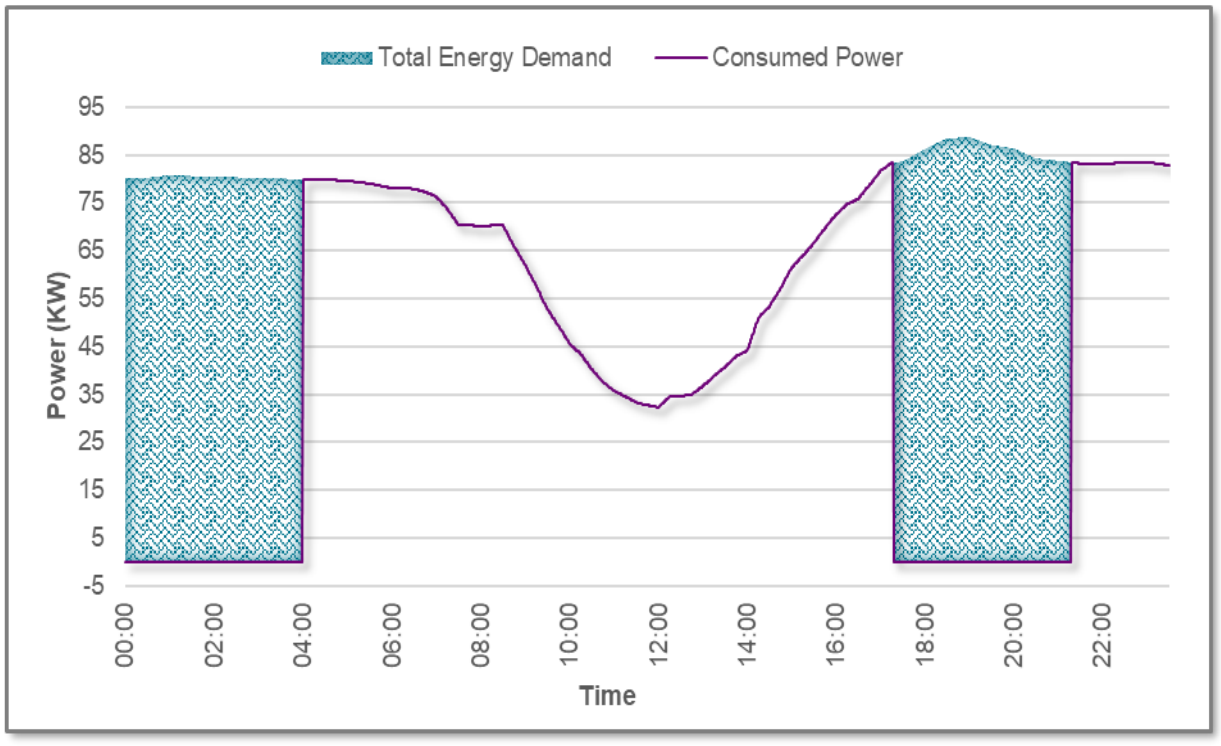

Figure 4-2: Power usage: double outage 4 hours

Figure 4-1 and Figure 4-2 illustrate the building's grid power consumption over an average day, under conditions of single and double 4-hour outages, respectively. The graphs indicate the grid power consumed in kilowatts [kW] during the average day. The building received solar power during this period and was not connected to any energy storage solution. The power consumption in both figures is consistent with the power consumption shown in Figure 3-11. In both Figure 4-1 and Figure 4-2, the building experienced power outages. The shaded areas represent the energy demand during these outage periods ($\frac{d}{dt}P_{demand}$).

In Figure 4-1, the building experienced a power outage between 18:00 and 22:00. During this period, the grid power consumption was 0 kW, as indicated by the line graph. A power demand of approximately 85 kW was maintained during the outage, as shown by the upper limits of the shaded area which follows the normal consumption trend. In Figure 4-2, the building had two outages lasting 4 hours each. These outages occurred from 00:00 to 04:00 and from 17:00 to 21:00. During these periods, the grid power consumption was 0 kW, while the power demand followed the trend of the periods without outages. Peak power consumption was approximately 90 kW on the average day.

Since the battery is responsible for satisfying the building's power demand during power outages, the total energy demand represents the minimum required battery capacity in kilowatt-hours [kWh]. To determine the required battery capacity for various possible power outage scenarios,

several power outages were simulated. Table 4-1 illustrates the energy demand during multiple power outage scenarios. The total energy demand in the table is equivalent to the integral over the shaded area in Figure 4-1 and Figure 4-2. Table 4-1 presents the total energy demand for single and double power outages ranging from 2 hours to 8 hours respectively.

Table 4-1: Total energy demand power outages

Number of Outages	Hours per Outage	Total Energy [kWh]
1	2	88
1	4	175
1	6	260
1	8	345
2	2	174
2	4	343
2	6	502
2	8	666

From Table 4-1, the highest simulated energy demand exceeded 666 kWh. This demand level remains significantly below the energy ratings of industrial-scale VRFBs, which are rated in the megawatt-hour [MWh] range (Noack et al., 2020, Díaz-Ramírez et al., 2021, Apribowo et al., 2023). Insight into the total energy demand plays an important role in specifying the battery requirements.

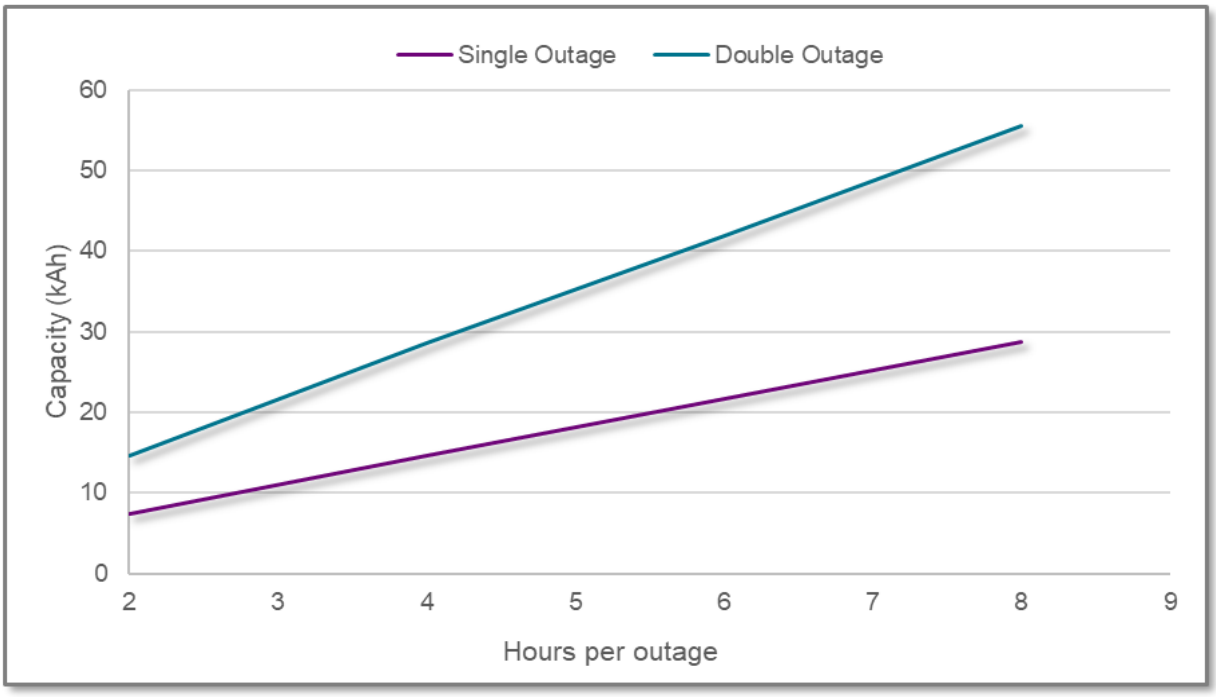

Figure 4-3: Battery capacity requirements due to power outages

Figure 4-3 illustrates the minimum battery capacity [Ah] required to compensate for the various power outage configurations in Table 4-1. The required capacity has a linear relation to the number of outages as well as the duration of the outages. From Figure 4-3, the slope of capacity over outage duration is higher for double outages, but not twice the slope of the single outages. The outages were calculated during peak consumption periods, which means that any additional outages occur outside of these peak times, and therefore incur a smaller energy loss.

4.1.2 Size

The electrode surface area and the volume of electrolyte were used to establish the battery system's size characteristics. Both the electrode surface area and electrolyte volume are dependent on the current density of the electrolyte solution. The battery model was derived from a VRFB with a current density of 100 $mA.cm^{-2}$.

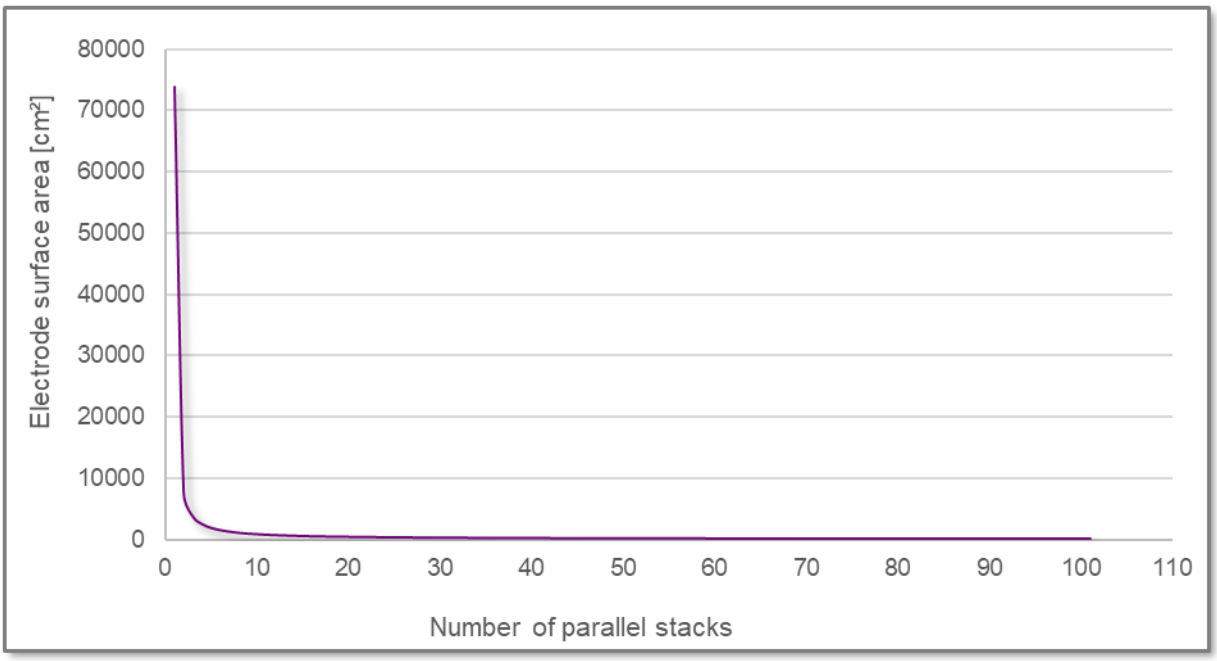

Figure 4-4: Electrode surface area to stack count

Figure 4-4 illustrates the relationship between electrode surface area and the number of parallel cell stacks. The line indicates the required surface area and parallel cell stacks required to provide 90 kW peak power as calculated in Section 4.1.1. The electrode surface area is inversely proportional to the number of parallel stacks.

The size of the battery system is influenced by both the electrode surface area and the number of parallel stacks. It is important to achieve a balance between these two factors. When there are fewer than three parallel stacks, the electrode surface area increases substantially. Conversely, when the surface area is below 820 cm^2 at 10 stacks, a significantly higher number of parallel

stacks is required. From Figure 4-4, an optimal electrode surface area to cell stacks would fall between 3 to 10 stacks for 3600 cm² to 820 cm² per stack.

The model was derived from a VRFB with an electrode surface area of 650cm^2 (Gao *et al.*, 2021), resulting in 13 parallel cell stacks. While this configuration falls outside the optimal range, it does so within reason, requiring only an additional 3 cell stacks. This relationship can be used to adjust the battery system based on size requirements.

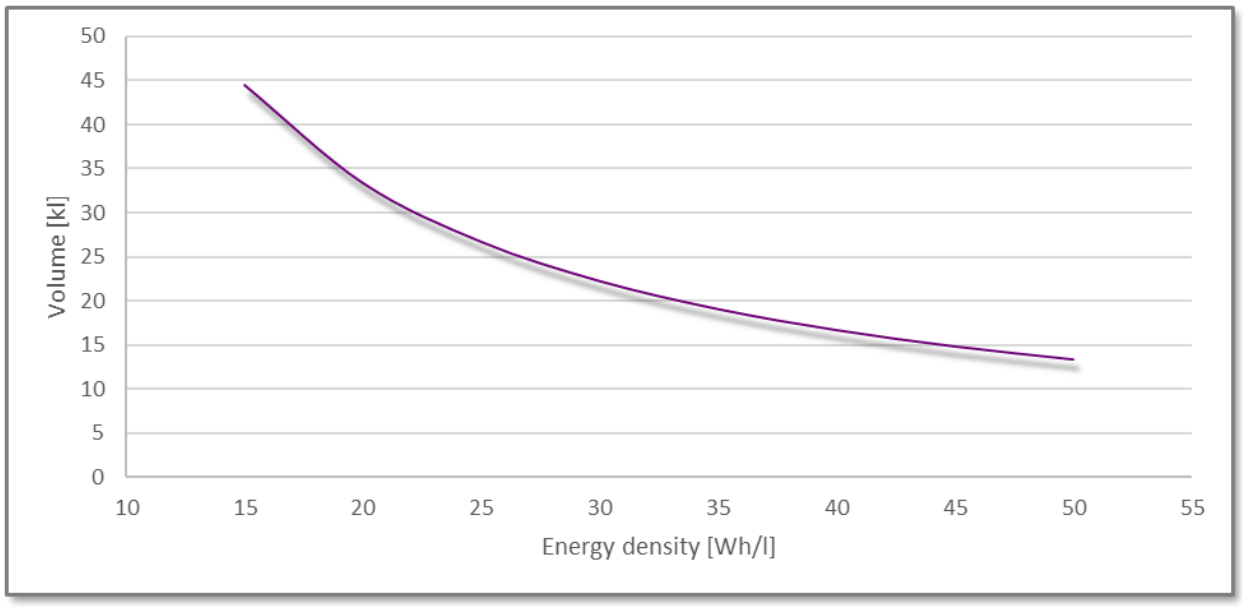

Figure 4-5: Electrolyte volume over energy density of a 666kWh system

Figure 4-5 illustrates the electrolyte volume per tank required as a function of the energy density of the electrolyte. It assumes a required capacity of 666 kWh which is equivalent to a double 8-hour power outage, as seen in Table 4-1. The line depicts the required volume of electrolyte [kl] based on the energy density of the electrolyte [Wh/l].

From Figure 4-5, the relationship between the electrolyte volume and energy density is observed to be non-linear. The slope of the curve levels off as the energy density increases, suggesting that an optimal energy density electrolyte can be determined according to the system requirements. After selecting an electrolyte, Figure 4-5 was used to calculate the electrolyte volume in each tank.

4.2 Factors influencing the performance of a VRFB system

The principal component affecting the energy density and longevity of VRFBs is the electrolyte. It is also the costliest component in the system. Therefore, the key characteristics affecting the

selection of the electrolyte are the cost, energy density and rated number of charge-discharge cycles.

Table 4-2: VRFB performance factors

Performance factor	Recommendation	Operating Temperature [°C]	Concentration [M] Vanadium: Acid(s)	Energy density [Wh/L]
Electrolyte	H_2SO_4	0 – 40	1.5:3	16.0 –18.0
Electrolyte	HCL	0 – 50	2.3:10	35.5
Electrolyte	Mixed H_2SO_4 & HCL	-10 – 50	3:3:6	40.8
Membrane	Nafion			
Negative Electrode	Graphite felt			
Positive Electrode	PAN			

Table 4-2 presents the key materials and configurations used in the VRFB model. The table specifies the chemical composition and ratios for the electrolytes, highlighting the use of a 3:3:6 ratio for the Vanadium(V) oxide, H_2SO_4 and HCL respectively, with a temperature range of -10°C to 50°C. The membrane used in the VRFB is Nafion, chosen for its high proton conductivity and chemical stability. The negative electrode is composed of graphite felt, known for its high surface area and conductivity. The positive electrode is made of graphitised polyacrylamide (PAN), selected for its robustness and compatibility with the acidic environment of the VRFB.

4.3 VRFB model results

An equivalent circuit model (ECM) was configured to model the electrical behaviour of the VRFB under various conditions in Section 3.1. The ECM circuit components were configured so that the model's voltage response approximated the terminal voltage measurements of a VRFB from experimental data.

Figure 4-6 illustrates the ECM voltage response as well as the VRFB terminal voltage measurements taken by Gao *et al*. (2021). Here, both systems were subjected to the same input current and their voltage responses were plotted over time. The input current consisted of either a positive current, representing charging, or a negative current, representing discharging. The voltage response of the literature VRFB is the same as the voltage response used to create the ECM in Section 3.1.1. A test incorporating varying input currents was chosen to evaluate the VRFB under diverse and dynamic conditions.

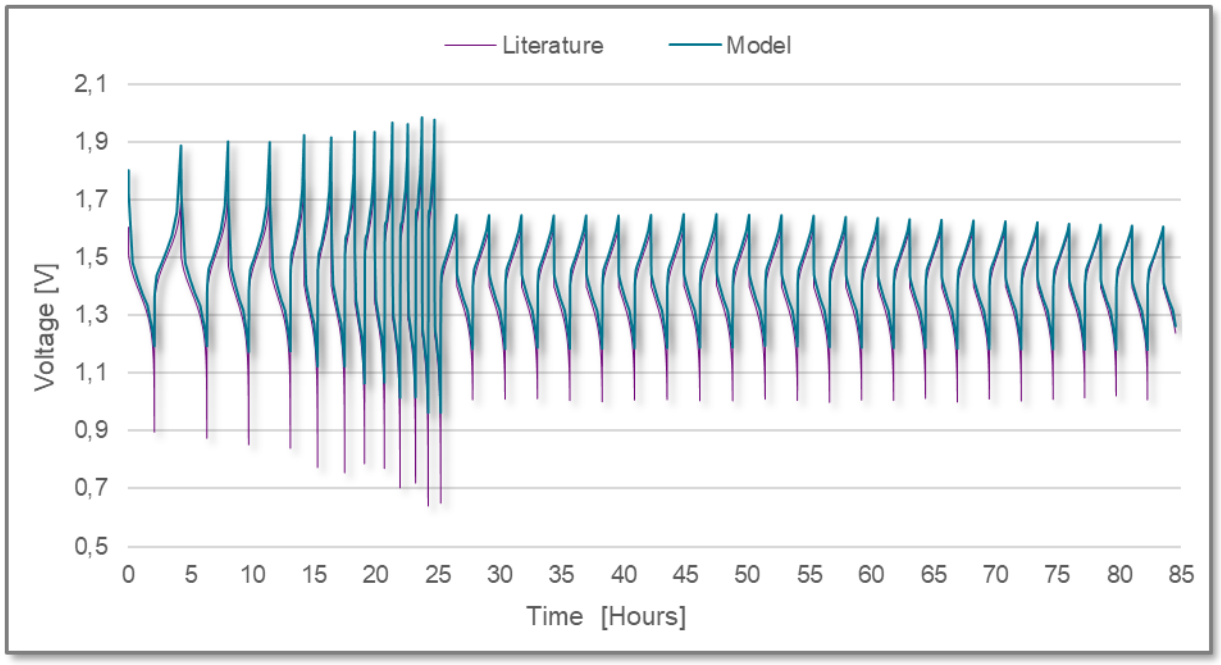

Figure 4-6: ECM voltage response

From Figure 4-6, the voltage response varies in both amplitude and frequency in the first 25 hours. Thereafter, the voltage frequency and amplitude remained stable throughout the duration of the experiment. The amplitude of the voltage response was higher in the first 25 hours than in the rest of the experiment and reached a peak voltage of 2 V at 23 hours. From Figure 4-6 the frequency of the voltage response also increased between 15 and 25 hours as compared to the rest of the experiment.

The voltage response of the ECM is consistent with that of the literature VRFB over the complete 85-hour test period. Notably, during the initial 25 hours, the literature battery exhibited a substantial voltage amplitude, with spikes ranging between 2 V and 0.65 V during transitions between increasing and decreasing phases and *vice versa*. During that period, the ECM did not generate voltage spikes of similar magnitude.

Overall, the ECM managed to produce a similar voltage response as that of the experimental VRFB cited in the literature. The accuracy of the response was maintained for over 30 charge-discharge cycles, indicating that the battery decay and self-discharge was also incorporated in the ECM. The ECM's ability to produce a similar voltage response during changes in input current amplitude and frequency indicates its overall accuracy. The voltage spikes occurred during state transitions from steady state to load conditions and *vice versa.* This is considered the battery's dynamic behaviour and primarily influenced by the RC (Resistor-Capacitor) pairs as seen in Figure 3-4. The similarity between the two models during charging and discharging states,

indicate that the ECM models the over- and underpotential accurately. This also indicates that the internal resistance of the ECM is like that of the literature VRFB.

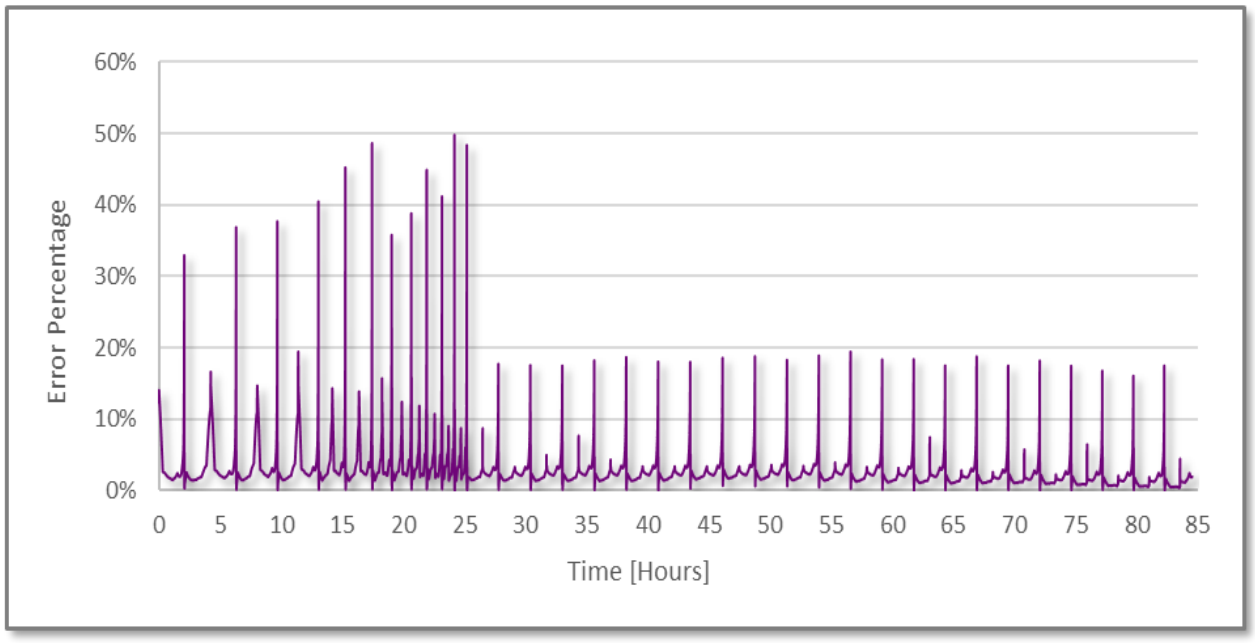

Figure 4-7: ECM Voltage Response – Error Percentage

Figure 4-7 illustrates the error between the model's voltage response and the measured terminal voltage of the experimental data from the literature. The line indicates the difference between the voltage response of the ECM and the literature VRFB shown in Figure 4-6. It shows the difference as a percentage value as well as the time in hours. When viewed in conjunction with Figure 4-6, the error percentage in Figure 4-7 provides more insight into the accuracy of the ECM.

The error spikes illustrated in Figure 4-7 correspond to the voltage spikes presented in Figure 4-6. During these spikes, the error reached a peak of 50% within the initial 25 hours shown in the figure. Beyond the 25-hour mark, the maximum error observed during the voltage spikes was reduced to 20%. The line in Figure 4-7 also demonstrates that the model error remained below 5% during periods without voltage spikes. Furthermore, both spiked and non-spiked model errors were consistent after the 25-hour mark. The model error observed during voltage spikes was notable, especially with high amplitude input current. Although the error during these spikes was considerable, Figure 4-7 demonstrates that the error was limited to the voltage spikes and had minimal impact on the total energy over the 85-hour period.

The model's accuracy was also validated by testing with an independent set of experimental VRFB measurements adapted from Gao *et al*. (2021). Figure 4-8 illustrates the difference between the model's voltage response and the voltage measurements of the independent dataset. The voltage response of the ECM is a result of the input current from the independent dataset.

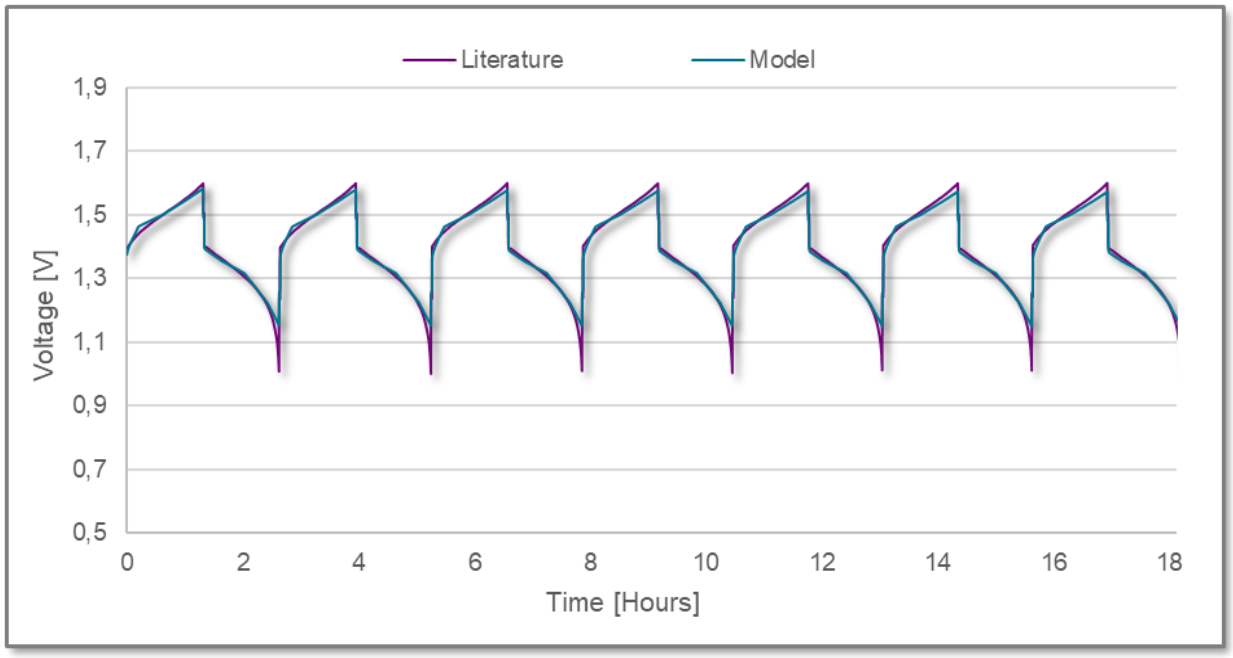

Figure 4-8: ECM Validation - Voltage Response

In Figure 4-8 the voltage response of the ECM closely resembles that of the literature VRFB for the same input signal. The voltage begins at a low point of 1.4 V and increases, in contrast to the initial high voltage of 1.7 V depicted in Figure 4-6. This suggests that the VRFB shown in Figure 4-8 commenced operation at a low state of charge (SoC) and in a charging state. The similarity between the two models for an independent dataset enhances confidence in the ECM's capability to generate a voltage response comparable to that of the VRFB on which it is based.

Figure 4-9 illustrates the model error when subjected to the validation dataset shown in Figure 4-8. The line in Figure 4-9 indicates the difference between voltage response of the ECM and the literature battery as a percentage value. This error percentage is shown for the entire duration of the test depicted in Figure 4-8.

The model error peaked at 15% during state transitions but remained within 2% accuracy of experimental voltage measurements otherwise. This increased error indicates poor model performance in predicting dynamic behaviour. The primary implication of these results is that while the ECM can reliably predict the VRFB's voltage under most conditions, it may require further refinement to better handle the transient behaviours observed during state transitions. This insight is important for applications where precise voltage prediction during dynamic states is necessary, and it highlights areas for potential model improvement.

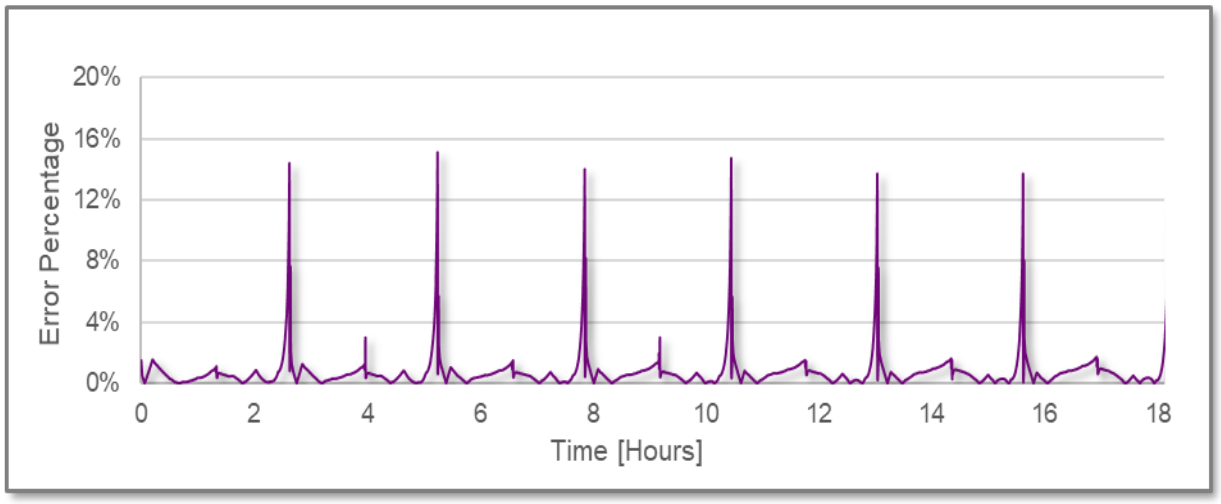

Figure 4-9: ECM Validation - Voltage Response – Error Percentage

The approximated circuit parameters determined during parameter estimation are illustrated in Table 4-3 and Table 4-4. The circuit components were modelled as functions of SoC in Table 4-3. The parasitic, self-discharge resistance R_{SD} was modelled as a constant, as discussed in Section 3.1.5. The open circuit voltage V_0 is inconsistent at SoCs of 0.1 and 1.0 because the experimental battery was primarily operated between 0.1 and 0.9 SoC. The parameter estimation process therefore did not include terminal voltage instances at SoCs outside the operating range.

As observed in Table 4-3, the time constants τ_1 and τ_2 are noticeably higher between 0.4 and 0.6 SoC. This happens because the dataset used to determine the ECM circuit parameters did not account for state transitions within that SoC range. The dataset consisted of a VRFB continuously charging and discharging between nearly full and nearly empty capacity.

Table 4-3: Approximated ECM parameters

SoC	V_0	R_0	R_1	τ_1	R_2	τ_2	R_{SD}
0.1	1.27 V	45.6 mΩ	44.9 mΩ	6 s	4.5 mΩ	154 s	166.6 Ω
0.2	1.23 V	62.2 mΩ	59.9 mΩ	4 s	4.1 mΩ	249 s	166.6 Ω
0.3	1.31 V	63.3 mΩ	61.3 mΩ	21 s	3.2 mΩ	235 s	166.6 Ω
0.4	1.36 V	52.9 mΩ	48.3 mΩ	65 s	1.6 mΩ	4960 s	166.6 Ω
0.5	1.39 V	50.3 mΩ	46.2 mΩ	62 s	1.8 mΩ	1138 s	166.6 Ω
0.6	1.41 V	48.7 mΩ	44.7 mΩ	61 s	1.9 mΩ	2952 s	166.6 Ω
0.7	1.44 V	48.1 mΩ	43.7 mΩ	23 s	1.9 mΩ	10 s	166.6 Ω
0.8	1.46 V	48.4 mΩ	42.9 mΩ	107 s	2.4 mΩ	57 s	166.6 Ω
0.9	1.49 V	49.6 mΩ	45.1 mΩ	37 s	2.2 mΩ	525 s	166.6 Ω
1.0	1.43 V	43.5 mΩ	31.9 mΩ	105 s	2.4 mΩ	933 s	166.6 Ω

The capacity decay parameter is shown in Table 4-4. The remaining cell capacity as well as the percentage loss was modelled as functions of the number of charge-discharge cycles. The ECM's initial capacity was 1.9 Ah at 0 cycles but decreased by 22% to a minimum of 1.47 Ah after 15 cycles. This capacity loss, observed by Gao *et al*. (2021), is higher than observations made in other studies regarding cycle life of VRFBs (Bogdanov et al., 2024). Initial capacity losses of 12% due to heavy pump operation was observed by Bogdanov et al (2024). This reduction in capacity highlights the importance of considering the degradation effects in the design and operational strategies of VRFB systems. It is therefore recommended that the battery system should be designed with a capacity overspecification of at least 22%.

Table 4-4: Approximated ECM parameters continued

Cycles	C [Ah]	Loss (%)
0	1.90	0
5	1.71	9.83
10	1.67	11.9
15	1.47	22.4

The utilisation of a constant self-discharge resistance along with a capacity loss parameter to assess the state of health (SoH) of the VRFB facilitated the modelling of SoH as a function of the number of battery cycles. The inclusion of a self-discharge resistance in addition to the capacity loss was necessary in modelling battery decay over time rather than cycles. This is evident by the accuracy of the voltage response after 15 cycles in Figure 4-6 and Figure 4-7. The accuracy of SoH was measured by comparing the SoH of the ECM with that of the referenced literature VRFB on which the ECM is based.

Figure 4-10 illustrates the comparison between the open circuit voltage of the modelled VRFB and a similar VRFB adapted from (Al-yasiri, 2020). The lines indicate the open circuit voltage (OCV) over SoC. The measurements adapted from Al-yasiri (2020) include all-vanadium VRFBs with current densities of 15 $mA.cm^{-2}$ and 85 $mA.cm^{-2}$ respectively. Both VRFBs were operated at an electrolyte flow rate of 100 $ml.min^{-1}$. The VRFB that the ECM was based on was configured with a current density and flow rate of 100 $mA.cm^{-2}$ and 100 $ml.min^{-1}$ respectively.

From Figure 4-10, the ECM voltage deviates at 0.1 and 1 SoC, aligning with Table 4-3's observations due to the VRFB's operating range of 0.1 to 1. The voltage of the ECM is lower at reduced SoC levels and higher at increased SoC levels when compared to the 15 mA.cm-2 VRFB. Relative to the 85 mA.cm-2, the open circuit voltage state of charge (OCV – SoC) curve follows a similar trend but is approximately 0.2 V lower. The voltage discrepancy between the VRFB at

low and high SoC, along with the operating range limitation of the ECM, suggests that the VRFB on which the ECM is based on provides a voltage response unlike the VRFB measurements adapted from Al-yasiri (2020). The difference in open circuit voltage over SoC is therefore not a product of the ECM itself.

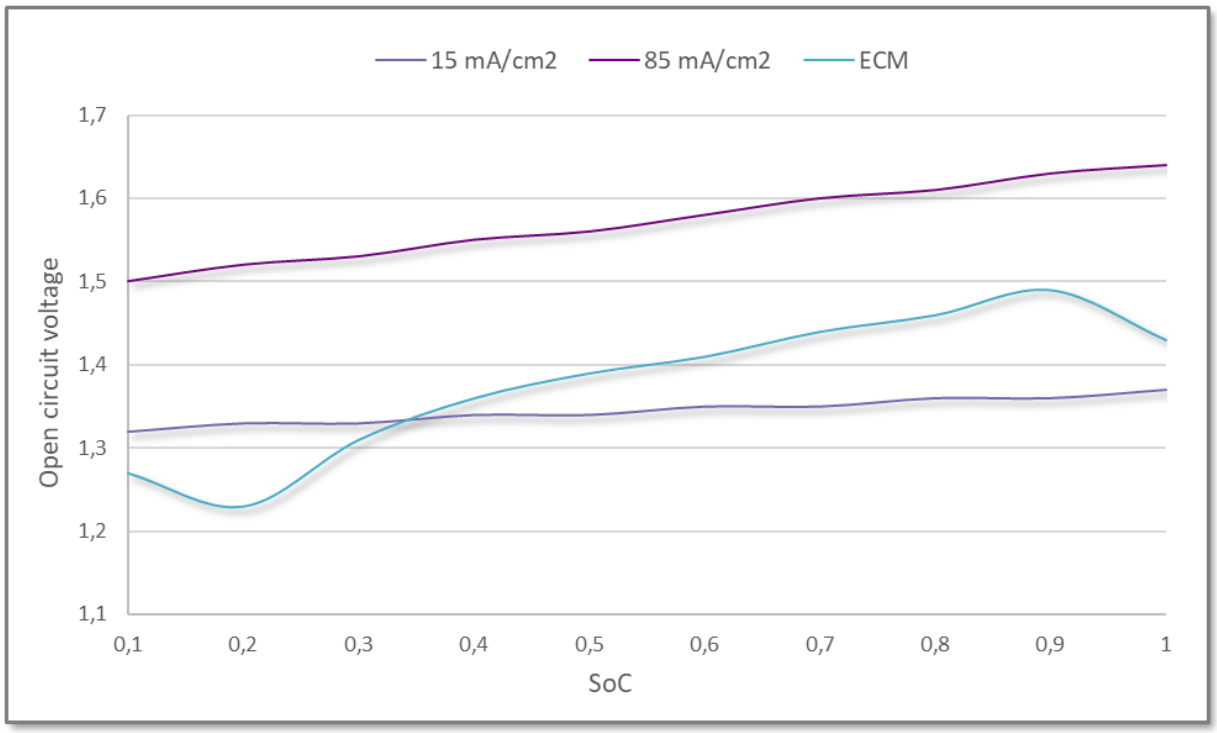

Figure 4-10: OCV-SoC curve Comparison

The model's SoH is compared with the literature VRFB measurements adapted from Gao *et al*. (2021) in Figure 4-11. The literature VRFB SoH measurements depicted in Figure 4-11 correlate with the same experiment as shown in Figure 4-6. The figure includes the model error as a percentage value at 4 intervals along the number of cycles. As observed in Figure 4-11, the similarity in the SoH between the ECM and the literature VRFB is lower during the initial 15 cycles with differences near 6.9%. Additionally, the SoH of the literature VRFB displays greater variability within this period due to an increased number of data points when compared to the ECM. The SoH, based on the capacity loss parameter from Section 3.1.5, remained constant after 15 cycles due to limited voltage measurements. The resolution of the model, set at 5-cycle increments, increased the estimated SoH error during the initial 15 cycles. The literature VRFB's SoH declined after 33 cycles by an additional 4%. This suggests that the experimental dataset consisting of 15 cycles is inadequate for accurately predicting the long-term SoH of the battery.

To simulate power outages and their effects, two possible configurations were selected from the configurations depicted in Table 4-1. The 4 and 8-hour double power outages were selected as the simulation scenarios. The required cell capacity for both scenarios is shown in Table 4-5. The

cell capacity was calculated using a combination of Equation 3 19 and correcting for the capacity loss shown in Table 4-4. Here, the capacity required to meet demand for two 4-hour power outages was measured at 25.37 Ah, while the capacity required to meet demand for two 8-hour power outages was 50.43 Ah.

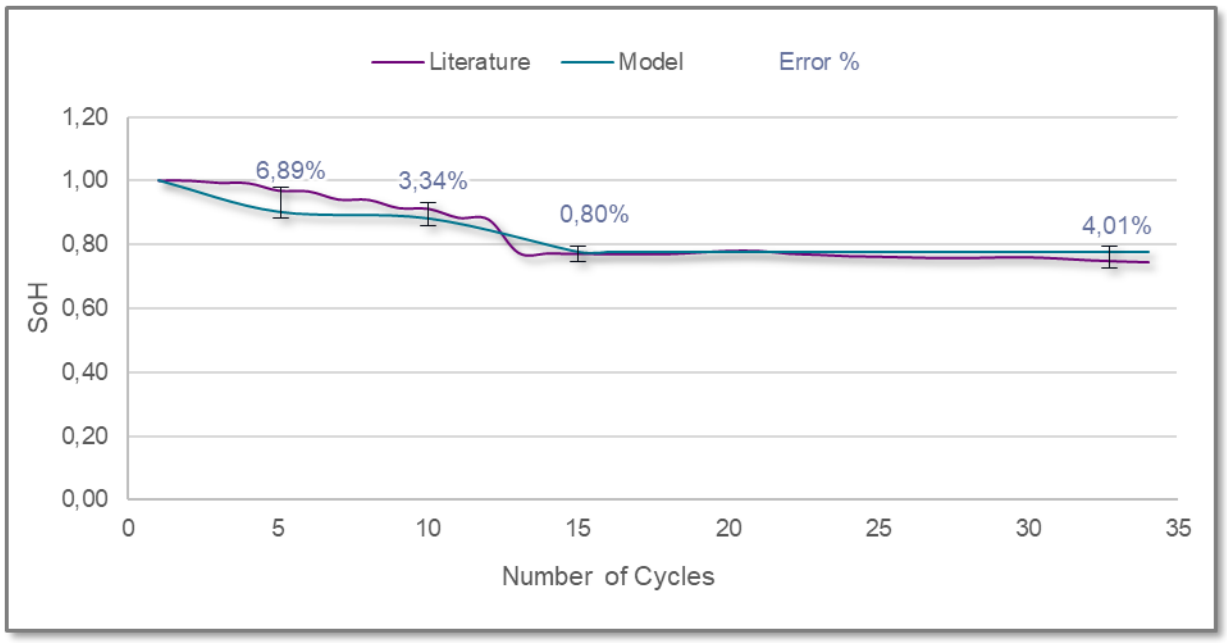

Figure 4-11: ECM SoH

Power outage simulations were created to test the battery response during power outages. The stack topology was configured such that a minimum of 12 V was supplied. This involved a stack configuration of 10 x 13 series and parallel cells respectively. The initial SoC of the cell was set to 0.9 for all simulations, adhering to the 0.1 to 0.9 SoC operating range of the VRFB. The test included scenarios that involve two 4-hour and 8-hour power outages respectively. In the 4-hour outage scenario the VRFB was configured with a capacity of 26 Ah, whereas the VRFB in the 8-hour scenario was configured with a capacity of 51 Ah. The power consumption trend shown in Figure 4-2 was used as the simulation input with two 4-hour outages. The simulation involving two 8-hour outages employed a similar consumption trend as that of the 4-hour scenario. For both scenarios, the solar charging power was connected to the VRFB to test recharging between power outages.

Table 4-5: Outage simulation – Cell capacity

Configuration	Capacity [Ah]
4 Hour	25.37
8 Hour	50.43

Figure 4-12 illustrates the stack current through the building during the power outage scenarios. The lines indicate the cell stack current in ampere over time. The stack current is expected only during power outages, as that is when the battery was operated. A rise in current is shown during solar charging times at 08:00 and 15:30. This occurs due to the overpotential caused by the solar charging power. Current overshoot can be seen during the state transitions to and from power outages. This indicates that the model's dynamic response time is not immediate.

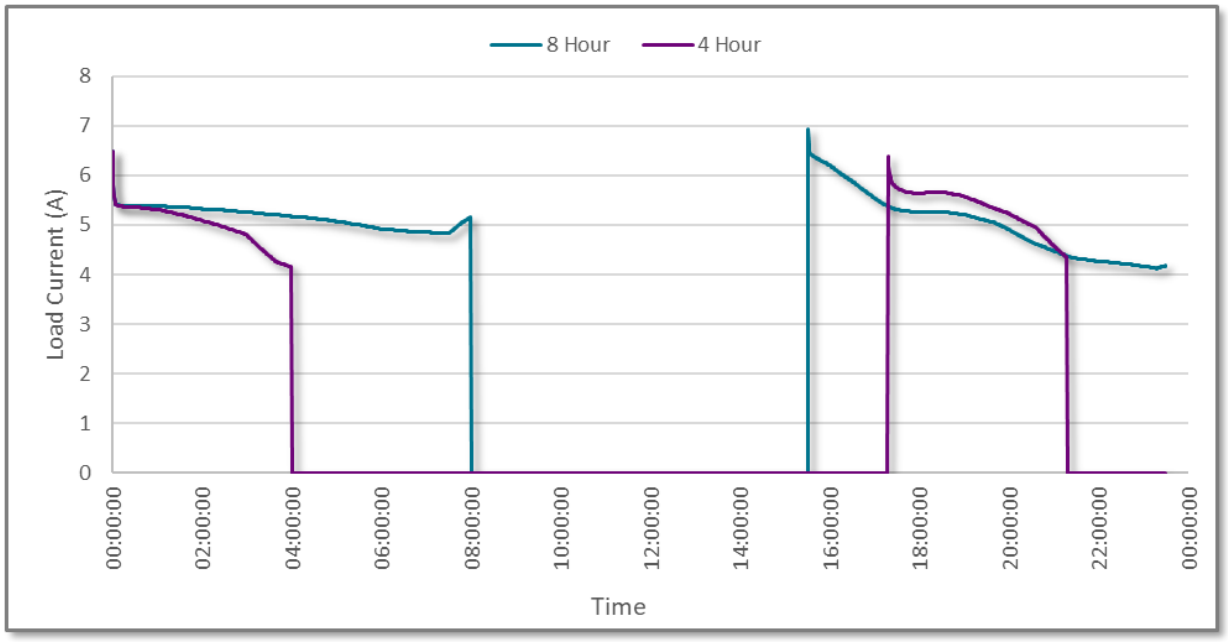

Figure 4-12: Outage simulation – Stack current

The stack voltage during the outage scenarios is shown in Figure 4-13. The lines indicate the voltage over the cell stack over time. The figure indicates the voltage for both the 4- and 8-hour scenarios. These voltage measurements correspond to the current shown in Figure 4-12, but include the effects of the solar charging power. The changes in stack voltage illustrate the battery under- and overpotential when connected to the load. The underpotential increased with the consumption, while the overpotential increased with the solar charging power.

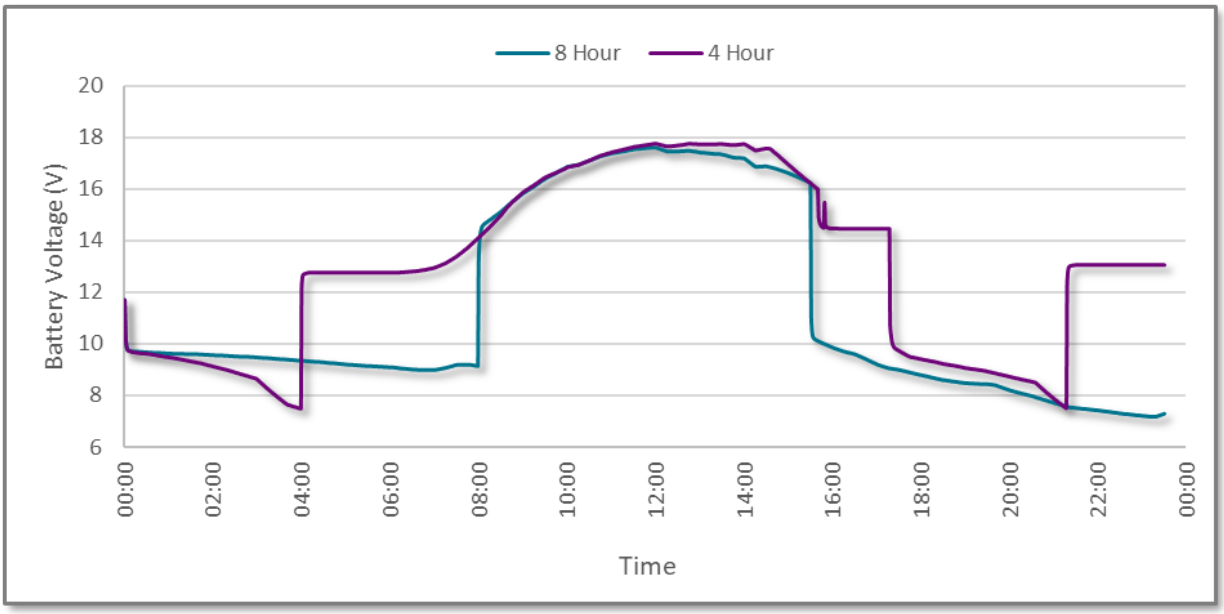

Figure 4-13: Outage simulation – Stack voltage

In Figure 4-13 the stack voltage of the 4-hour outage scenario falls to below 8V at 04:00, while the voltage of the 8-hour scenario remained near 9V throughout the first outage. This indicates a lower SoC in the 4-hour scenario than in the 8-hour scenario. During the second outage starting near 15:30 and 17:00 respectively, the opposite characteristic is shown. Here, the voltage of the 8-hour scenario drops to 7V at the end of the outage period. The same stack voltage was not met for both scenarios because the power demand was not constant throughout the day. In Figure 4-13 the voltage of the 8-hour scenario experienced underpotential at 23:30 while the voltage of the 4-hour scenario was measured at no-load. This explains the difference between the voltage responses at 23:30.

The voltage responses in Figure 4-13 indicate that the cell stack did not maintain a voltage of 12V during the duration of the simulation. This is due to the underpotential caused by connected a load to the stack. A stack configuration involving 10 series cells provided more than 12V at no-load, but each cell provided less than 1.2V at load. If the voltage of the system needs to be regulated, a stack configuration with more series cells is recommended in combination with a voltage regulator. The stack configuration should be based on the voltage of the cells under load. For both scenarios, the VRFB demonstrated the ability to maintain power supply within the set operating range, although notable differences in performance were observed between the 4-hour and 8-hour scenarios.

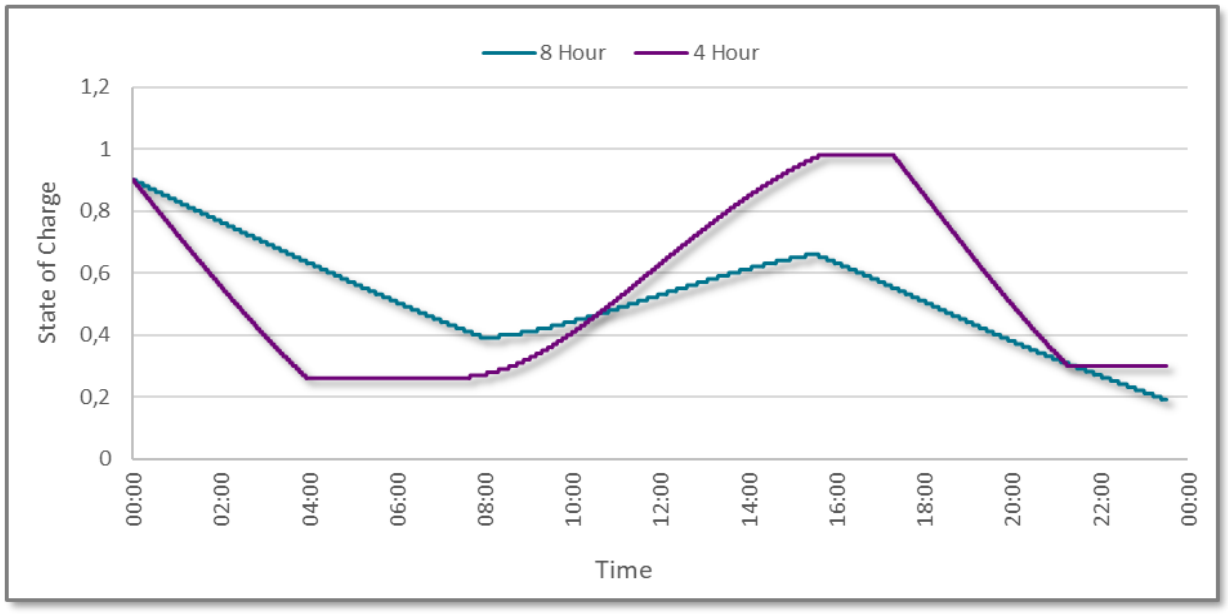

Figure 4-14: Outage simulation – SoC

Figure 4-14 illustrates the stack SoC of the 4-hour and 8-hour power outage scenarios. The SoC measurements in Figure 4-14 correlate with the current and voltage measurements in Figure 4-12 and Figure 4-13 respectively. The lines depict the SoC of the simulated VRFB throughout the duration of the test.

From Figure 4-14 the SoC of the 4-hour scenario reduced from 0.9 to 0.25 in the first power outage from 00:00 to 04:00. The SoC of the 8-hour scenario was only reduced to 0.4 at the end of the 8-hour simulated power outage. This substantiates measurements in Figure 4-13 where the 8-hour scenario measured a higher voltage at the end on the first simulated power outage. The same reverse effect is also shown in Figure 4-14 where the SoC of the 8-hour scenario drops below that of the 4-hour scenario at the end of the second outage.

From Figure 4-14, the operating range of 0.1 to 0.9 has been maintained in both scenarios, indicating that the calculated cell capacity was sufficient in providing power to the simulated load during power outages. However, when considering that the SoC was reduced to below 50% at the end of the first power outage for both scenarios a one-to-one specification of capacity to demand is not recommended. This is due to parasitic effects such as self-discharge and capacity decay, as depicted in Figure 4-11. Therefore, battery overspecification is recommended to ensure reliable performance and longevity of the VRFB system under real-world conditions, where unforeseen variables may impact efficiency

The battery's ability to maintain SoC above 0.1 throughout the 8-hour outage scenario indicates that it is sufficient in providing energy storage for the micro-grid at the North-West University campus. It's scalability in terms of capacity makes it possible for the design to scale in accordance

with any increase in load demand. This is also applicable for the stack configuration discussed in Section 4.1.2. Moreover, the modelling process is modular and can be repeated using the requirements of any micro-grid.

.

CHAPTER 5 CONCLUSION AND RECOMMENDATIONS

5.1 Main findings

Electrolyte selection has the highest influence on battery the cost, size and operating temperature. Although there is no single optimal electrolyte solution, a trade off can be made based on the specific requirements of the battery system and the availability of materials. Among the evaluated electrolyte solutions, a mixed H_2SO_4 and HCL solution has the broadest operating temperature range of -10°C to 50°C and offers the highest energy density. Graphite felt electrodes offer high surface area and electrical conductivity and are versatile in terms of possible modifications. Nafion membranes offer high proton conductivity, chemical stability and thermal stability.

By considering additional energy sources, a 90 kW / 666 kWh VRFB was determined to be sufficient to meet the power demand of a micro-grid on the North-West University campus during two daily 8-hour power outages. The VRFB's energy rating should be increased by at least 50% above the requirements to counteract initial degradation, self-discharge, and parasitic effects. The scalability of VRFB systems allows this configuration to be upgraded in accordance with the requirements of the micro-grid. This scalability allows the system to independently interchange and upgrade its components as needed, increasing its operational and financial feasibility.

An electrical model of a VRFB can be constructed to predict VRFB performance by employing an equivalent circuit model aided by parameter estimation techniques. The electrical model can predict the voltage response of a VRFB under various load conditions, that include charging, discharging and steady state conditions. The model is also able to incorporate battery degradation as a function of the amount of charge/discharge cycles that the system has undergone. In terms of modularity, the equivalent circuit modelling process can be repeated for any VRFB configuration and load requirements.

5.2 Recommendations

General recommendations for future studies include the benchmarking of battery systems with primary focus on their performance as energy storage solutions for commercially sized systems. This should include size, cost, and battery lifecycle benchmarks, such that the feasibility of VRFB systems can be examined in the current market. Furthermore, it is recommended that further studies also incorporate both temperature and electrolyte flow rate as variables to the equivalent circuit model. The omission of electrolyte flow rate and temperature in this study was due to a lack of experimental data studying a combination of these effects on a single electrolyte membrane combination. Simulink™ includes out-of-the-box modelling of the temperature

dimension. Sufficient experimental data including temperature measurements during voltage response can be used to expand the modelling process. Additional study regarding the dynamic behaviour of the battery, especially during load transition phases is recommended. While the ECM is ultimately dependant on VRFB response data, fundamental modelling of the ECM could expose, rather than mask, the operating parameters of VRFB.

Model validation was performed by testing the model against a holdout test set of experimental VRFB measurements from the literature. This links the model validity to the specific VRFB used for generating both training and test set measurements. Conducting physical experiments to validate the model is suggested as it would empirically demonstrate the model's validity. However, this was not feasible for this study due to the long-distance nature of the research and lack of access to on-campus facilities.

BIBLIOGRAPHY

1. ABEROUMAND, S., WOODFIELD, P., SHABANI, B. & DAO, D. V. 2020. Advances in electrode and electrolyte improvements in vanadium redox flow batteries with a focus on the nanofluidic electrolyte approach. *Physics Reports,* 881, 1-49.
2. AGOUNDEDEMBA, M., KIM, C. K. & KIM, H.-G. 2023. Energy Status in Africa: Challenges, Progress and Sustainable Pathways. *Energies,* 16, 7708.
3. AL-YASIRI, M. 2020. A parametric analysis of the output voltage of all-vanadium redox-flow battery system. *IOP Conference Series: Materials Science and Engineering,* 871.
4. APRIBOWO, C. H. B., SARJIYA, HADI, S. P., WIJAYA, F. D. & SETYONEGORO, M. I. B. Optimal Allocation of Vanadium Redox Flow Battery Storage Systems With Integrated Variable Renewable Energy. 2023 15th International Conference on Information Technology and Electrical Engineering (ICITEE), 26-27 Oct. 2023 2023. 375-380.
5. BAUMANN, M., ZIMMERMANN, B., DURA, H., SIMON, B. & WEIL, M. 2013. A comparative probabilistic economic analysis of selected stationary battery systems for grid applications. *2013 International Conference on Clean Electrical Power (ICCEP)*, 87-92.
6. BAYEH, A. W., KABTAMU, D. M., CHANG, Y.-C., WONDIMU, T. H., HUANG, H.-C. & WANG, C.-H. 2021. Carbon and metal-based catalysts for vanadium redox flow batteries: a perspective and review of recent progress. *Sustainable Energy & Fuels,* 5, 1668-1707.
7. BLANC, C. 2009. Modeling of a vanadium redox flow battery electricity storage system.
8. BOGDANOV, S., PARSEGOV, S., IBANEZ, F. M. & PUGACH, M. Modeling of Vanadium Redox Flow Battery Under Different Operating Temperatures. 2024 IEEE 7th International Electrical and Energy Conference (CIEEC), 10-12 May 2024 2024. 5194-5199.
9. BOGDANOV, S., PUGACH, M., PARSEGOV, S., VLASOV, V., IBANEZ, F. M., STEVENSON, K. J. & VOROBEV, P. 2023. Dynamic modeling of vanadium redox flow batteries: Practical approaches, their applications and limitations. *Journal of Energy Storage,* 57, 106191.
10. BUCKLEY, D. N., O'DWYER, C., QUILL, N. & LYNCH, R. P. 2018. Electrochemical energy storage. *Energy Storage Options and Their Environmental Impact,* 46, 115.
11. CAO, L., SKYLLAS-KAZACOS, M., MENICTAS, C. & NOACK, J. 2018. A review of electrolyte additives and impurities in vanadium redox flow batteries. *Journal of Energy Chemistry,* 27, 1269-1291.

12. CAPELLÁN-PÉREZ, I., MEDIAVILLA, M., DE CASTRO, C., CARPINTERO, Ó. & MIGUEL, L. J. 2014. Fossil fuel depletion and socio-economic scenarios: An integrated approach. *Energy,* 77, 641-666.

13. CHALLAPURAM, Y. R., QUINTERO, G. M., BAYNE, S. B., SUBBURAJ, A. S. & HARRAL, M. A. 2019. Electrical Equivalent Model of Vanadium Redox Flow Battery. *2019 IEEE Green Technologies Conference(GreenTech)*, 1-4.

14. CHOI, C., KIM, S., KIM, R., CHOI, Y., KIM, S., JUNG, H.-Y., YANG, J. H. & KIM, H.-T. 2017. A review of vanadium electrolytes for vanadium redox flow batteries. *Renewable and Sustainable Energy Reviews,* 69, 263-274.

15. CHUN, H., KIM, J., YU, J. & HAN, S. 2020. Real-Time Parameter Estimation of an Electrochemical Lithium-Ion Battery Model Using a Long Short-Term Memory Network. *IEEE Access,* 8, 81789-81799.

16. CIEZ, R. E. & STEINGART, D. A. 2020. Asymptotic Cost Analysis of Intercalation Lithium-Ion Systems for Multi-hour Duration Energy Storage. *Joule,* 4, 597-614.

17. DELGADO, N. M., MONTEIRO, R., CRUZ, J., BENTIEN, A. & MENDES, A. 2022. Shunt currents in vanadium redox flow batteries – a parametric and optimization study. *Electrochimica Acta,* 403, 139667.

18. DÍAZ-RAMÍREZ, M. C., BLECUA-DE-PEDRO, M., ARNAL, Á. J. & POST, J. W. 2021. Acid/base flow battery environmental and economic performance based on its potential service to renewables support. *Journal of Cleaner Production*.

19. DU, J., LIU, J., LIU, S.-Y., WANG, L. & CHOU, K.-C. 2023. Research progress of vanadium battery with mixed acid system: A review. *Journal of Energy Storage*.

20. FERNÁNDEZ-MARCHANTE, C. M., MILLÁN, M., MEDINA-SANTOS, J. I. & LOBATO, J. 2020. Environmental and Preliminary Cost Assessments of Redox Flow Batteries for Renewable Energy Storage. *Energy technology,* 8, 1900914.

21. FOGELQUIST, J., LAI, Q. & LIN, X. 2023. On the Error of Li-ion Battery Parameter Estimation Subject to System Uncertainties. *Journal of The Electrochemical Society*.

22. FORNARO, P., PULESTON, T., PULESTON, P. F., SERRA-PRAT, M., COSTA-CASTELLÓ, R. & BATTAIOTTO, P. E. 2022. Redox flow battery time-varying parameter estimation based on high-order sliding mode differentiators. *International Journal of Energy Research,* 46.

23. GAO, P., KIM, S., THOMSEN, E. C., CHEN, Y., FU, Y., BAO, J., XU, Z. & WANG, W. 2021. An experimental database of cell performance for vanadium redox flow battery.

24. GUO, Y., HUANG, J. & FENG, J. 2022. Research progress in preparation of electrolyte for all-vanadium redox flow battery. *Journal of Industrial and Engineering Chemistry*.

25. GVOZDIK, N., KURILOVICH, A. & STEVENSON, K. J. 2022. Identification of Overpotentials in Vanadium Redox Flow Battery with Reference Electrodes and Determination of Apparent Electrochemical Rate Constants. *ECS Meeting Abstracts,* 2022, 2033-2033.

26. HALL, D. M., GRENIER, J., DUFFY, T. S. & LVOV, S. N. 2020. The Energy Storage Density of Redox Flow Battery Chemistries: A Thermodynamic Analysis. *Journal of The Electrochemical Society,* 167, 110536.

27. HE, Z., LV, Y., ZHANG, T., ZHU, Y., DAI, L., YAO, S., ZHU, W. & WANG, L. 2022. Electrode materials for vanadium redox flow batteries: Intrinsic treatment and introducing catalyst. *Chemical Engineering Journal,* 427, 131680.

28. HÖÖK, M. & TANG, X. 2013. Depletion of fossil fuels and anthropogenic climate change—A review. *Energy Policy,* 52, 797-809.

29. HUANG, Z., MU, A., WU, L.-Y. & WANG, H. 2021. Vanadium redox flow batteries: Flow field design and flow rate optimization. *Journal of Energy Storage*.

30. HUANG, Z., MU, A., WU, L. & WANG, H. 2022. Vanadium redox flow batteries: Flow field design and flow rate optimization. *Journal of Energy Storage,* 45, 103526.

31. HURIA, T., JACKEY, R., GAZZARRI, J., SAGINAW, M. & SANGHVI, P. 2013. *Battery Model Parameter Estimation Using a Layered Technique: An Example Using a Lithium Iron Phosphate Cell*.

32. IWAKIRI, I., ANTUNES, T., ALMEIDA, H., SOUSA, J. P., FIGUEIRA, R. B. & MENDES, A. 2021. Redox Flow Batteries: Materials, Design and Prospects. *Energies,* 14, 5643.

33. JINYEON, H., BO-MI, K., JOONHEE, M., ASAD, M. & HA, H. 2018. A highly efficient and stable organic additive for the positive electr olyte in vanadium redox flow batteries: taurine biomolecules containin g –NH2 and –SO3H functional groups.

34. KESHAN, H., THORNBURG, J. D. & USTUN, T. S. Comparison of lead-acid and lithium ion batteries for stationary storage in off-grid energy systems. 2016.

35. KIM, K. J., PARK, M. S., KIM, Y. J., KIM, J. H., DOU, S. X. & SKYLLAS-KAZACOS, M. 2015. A technology review of electrodes and reaction mechanisms in vanadium redox flow batteries. *Journal of Materials Chemistry A,* 3, 16913-16933.

36. KIM, S., VIJAYAKUMAR, M., WANG, W., ZHANG, J., CHEN, B., NIE, Z., CHEN, F., HU, J., LI, L. & YANG, Z. 2011. Chloride supporting electrolytes for all-vanadium redox flow batteries. *Phys Chem Chem Phys,* 13, 18186-93.

37. KLEINSTEINBERG, B., KLICK, S. & SAUER, D. U. 2020. Empirical approach to determine open-circuit voltage of a vanadium-redox-flow battery for models, based on published data for anion-exchange and cation-exchange membranes and temperature dependency. *Journal of Energy Storage,* 28, 101109.

38. KNEHR, K. W., AGAR, E., DENNISON, C. R., KALIDINDI, A. R. & KUMBUR, E. C. 2012. A Transient Vanadium Flow Battery Model Incorporating Vanadium Crossover and Water Transport through the Membrane. *Journal of The Electrochemical Society,* 159, A1446-A1459.

39. KROWNE, C. M. 2023. Nernst Equations and Concentration Chemical Reaction Overpotentials for VRFB Operation. *Journal of The Electrochemical Society*.

40. LEUNG, P., SHAH, A., SANZ RUBIO, L., FLOX, C., MORANTE, JR., XU, Q., MOHAMED, M. R., PONCE DE LEÓN, C. & WALSH, F. 2017. Recent developments in organic redox flow batteries: A critical review. *Journal of Power Sources,* 360, 243-283.

41. LI, B., GU, M., NIE, Z., SHAO, Y., LUO, Q., WEI, X., LI, X., XIAO, J., WANG, C. & SPRENKLE, V. 2013. Bismuth nanoparticle decorating graphite felt as a high-performance electrode for an all-vanadium redox flow battery. *Nano letters,* 13, 1330-1335.

42. LI, J., MAZZOLA, M. S., GAFFORD, J. & YOUNAN, N. H. 2012. A new parameter estimation algorithm for an electrical analogue battery model. *2012 Twenty-Seventh Annual IEEE Applied Power Electronics Conference and Exposition (APEC)*, 427-433.

43. LI, L., KIM, S., WANG, W., VIJAYAKUMAR, M., NIE, Z., CHEN, B., ZHANG, J., XIA, G., HU, J. & GRAFF, G. 2011a. A stable vanadium redox-flow battery with high energy density for large-scale energy storage. *Advanced Energy Materials,* 1, 394-400.

44. LI, W., LIU, J. & YAN, C. 2011b. Multi-walled carbon nanotubes used as an electrode reaction catalyst for VO2+/VO2+ for a vanadium redox flow battery. *Carbon,* 49, 3463-3470.

45. LI, X., ZHANG, H., MAI, Z., ZHANG, H. & VANKELECOM, I. 2011c. Ion exchange membranes for vanadium redox flow battery (VRB) applications. *Energy & Environmental Science,* 4, 1147-1160.

46. LIMING, C., TAO, L., YI-MIN, Z., HONG, L., MUQING, D. & DONG, P. 2022. Mitigating Capacity Decay by Adding Carbohydrate in the Negative Elect rolyte of Vanadium Redox Flow Battery. *Energies*.

47. LOURENSSEN, K., WILLIAMS, J., AHMADPOUR, F., CLEMMER, R. & TASNIM, S. 2019. Vanadium redox flow batteries: A comprehensive review. *Journal of Energy Storage,* 25, 100844.

48. LUO, Q., LI, L., WANG, W., NIE, Z., WEI, X., LI, B., CHEN, B., YANG, Z. G. & SPRENKLE, V. L. 2013. Capacity decay and remediation of nafion-based all-vanadium redox flow batteries. *ChemSusChem,* 6 2, 268-74.

49. MARSHALL, P. F., VICHANPOL, B., RAKWICHIAN, W., WONGPANYO, W., SITTISUN, P. & THANARAK, P. Comparison of Energy Storage Technologies for a Notional, Isolated Community Microgrid. 2020.

50. MATHWORKS 2024. Battery (Table-Based).

51. MAY, G. J., DAVIDSON, A. & MONAHOV, B. 2018. Lead batteries for utility energy storage: A review. *Journal of Energy Storage,* 15, 145-157.

52. MIGNARD, D. 2014. Estimating the capital costs of energy storage technologies for levelling the output of renewable energy sources. *International Journal of Environmental Studies,* 71, 796 - 803.

53. MOORE, M. A., COUNCE, R. M., WATSON, J. S. & ZAWODZINSKI, T. A. A Comparison of the Capital Costs of a Vanadium Redox-Flow Battery and a Regenerative Hydrogen-Vanadium Fuel Cell. 2015.

54. NGUYEN, T. D., WHITEHEAD, A., WAI, N., SCHERER, G. G., SIMONOV, A. N., XU, Z. J. & MACFARLANE, D. R. 2024. Advanced Electrolyte Formula for Robust Operation of Vanadium Redox Fl ow Batteries at Elevated Temperatures. *Small,* 20.

55. NOACK, J., ROZNYATOVSKAYA, N. V., MENICTAS, C., SKYLLAS-KAZACOS, M. & TÜBKE, J. 2020. Vanadium/Oxygen Systems for Energy Storage. *ECS Meeting Abstracts,* MA2021-01, 26-26.

56. ORIJI, G., KATAYAMA, Y. & MIURA, T. 2004. Investigation on V(IV)/V(V) species in a vanadium redox flow battery. *Electrochimica Acta,* 49, 3091-3095.

57. OZGOLI, H. A., ELYASI, S. & MOLLAZADEH, M. 2015. Hydrodynamic and electrochemical modeling of vanadium redox flow battery. *Mechanics & Industry,* 16, 201.

58. PARK, D.-J., JEON, K.-S., RYU, C.-H. & HWANG, G.-J. 2017. Performance of the all-vanadium redox flow battery stack. *Journal of Industrial and Engineering Chemistry,* 45, 387-390.

59. PARTHASARATHY, C., HAFEZI, H. & LAAKSONEN, H. 2020. Lithium-ion BESS Integration for Smart Grid Applications - ECM Modelling Approach. *2020 IEEE Power & Energy Society Innovative Smart Grid Technologies Conference (ISGT)*, 1-5.

60. PATHAK, A., SHARMA, A. K. & GUPTA, A. K. 2022. Systematic Lumped Modeling of all-Vanadium Redox Flow Batteries. *Journal of The Electrochemical Society*.

61. PHIL-JACQUES, A., TAŞ, M. & GULSAH, E. 2022. Numerical Investigation of Supporting Electrolyte Using in a Vanadium Redox Flow Battery. *ECS Meeting Abstracts*.

62. POULLIKKAS, A. 2013. A comparative overview of large-scale battery systems for electricity storage. *Renewable and Sustainable Energy Reviews,* 27, 778-788.

63. PRAPHULLA, P., RAO, P. & JAYANTI, S. 2022. *Temperature-sensitive Electrochemical Model of Vanadium Redox Flow Battery Cell*.

64. PUGACH, M., KONDRATENKO, M., BRIOLA, S. & BISCHI, A. 2018. Zero dimensional dynamic model of vanadium redox flow battery cell incorporating all modes of vanadium ions crossover. *Applied Energy,* 226, 560-569.

65. PULESTON, T., CLEMENTE, A., COSTA-CASTELLÓ, R. & SERRA, M. 2022. Modelling and Estimation of Vanadium Redox Flow Batteries: A Review. *Batteries,* 8, 121.

66. R. THAKKAR, R. 2021. Electrical Equivalent Circuit Models of Lithium-ion Battery. *Energy Storage Devices [Working Title]*.

67. RA, N. & BHATTACHARJEE, A. 2021. An Extensive Study and Analysis of System Modeling and Interfacing of Vanadium Redox Flow Battery. *Energy Technology,* 9, 2000708.

68. RAO, P. & JAYANTI, S. 2023. Physics-Based Electrochemical Model of Vanadium Redox Flow Battery for Low-Temperature Applications. *Batteries*.

69. REN, J., LI, Y., WANG, Z., SUN, J., YUE, Q., FAN, X. & ZHAO, T. 2023. Thermal issues of vanadium redox flow batteries. *International Journal of Heat and Mass Transfer*.

70. ROBERTS, D. & BROWN, S. F. 2022. The economics of firm solar power from Li-ion and vanadium flow batteries in California. *MRS Energy & Sustainability,* 9, 129-141.

71. ROTAS, R., ILIADIS, P., NIKOLOPOULOS, N., RAKOPOULOS, D. & TOMBOULIDES, A. 2024. Dynamic Battery Modeling for Electric Vehicle Applications. *Batteries,* 10, 188.

72. ROZNYATOVSKAYA, N., NOACK, J., HEIKO, M., FÜHL, M., FISCHER, P., PINKWART, K., TÜBKE, J. & SKYLLAS-KAZACOS, M. 2019. Vanadium Electrolyte for All-Vanadium Redox-Flow Batteries: The Effect of the Counter Ion. *Batteries*.

73. RYCHCIK, M. & SKYLLAS-KAZACOS, M. 1988. Characteristics of a new all-vanadium redox flow battery. *Journal of Power Sources,* 22, 59-67.

74. SANGWON, K. 2019. Vanadium Redox Flow Batteries: Electrochemical Engineering. *In:* DEMIRKAN, M. T. & ADEL, A. (eds.) *Energy Storage Devices.* Rijeka: IntechOpen.

75. SEEPANA, M. M., SAMUDRALA, S., SURESH, P. V. & VOORADI, R. 2018. Unit Cell Modelling and Simulation of All Vanadium Redox Flow Battery. *Chemical Product and Process Modeling,* 13.

76. SHIGEMATSU, T. 2011. Redox flow battery for energy storage. *SEI technical review,* 73, 13.

77. SINSEL, S. R., RIEMKE, R. L. & HOFFMANN, V. H. 2020. Challenges and solution technologies for the integration of variable renewable energy sources—a review. *Renewable Energy,* 145, 2271-2285.

78. SKYLLAS-KAZACOS, M. & MCCANN, J. F. 2015. Chapter 10 - Vanadium redox flow batteries (VRBs) for medium- and large-scale energy storage. *In:* MENICTAS, C., SKYLLAS-KAZACOS, M. & LIM, T. M. (eds.) *Advances in Batteries for Medium and Large-Scale Energy Storage.* Woodhead Publishing.

79. THELIANDER, O., KERSTEN, A., KUDER, M., GRUNDITZ, E. & THIRINGER, T. 2019. *LiFeP0 4 Battery Modeling and Drive Cycle Loss Evaluation in Cascaded H-Bridge Inverters for Vehicles*.

80. TIAN, W., DU, H., WANG, J., WEIGAND, J. J., QI, J., WANG, S. & LI, L. 2023. A Review of Electrolyte Additives in Vanadium Redox Flow Batteries. *Materials* [Online], 16.

81. TOJA, F., PERLINI, L., FACCHI, D., CASALEGNO, A. & ZAGO, M. 2023. Mitigation of Discharged Capacity Decay and Volume Variation in Vanadi um Redox Flow Batteries By Modifying Electrolytes Composition. *ECS Meeting Abstracts*.

82. VASUDEVARAO, P. & RAMANUJAM, K. 2017. On In–situ Redox Balancing of Vanadium Redox Flow Battery Using D-Fruc tose as Negative Electrolyte Additive.

83. WANG, G., JINWEI, C., YADONG, X., BICHEN, Y., XUEQIN, W., XUEJING, Z., YU, Z., XIAOJIANG, L. & RUILIN, W. 2014. Several ionic organic compounds as positive electrolyte additives for a vanadium redox flow battery.

84. WANG, Y., MU, A., WANG, W., YANG, B. & WANG, J. 2024. A Review of Capacity Decay Studies of All-vanadium Redox Flow Batteries: Mechanism and State Estimation. *ChemSusChem*, e202301787.

85. WEBER, S., PETERS, J. F., BAUMANN, M. & WEIL, M. 2018. Life Cycle Assessment of a Vanadium Redox Flow Battery. *Environmental Science & Technology,* 52, 10864-10873.

86. WEI, X., WANG, G., LI, F., ZHANG, J., CHEN, J. & WANG, R. 2022. High Performance Positive Electrolyte with Potassium Diformate (KDF) A dditive for Vanadium Redox Flow Batteries. *International Journal of Electrochemical Science,* 17, 220126.

87. WENXIN, T., HAO, D., JIANZHANG, W., WEIGAND, J., JIANZHONG, Q., SHAONA, W. & LANJIE, L. 2023. A Review of Electrolyte Additives in Vanadium Redox Flow Batteries. *Materials*.

88. WOLFRAM, P. & LUTSEY, N. Electric Vehicles: Literature review of technology costs and carbon emissions. 2016.

89. XIONG, B., YANG, Y., TANG, J., LI, Y., WEI, Z., SU, Y. & ZHANG, Q. 2019. An Enhanced Equivalent Circuit Model of Vanadium Redox Flow Battery Energy Storage Systems Considering Thermal Effects. *IEEE Access,* 7.

90. XIONGWEI, W., JUN, L., XIAOJUAN, X., ZHANG, J., JUNPING, H. & YUPING, W. 2014. Electrolytes for vanadium redox flow batteries.

91. XU, Z., XIAO, W., ZHANG, K., ZHANG, D., WEI, H., ZHANG, X., ZHANG, Z., PU, N., LIU, J. & YAN, C.-W. 2020. An advanced integrated electrode with micron- and nano-scale structures for vanadium redox flow battery. *Journal of Power Sources,* 450, 227686.

92. YANG, W. W., HE, Y. L. & LI, Y. S. 2015. Performance Modeling of a Vanadium Redox Flow Battery during Discharging. *Electrochimica Acta,* 155, 279-287.

93. YANG, Y., ZHANG, Y.-M., TANG, L., LIU, T., PENG, S. & YANG, X. 2020. Improved energy density and temperature range of vanadium redox flow battery by controlling the state of charge of positive electrolyte. *Journal of Power Sources,* 450, 227675.

94. YEON, S.-H., SO, J.-Y., YUN, J.-H., PARK, S.-K., SHIN, K. H., JIN, C.-S. & LEE, Y. J. Effect of Phosphate Additive for Thermal Stability in a Vanadium Redox Flow Battery. 2017.

95. YESILYURT, M. S. & YAVASOGLU, H. A. 2023. An All-Vanadium Redox Flow Battery: A Comprehensive Equivalent Circuit Model. *Energies,* 16, 2040.

96. YILMAZ, E. N. 2015. BATTERIES FOR LARGE SCALE STATIONARY ELECTRICAL ENERGY STORAGE.

97. YIN, Y., WANG, J., JIANG, S., YANG, X., ZHANG, X., CAO, Y., CAO, L. & WU, H. 2015. Novel composite membranes based on sulfonated poly(ether ether ketone) and adenosine triphosphate for enhanced proton conduction. *RSC Advances,* 5, 75434-75441.

98. YOSHIO, M., BRODD, R. J. & KOZAWA, A. 2009. *Lithium-ion batteries*, Springer.

99. ZHANG, Y., ZHAO, J., WANG, P., SKYLLAS-KAZACOS, M., XIONG, B. & BADRINARAYANAN, R. 2015. A comprehensive equivalent circuit model of all-vanadium redox flow battery for power system analysis. *Journal of Power Sources,* 290, 14-24.

100. ZIHAN, Y., XIONGJIE, J., YUHAO, C., RUIHANG, S., QIANG, Z., TIANSHOU, Z. & HAORAN, J. 2024. Electrolyte engineering for efficient and stable vanadium redox flow b atteries. *Energy Storage Materials*.

APPENDIX A – MATLAB EXTACT

```
classdef clsSimulation
    properties
        Time
        power
        powerFromBattery
        isOutage
        outageIndices
        consumedPower
        chargingPower
        auxPower
        size
        timeDuration
    end

    methods
        function obj = clsSimulation(ttConsumed, ttCharged, outageMinuteStart, outageMinuteEnd)

            obj.size = length(ttConsumed.power);
            if(length(ttCharged.power) < 1)
                ttCharged = ttConsumed;
                ttCharged.power = ttCharged.power .* 0;
            end

            ttConsumedSeconds = retime(ttConsumed,"secondly","linear");
            ttChargedSeconds = retime(ttCharged,"secondly","linear");

            synced = synchronize(ttConsumedSeconds, ttChargedSeconds, "intersection");

            obj.timeDuration = synced.Time;
            obj.Time = seconds(ttConsumedSeconds.Time);
```

```
    obj.consumedPower = synced{:,1};
    obj.chargingPower = synced{:,2};

    obj = SetOutage(obj, outageMinuteStart, outageMinuteEnd);
    obj = SetPower(obj);
end

function totalEnergy = TotalEnergy(obj, startMinutes, endMinutes)
    windowData = obj.power(obj.Time >= 60*startMinutes & obj.Time <= 60*endMinutes, :);
    totalEnergy = sum(windowData) / 3600; %seconds to hours
end

function totalEnergy = TotalBatteryEnergy(obj, startMinutes, endMinutes)
    windowData = obj.powerFromBattery(obj.Time >= 60*startMinutes & obj.Time <= 60*endMinutes, :);
    totalEnergy = sum(windowData) / 3600; %seconds to hours
end

function totalEnergy = TotalOutageEnergy(obj)
    windowData = obj.consumedPower .* obj.isOutage;
    totalEnergy = sum(windowData) / 3600; %seconds to hours
end

function obj = SetPower(obj)
    obj.power = (obj.consumedPower .* (~obj.isOutage)) - obj.chargingPower;
    obj.powerFromBattery = (obj.consumedPower .* (obj.isOutage)) - obj.chargingPower;
end

function obj = SetOutage(obj, outageMinuteStart, outageMinuteEnd)
    obj.isOutage = (obj.Time >= outageMinuteStart*60) & (obj.Time <= outageMinuteEnd*60);
    obj.outageIndices = (obj.Time == outageMinuteStart*60) | (obj.Time == outageMinuteEnd*60);
    if(max(obj.isOutage) == 0)
        obj.outageIndices = obj.outageIndices .* 0;
```

```
        end

    end


    function obj = AddOutage(obj, outageMinuteStart, outageMinuteEnd)

        obj.isOutage = obj.isOutage | ((obj.Time >= outageMinuteStart*60) & (obj.Time <= outageMinuteEnd*60));

        obj.outageIndices = obj.outageIndices | (obj.Time == outageMinuteStart*60) | (obj.Time == outageMinuteEnd*60);

    end


    %function obj = SetOutageExt(obj, arrOutageStartEndCells)

    %    for i = 1:length(arrOutageStartEndCells)

    %                obj.isOutage = obj.isOutage + (obj.Time >= arrOutageStartEndCells(i,1)*60) & (obj.Time <= arrOutageStartEndCells(i,2)*60);

    %    end

    %end


    function tt = AsTimeTablePowerFromBattery(obj)

        tt = timetable(obj.timeDuration, obj.powerFromBattery);

    end


    function tt = AsTimeTablePower(obj)

        tt = timetable(obj.timeDuration, obj.power);

    end

  end

end
```

```
classdef clsPowerDescriptor

  properties

    Data

    Mean

    Max
```

```
    Std

    Total

    AvgDay

end


methods

    function obj = clsPowerDescriptor(datetime, power)

        % Constructor to initialize the properties

        obj.Data = timetable(datetime, power, 'VariableNames', {'power'});

        result = clsPowerDescriptor.GetPowerStatistics(obj.Data);


        obj.Mean = result.mean;

        obj.Max = result.max;

        obj.AvgDay = result.avgDay;

        obj.Std = result.std;

        obj.Total = result.yield;

    end

end


methods (Static)

    function result = RemoveOutages(powerDescriptor, thresholdHours, dropOutageTimes)

        arguments

            powerDescriptor clsPowerDescriptor

            thresholdHours double

            dropOutageTimes

        end


            timetableDates = dateshift(powerDescriptor.Data.datetime, 'start', 'day');

            outageDays = clsPowerDescriptor.GetOutageDays(powerDescriptor.Data, thresholdHours);

            isOutageDay = ismember(timetableDates, outageDays);

            withoutOutages = powerDescriptor.Data(~isOutageDay, :);

            if(dropOutageTimes)
```

```
            withoutOutages = clsPowerDescriptor.RemoveEmptyIndexes(withoutOutages);
        end
        result = clsPowerDescriptor(withoutOutages.datetime, withoutOutages.power);
end


function results = GetPowerStatistics(data)
    arguments
        data (:,1) timetable
    end

    % The data timetable must have the following 2 columns: datetime, power

    data = clsPowerDescriptor.CleanTimetable(data);

    results.raw = data;
    results.mean = retime(data, 'daily', 'mean');
    results.max = retime(data, 'daily', 'max');
    results.min = retime(data, 'daily', 'min');
    results.std = retime(data, 'daily', @std);
    results.yield = retime(data, 'daily', 'sum');

    % Temp tables for now
    meanPowerData = data;
    stdPowerData = data;

    for i = 1:height(data)
        % Get the date
        date = dateshift(data.datetime(i), 'start', 'day');

        % Find the mean and std for each data point
        meanPowerData.power(i) = results.mean.power(results.mean.datetime == date);
        stdPowerData.power(i) = results.std.power(results.std.datetime == date);
```

```
    end

    % Calculate the outliers
    isOutlier = abs(data.power - meanPowerData.power) > 3 * stdPowerData.power;
    results.withoutOutliers = data(~isOutlier, :);

    timeOfDay = timeofday(data.datetime);
    averageDayData = table(timeOfDay, data.power, 'VariableNames', {'time', 'power'});

    figure;
    scatter(averageDayData.time, averageDayData.power);

    averageDayData = varfun(@mean, averageDayData, 'GroupingVariables', 'time');

    results.avgDay = timetable(averageDayData.time, averageDayData.mean_power, 'VariableNames', {'power'});

end

function cleanedData = CleanTimetable(timetable)
    % Remove missing rows
    if any(any(ismissing(timetable)))
        % interpolate missing values with linear approximation
        timetable.power = fillmissing(timetable.power,'linear');
    end

    % Sort asc
    timetable = sortrows(timetable, 'datetime');

    cleanedData = timetable;
end

function outageDays = GetOutageDays(timetable, outageThreshold)
```

```
        % Detect which days have outages (zero consumption for a threshold period)
        isOutage = (timetable.power == 0);

        outageChange = diff([false; isOutage; false]);

        outageStarts = timetable.datetime(outageChange == 1);
        outageEnds = timetable.datetime(outageChange == -1);

        outageDurations = hours(outageEnds - outageStarts);
        isRealOutage = (outageDurations >= outageThreshold);

        outageDays = unique(dateshift(outageStarts(isRealOutage), 'start', 'day'));
    end

    function window = MaxPowerWindow(timetable, n)
        powerSum = movsum(timetable{:,1}, n, 'Endpoints', 'discard');

        % Index of the maximum power sum
        [~, maxIdx] = max(powerSum);

        window = struct;
        window.startTime = timetable.Time(maxIdx);
        window.endTime = timetable.Time(maxIdx + n - 1);
        window.maxPower = powerSum(maxIdx);
    end

    function result = RemoveEmptyIndexes(timetable)
        result = timetable(timetable.power ~= 0, :);
    end
  end
end
```

```
classdef clsPlotBuilder

  properties

    X

    Data

    Name

    Title

    XLabel

    YLabel

    TrendLines

    Legend

  end


  methods

    function obj = clsPlotBuilder(X, data, varargin)

      % Constructor to initialize the properties

      obj.X = X;

      obj.Data = data;

      obj.Name = 'Default Name';

      obj.Title = 'Default Title';

      obj.XLabel = 'X-axis Label';

      obj.YLabel = 'Y-axis Label';


      if nargin > 2

        obj.Name = varargin{1};

      end

    end


    function fig = Plot(obj)

      fig = figure('Name', obj.Name);


      numData = numel(obj.Data);

      colors = {'b-', 'r-', 'g-', 'k-'}; % Define colors for different data sets
```

```
        for i = 1:numData
            plot(obj.X, obj.Data{i}, colors{i});
            hold on;

            % If a trendline is specified for this data, add it to the plot
            if i <= numel(obj.TrendLines) && ~isempty(obj.TrendLines{i})
                trendline = polyval(obj.TrendLines{i}, datenum(obj.X));
                plot(obj.X, trendline, colors{i}, 'LineWidth', 2 );
                hold on;
            end
        end

        xlabel(obj.XLabel);
        ylabel(obj.YLabel);
        title(obj.Title);
        %xtickangle(45);
        grid on;

        exportgraphics(fig, obj.Name + ".jpeg", 'Resolution', 600);
        %legend(obj.Legend);
    end

    function obj = AddTrendLine(obj, index, order)
        % Check that index and order are valid
        assert(index > 0 && index <= numel(obj.Data), ...
            'Invalid data index.');
        assert(order >= 0 && rem(order, 1) == 0, ...
            'Order must be a non-negative integer.');

        obj.Data{index}(isnan(obj.Data{index})) = 0;
        p = polyfit(datenum(obj.X), obj.Data{index}, order);
```

```
            %Add to list of trendlines
            obj.TrendLines{index} = p;
        end
    end

    methods (Access = private)
        function [] = validate(obj)
            assert(length(obj.X) == length(obj.Data{1}), ...
                'X and Y data should have the same length.');

            for i = 2:numel(obj.Data)
                assert(length(obj.Data{i-1}) == length(obj.Data{i}), ...
                    'All data sets should have the same length.');
            end
        end
    end
end
```

APPENDIX B – VRFB TRAINING DATA EXTRACT

time(s)	Time (s) training set start	Current	Voltage	SOC
121593,8	33,77604	0,999804	1,396063	0,15
121608,8	33,78021	1,000182	1,405029	0,152074
121623,8	33,78438	1,000182	1,405518	0,154148
121638,8	33,78855	1,000147	1,405844	0,156222
121653,8	33,79272	1,000182	1,405844	0,158297
121668,8	33,79689	1,000182	1,406496	0,160371
121683,8	33,80105	1,000147	1,4078	0,162445
121698,8	33,80522	1,000182	1,409267	0,164519
121713,8	33,80939	1,000216	1,410408	0,166594
121728,8	33,81356	1,000182	1,411223	0,168668
121743,8	33,81773	1,000216	1,412201	0,170743
121758,8	33,8219	1,000182	1,413342	0,172816
121773,8	33,82607	1,000147	1,414157	0,17489
121788,8	33,83024	1,000182	1,415461	0,176965
121803,9	33,8344	1,000182	1,416439	0,179039
121818,9	33,83857	1,000182	1,41758	0,181113
121833,9	33,84274	1,000182	1,418395	0,183187
121848,9	33,84691	1,000182	1,419536	0,185262
121863,9	33,85108	1,000182	1,420515	0,187336
121878,9	33,85525	1,000182	1,421167	0,18941
121893,9	33,85942	1,000182	1,422308	0,191484
121908,9	33,86358	1,000216	1,423286	0,19356
121923,9	33,86775	1,000182	1,424264	0,195633
121938,9	33,87192	1,000182	1,424916	0,197707
121953,9	33,87609	1,000182	1,426057	0,199781
121968,9	33,88026	1,000182	1,427035	0,201855
121983,9	33,88443	1,000216	1,428013	0,203931
121998,9	33,8886	1,000182	1,428828	0,206004
122014	33,89277	1,000182	1,429806	0,208081
122029	33,89694	1,000182	1,430458	0,210154
122044	33,90111	1,000216	1,431273	0,212231
122059	33,90527	1,000182	1,432088	0,214303
122074	33,90944	1,000182	1,433066	0,216377
122089	33,91361	1,000182	1,434044	0,218451
122104	33,91778	1,000147	1,434696	0,220523
122119	33,92195	1,000182	1,435674	0,222599
122134	33,92612	1,000182	1,436489	0,224674
122149	33,93029	1,000182	1,437304	0,226748
122164	33,93446	1,000182	1,437956	0,228822
122179	33,93862	1,000182	1,438771	0,230896
122194,1	33,94279	1,000147	1,439424	0,232968
122209,1	33,94696	1,000182	1,440076	0,235045
122224,1	33,95113	1,000182	1,440728	0,237119
122239,1	33,9553	1,000182	1,44138	0,239193
122254,1	33,95947	1,000182	1,441869	0,241267
122269,1	33,96364	1,000182	1,442847	0,243342
122284,1	33,9678	1,000182	1,443499	0,245416
122299,1	33,97197	1,000182	1,444314	0,24749
122314,1	33,97614	1,000182	1,44464	0,249564
122329,1	33,98031	1,000182	1,445618	0,251638
122344,1	33,98448	1,000182	1,446107	0,253713
122359,1	33,98865	1,000182	1,447085	0,255787
122374,1	33,99282	1,000182	1,447737	0,257861
122389,1	33,99698	1,000182	1,448389	0,259935
122404,2	34,00115	1,000182	1,449041	0,262009
122419,2	34,00532	1,000182	1,449693	0,264084
122434,2	34,00949	1,000182	1,450345	0,266158
122449,2	34,01366	1,000182	1,45116	0,268232
122464,2	34,01783	1,000182	1,451812	0,270306

122479,2	34,022	1,000182	1,452301	0,27238
122494,2	34,02617	1,000182	1,453279	0,274455
122509,2	34,03033	1,000182	1,453768	0,276529
122524,2	34,0345	1,000182	1,45442	0,278603
122539,2	34,03867	1,000182	1,455072	0,280677
122554,2	34,04284	1,000147	1,455724	0,282747
122569,2	34,04701	1,000182	1,456539	0,284826
122584,3	34,05119	1,000182	1,457191	0,286904
122599,3	34,05535	1,000182	1,45768	0,288978
122614,3	34,05952	1,000182	1,45817	0,291053
122629,3	34,06369	1,000147	1,458985	0,293122
122644,3	34,06786	1,000216	1,4598	0,295206
122659,3	34,07203	1,000182	1,460289	0,297275
122674,3	34,0762	1,000216	1,460941	0,299355
122689,3	34,08037	1,000147	1,46143	0,301419
122704,3	34,08453	1,000147	1,462245	0,303493
122719,3	34,0887	1,000216	1,462734	0,305577
122734,3	34,09287	1,000182	1,463223	0,307646
122749,3	34,09704	1,000147	1,463875	0,309715
122764,4	34,10121	1,000182	1,464527	0,311795
122779,4	34,10538	1,000147	1,465179	0,313863
122794,4	34,10955	1,000216	1,465831	0,315949
122809,4	34,11372	1,000182	1,466483	0,318017
122824,4	34,11788	1,000147	1,466809	0,320086
122839,4	34,12205	1,000182	1,467624	0,322166
122854,4	34,12622	1,000147	1,468113	0,324234
122869,4	34,13039	1,00025	1,468928	0,326326
122884,4	34,13456	1,000147	1,469417	0,328382
122899,4	34,13873	1,000147	1,469906	0,330456
122914,4	34,1429	1,000147	1,470721	0,332531
122929,4	34,14706	1,000147	1,471373	0,334605
122944,4	34,15123	1,000147	1,472025	0,336679
122959,4	34,1554	1,000147	1,472514	0,338753
122974,5	34,15957	1,000182	1,473166	0,340834
122989,5	34,16374	1,000182	1,473818	0,342908
123004,5	34,16791	1,000147	1,474307	0,344975
123019,5	34,17208	1,000216	1,475122	0,347063
123034,5	34,17624	1,000147	1,475611	0,349124
123049,5	34,18041	1,000147	1,476264	0,351198
123064,5	34,18458	1,000147	1,476753	0,353272
123079,5	34,18875	1,000182	1,477405	0,355353
123094,5	34,19292	1,000147	1,477731	0,35742
123109,5	34,19709	1,000182	1,47822	0,359502
123124,5	34,20126	1,000147	1,478872	0,361568
123139,5	34,20543	1,000147	1,479361	0,363643
123154,5	34,20959	1,000147	1,47985	0,365717
123169,5	34,21376	1,000182	1,480502	0,367798
123184,6	34,21793	1,000182	1,480828	0,369873
123199,6	34,2221	1,000147	1,481317	0,371939
123214,6	34,22627	1,000147	1,481806	0,374013
123229,6	34,23044	1,000113	1,482295	0,37608
123244,6	34,23461	1,000147	1,482947	0,378162
123259,6	34,23877	1,000147	1,483436	0,380236
123274,6	34,24294	1,000147	1,483925	0,38231
123289,6	34,24711	1,000113	1,484251	0,384376
123304,6	34,25128	1,000147	1,485066	0,386458
123319,6	34,25545	1,000182	1,485555	0,38854
123334,6	34,25962	1,000113	1,486044	0,390598
123349,6	34,26379	1,000182	1,486533	0,392689
123364,6	34,26795	1,000182	1,487185	0,394763
123379,6	34,27212	1,000147	1,487511	0,396829
123394,7	34,27629	1,000182	1,488163	0,398911
123409,7	34,28046	1,000182	1,488815	0,400986
123424,7	34,28463	1,000147	1,489304	0,403051
123439,7	34,2888	1,000182	1,489793	0,405134
123454,7	34,29297	1,000147	1,490282	0,4072

APPENDIX C – CONSUMPTION DATA EXTRACT

Date/Time	Time	kWh	kVArh	kVA	PF
2022/01/01 00:00	00:30	28,661	14,388	64,1395	0,8937
2022/01/01 00:00	01:00	31,25	15,531	69,7933	0,8955
2022/01/01 00:00	01:30	28,664	14,727	64,4518	0,8895
2022/01/01 00:00	02:00	29,935	14,439	66,4707	0,9007
2022/01/01 00:00	02:30	29,425	13,673	64,8932	0,9069
2022/01/01 00:00	03:00	29,597	13,8	65,3122	0,9063
2022/01/01 00:00	03:30	29,426	14,288	65,4228	0,8996
2022/01/01 00:00	04:00	30,026	13,868	66,1478	0,9078
2022/01/01 00:00	04:30	29,276	14,322	65,1829	0,8983
2022/01/01 00:00	05:00	29,869	13,986	65,9626	0,9056
2022/01/01 00:00	05:30	27,892	13,409	61,8956	0,9013
2022/01/01 00:00	06:00	25,958	15,08	60,0408	0,8647
2022/01/01 00:00	06:30	20,943	14,107	50,5021	0,8294
2022/01/01 00:00	07:00	21,094	13,464	50,0494	0,8429
2022/01/01 00:00	07:30	15,498	13,269	40,8046	0,7596
2022/01/01 00:00	08:00	18,726	19,497	54,0665	0,6927
2022/01/01 00:00	08:30	11,61	19,264	44,9842	0,5162
2022/01/01 00:00	09:00	11,235	19,059	44,248	0,5078
2022/01/01 00:00	09:30	8,961	23,721	50,7143	0,3534
2022/01/01 00:00	10:00	9,61	27,612	58,4731	0,3287
2022/01/01 00:00	10:30	8,119	28,628	59,5141	0,2728
2022/01/01 00:00	11:00	8,729	30,474	63,3991	0,2754
2022/01/01 00:00	11:30	10,647	32,945	69,2454	0,3075
2022/01/01 00:00	12:00	9,879	33,984	70,7815	0,2791
2022/01/01 00:00	12:30	14,315	33,731	73,2857	0,3907
2022/01/01 00:00	13:00	10,321	34,498	72,0176	0,2866
2022/01/01 00:00	13:30	13,782	35,492	76,1479	0,362
2022/01/01 00:00	14:00	15,379	33,614	73,9301	0,416
2022/01/01 00:00	14:30	21,145	31,569	75,9924	0,5565
2022/01/01 00:00	15:00	19,018	33,745	77,4702	0,491
2022/01/01 00:00	15:30	29,829	31,886	87,3267	0,6832
2022/01/01 00:00	16:00	31,075	29,779	86,0801	0,722
2022/01/01 00:00	16:30	38,104	29,277	96,1053	0,793
2022/01/01 00:00	17:00	30,012	30,763	85,9554	0,6983
2022/01/01 00:00	17:30	34,308	30,464	91,7626	0,7478
2022/01/01 00:00	18:00	39,89	28,756	98,3488	0,8112
2022/01/01 00:00	18:30	43,457	29,605	105,1659	0,8264
2022/01/01 00:00	19:00	43,266	28,597	103,7253	0,8342
2022/01/01 00:00	19:30	43,429	26,675	101,934	0,8521
2022/01/01 00:00	20:00	37,487	21,748	86,6776	0,865
2022/01/01 00:00	20:30	36,793	20,38	84,1206	0,8748
2022/01/01 00:00	21:00	35,318	20,605	81,7784	0,8637
2022/01/01 00:00	21:30	30,865	15,96	69,4945	0,8883
2022/01/01 00:00	22:00	32,516	16,968	73,354	0,8865
2022/01/01 00:00	22:30	32,058	16,143	71,7861	0,8932
2022/01/01 00:00	23:00	29,836	15,012	66,7996	0,8933
2022/01/01 00:00	23:30	33,243	17,513	75,1479	0,8847
2022/01/02 00:00	00:00	28,669	14,093	63,8913	0,8974
2022/01/02 00:00	00:30	29,657	14,352	65,8944	0,9001
2022/01/02 00:00	01:00	28,253	13,528	62,6495	0,9019
2022/01/02 00:00	01:30	29,283	14,043	64,9523	0,9017
2022/01/02 00:00	02:00	28,628	13,582	63,373	0,9035
2022/01/02 00:00	02:30	29,703	13,968	65,6467	0,9049
2022/01/02 00:00	03:00	29,142	13,502	64,2358	0,9073
2022/01/02 00:00	03:30	29,657	14,379	65,9179	0,8998
2022/01/02 00:00	04:00	29,43	13,714	64,9369	0,9064
2022/01/02 00:00	04:30	28,185	12,883	61,9795	0,9095
2022/01/02 00:00	05:00	29,521	14,08	65,4136	0,9026
2022/01/02 00:00	05:30	28,302	12,92	62,2231	0,9097
2022/01/02 00:00	06:00	25,987	14,573	59,5885	0,8722
2022/01/02 00:00	06:30	22,514	14,51	53,5694	0,8406
2022/01/02 00:00	07:00	21,248	15,004	52,023	0,8169
2022/01/02 00:00	07:30	20,874	18,982	56,4284	0,7398
2022/01/02 00:00	08:00	18,918	18,803	53,3458	0,7093
2022/01/02 00:00	08:30	17,31	21,951	55,91	0,6192
2022/01/02 00:00	09:00	17,792	25,393	62,0116	0,5738

APPENDIX D – SOLAR DATA EXTRACT

Time period	Power [kW]
07/23/2022 07.00 AM	0
07/23/2022 07.15 AM	0.33
07/23/2022 07.30 AM	0.93
07/23/2022 07.45 AM	1.82
07/23/2022 08.00 AM	2.58
07/23/2022 08.15 AM	3.83
07/23/2022 08.30 AM	4.6
07/23/2022 08.45 AM	5.25
07/23/2022 09.00 AM	5.78
07/23/2022 09.15 AM	9.15
07/23/2022 09.30 AM	28.87
07/23/2022 09.45 AM	28.59
07/23/2022 10.00 AM	21.06
07/23/2022 10.15 AM	21.77
07/23/2022 10.30 AM	26.64
07/23/2022 10.45 AM	16.69
07/23/2022 11.00 AM	31.47
07/23/2022 11.15 AM	45.14
07/23/2022 11.30 AM	30.24
07/23/2022 11.45 AM	28.64
07/23/2022 12.00 PM	29.55
07/23/2022 12.15 PM	48.01
07/23/2022 12.30 PM	31.63
07/23/2022 12.45 PM	33.62
07/23/2022 01.00 PM	33.16
07/23/2022 01.15 PM	33.14
07/23/2022 01.30 PM	20.52
07/23/2022 01.45 PM	10.03
07/23/2022 02.00 PM	16.17
07/23/2022 02.15 PM	7.76
07/23/2022 02.30 PM	10.19
07/23/2022 02.45 PM	31.9
07/23/2022 03.00 PM	11.81
07/23/2022 03.15 PM	4.94
07/23/2022 03.30 PM	8.86
07/23/2022 03.45 PM	5.56
07/23/2022 04.00 PM	2.15
07/23/2022 04.15 PM	2.23
07/23/2022 04.30 PM	2.07
07/23/2022 04.45 PM	4.42
07/23/2022 05.00 PM	4.19
07/23/2022 05.15 PM	2.55
07/23/2022 05.30 PM	0.61
07/23/2022 05.45 PM	0.04
07/23/2022 06.00 PM	0
07/23/2022 06.15 PM	'-
07/24/2022 07.00 AM	0.04
07/24/2022 07.15 AM	0.44
07/24/2022 07.30 AM	1.32
07/24/2022 07.45 AM	3.37
07/24/2022 08.00 AM	7.41
07/24/2022 08.15 AM	8.65
07/24/2022 08.30 AM	13.02

APPENDIX E – MATLAB RESULS N1 DATA

Time	Consumed power (kW) average day	Consumed power (kW) average day [but removed days from global set with loadshedding]
00:00:00	74,44343	80,07271
00:30:00	74,38745	80,24497
01:00:00	75,98299	80,77079
01:30:00	75,42139	80,58556
02:00:00	75,37854	80,39021
02:30:00	74,15857	80,31766
03:00:00	74,93786	80,12765
03:30:00	74,87959	80,03128
04:00:00	74,70033	79,93148
04:30:00	73,72669	79,84913
05:00:00	74,08028	79,57074
05:30:00	72,5884	79,01215
06:00:00	71,2493	78,05426
06:30:00	71,10723	78,23579
07:00:00	71,40941	77,98078
07:30:00	69,58909	75,92916
08:00:00	75,88172	81,62889
08:30:00	81,40841	88,69073
09:00:00	83,60093	88,3353
09:30:00	82,03776	85,28871
10:00:00	80,34186	83,06879
10:30:00	75,2175	80,05702
11:00:00	74,52138	78,40392
11:30:00	73,93152	77,4563
12:00:00	74,30518	76,88812
12:30:00	71,1937	76,85941
13:00:00	73,59343	78,00288
13:30:00	76,22419	80,68387
14:00:00	77,54879	81,58727
14:30:00	79,52796	86,6138
15:00:00	86,3636	90,89833
15:30:00	87,02541	90,90141
16:00:00	86,37039	90,92768
16:30:00	78,33714	88,38479
17:00:00	78,4745	86,86144
17:30:00	78,20468	85,11558
18:00:00	79,3255	86,39397
18:30:00	79,23254	88,45125
19:00:00	82,28047	88,73749
19:30:00	80,37717	87,06938
20:00:00	79,53862	86,35391
20:30:00	72,88067	84,24996
21:00:00	74,12253	83,79258
21:30:00	73,63971	83,20629
22:00:00	73,54237	82,97885
22:30:00	72,56559	83,53942
23:00:00	75,20445	83,48969
23:30:00	74,76963	82,81907